ASPECTS OF SOUTHERN OCEAN TRANSPORT AND MIXING

A thesis submitted to the
School of Environmental Sciences
of the
University of East Anglia
in partial fulfilment of the requirements for the degree of
Doctor of Philosophy

By
Gillian M. Damerell
September 2012

Abstract

Understanding and quantifying the circulation of the oceans and the driving mechanisms thereof is an important step in developing models which can accurately predict future climate change. In particular, model studies have shown that the spatial variability of diapycnal diffusivity, which represents the rate at which deep water returns to shallower depths by means of turbulent diapycnal mixing, is a critical factor controlling the strength and structure of the circulation. Efforts are therefore ongoing to measure diffusivity as extensively as possible, but temporal variability in diffusivity has not been widely addressed.

Results from three Southern Ocean studies are presented in this thesis. Firstly, a high resolution hydrographic survey carried out on the northern flank of the Kerguelen Plateau identifies a complex meandering current system carrying a total eastward volume transport of 174 $\pm$ 22 Sv, mostly associated with the blended Subtropical Front/Subantarctic Front. Significant water mass transformation across isopycnals is not required to balance the budgets in this region. Secondly, results are presented which cast doubt on the advisability of using density profiles acquired using Conductivity-Temperature-Depth instruments to estimate diapycnal diffusivity (an attractive proposition due to low cost and widespread data availability) in areas of weak stratification such as the Southern Ocean, because the noise characteristics of the data result in inaccurate diffusivity estimates. Finally, a method is developed for estimating diffusivity from profiles of velocity shear acquired by moored acoustic Doppler current profilers. An 18-month time series of diffusivity estimates is derived with a median of 3.3×10^{-4} m^2 s^{-1} and a range of 0.5×10^{-4} m^2 s^{-1} to 57×10^{-4} m^2 s^{-1}. There is no significant signal at annual or semiannual periods, but there is evidence of signals at periods of approximately fourteen days (likely due to the spring-neaps tidal cycle), and at periods of 3.8 and 2.6 days most likely due to topographically-trapped waves propagating around the local seamount. More widespread application of this method would allow for an assessment of natural climate variability in diapycnal diffusivity.

Acknowledgements

It gives me great pleasure to acknowledge some of the people who have helped in the completion of this thesis. In particular, my supervisors - Dave Stevens for many useful discussions and advice, Alberto Naveira Garabato for explaining diffusivity calculations, Brian King for teaching me the workings of the ADCP and making me a much more knowledgeable sea-going scientist, and above all, Karen Heywood, for her help, support, constructive criticism and endless patience, throughout my time at the UEA.

Thanks are also due to the U.K.'s Natural Environment Research Council (NERC), whose PhD studentship at the UEA supported me during the analysis and writing of this thesis.

The SOFine project is funded by NERC (grant numbers NE/G001510/1 and NE/ B503717). I am grateful to all the scientists, technicians, officers and crew involved in cruise JC029. The altimeter products were produced by Ssalto/Duacs and distributed by Aviso, with support from Cnes (http://www.aviso.oceanobs.com/duacs/).

The Shag Rocks Passage CTD, LADCP and mooring data were acquired as part of the North Scotia Ridge Overflow project, funded by the NERC grant NER/G/S/2001/00006 through the Antarctic Funding Initiative. The ERA-Interim data were obtained from ECMWF at http://www.ecmwf.int/research/era/do/get/index. The Brink model is made available at http://www.whoi.edu/page.do?pid=23361. Alex Tate kindly provided multibeam bathymetry from the British Antarctic Survey Marine Geophysical Database. I am grateful to Gareth Janacek and Adrian Matthews for useful discussions on spectral analysis, and the anonymous reviewers for their insightful comments.

The DIMES project is supported by the NERC grant NE/E005985/1, and the US National Science Foundation (grants ANT-0444134, ANT-0948338, OCE-0622740 and OCE-0957342). Thanks are also due to the officers, crew and scientific party aboard R/V Thomas G. Thompson for facilitating deployment of XCTDs as well as other instruments needed for this study during the very long and stormy DIMES US2 cruise.

I would like to thank my friends, obliging landlords, and work colleagues for their help and support during my time at the UEA. Finally, special thanks must go to my parents for their encouragement and love throughout.

LIST OF ACRONYMS

AABW	Antarctic Bottom Water
AAIW	Antarctic Intermediate Water
AASW	Antarctic Surface Water
ACC	Antarctic Circumpolar Current
ACCbw	Antarctic Circumpolar Current bottom water
ADCP	Acoustic Doppler Current Profiler
ARF	Agulhas Return Front
ASF	Antarctic Slope Front
CDW	Circumpolar Deep Water
CTD	Conductivity-Temperature-Depth
DIMES	Diapycnal and Isopycnal Mixing Experiment in the Southern Ocean
DMP	Deep Microstructure Profiler
ECMWF	European Centre for Medium-range Weather Forecasting
FT	Fawn Trough
GCM	General Circulation Model
GM	Garret and Munk (model spectrum)
HRP2	High Resolution Profiler
ISV	Integrated Shear Variance
LADCP	Lowered Acoustic Doppler Current Profiler
LCDW	Lower Circumpolar Deep Water
NADW	North Atlantic Deep Water
NERC	Natural Environment Research Council
NIDW	North Indian Deep Water
NKP	Northern Kerguelen Plateau
OTM	Ocean Temperature Module
PET	Princess Elizabeth Trough
PF	Polar Front
RAFOS	SOund Fixing And Ranging (backwards)
RCM	Rotary Current Meter
RMS	Root mean square
SB	Southern Boundary of the ACC
SACCF	Southern ACC Front
SAF	SubAntarctic Front
SASW	SubAntarctic Surface Water

SKP	Southern Kerguelen Plateau
SOFine	Southern Ocean Finestructure
SRP	Shag Rocks Passage
SSH	Sea Surface Height
SSS	Sea Surface Salinity
SST	Sea Surface Temperature
STF	SubTropical Front
STSW	SubTropical Surface Water
UCDW	Upper Circumpolar Deep Water
UEA	University of East Anglia
VMADCP	Vessel-Mounted Acoustic Doppler Current Profiler
WOCE	World Ocean Circulation Experiment
XCTD	eXpendable Conductivity-Temperature-Depth

Contents

List of Tables

List of Figures

Chapter 1

Introduction

1.1 General Context

The circulation of the world's oceans is an important controlling factor for the surface climate due to the high heat capacity of water, the contribution of the oceans to the meridional transport of heat, and the ocean-atmosphere exchanges of gases, water, heat, momentum and particulate matter (Bigg et al., 2003). Abrupt and dramatic changes in the climate of the past have been linked to non-linear behaviour of the ocean circulation (McManus et al., 2004; Rahmstorf, 2002), and there is some concern that anthropogenic CO_2 emissions might lead to an abrupt shift in circulation patterns in the future (Broecker, 1997). Thus understanding, and quantifying, the circulation of the oceans and the driving mechanisms thereof is an important step in developing models which can accurately predict the future response to anthropogenic activity. The main ocean transports and the rate of formation of deep water at high latitudes are reasonably well measured (Figure 1.1), but the return of deep water to shallower depths remains an area of extensive research (Ganachaud and Wunsch, 2000).

1.2 The Southern Ocean

In the late 1700s, Captain Cook first used the term 'Southern Ocean' to describe the area surrounding Antarctica, particularly referring to the fairly uniform nature of the climate, currents, winds and marine life. The Southern Ocean is not physically separated from the oceans to the north, so could be considered as southward extensions of the Atlantic, Indian and Pacific Oceans. However, the northern current systems of the Southern Ocean sharply delineate the cold waters and

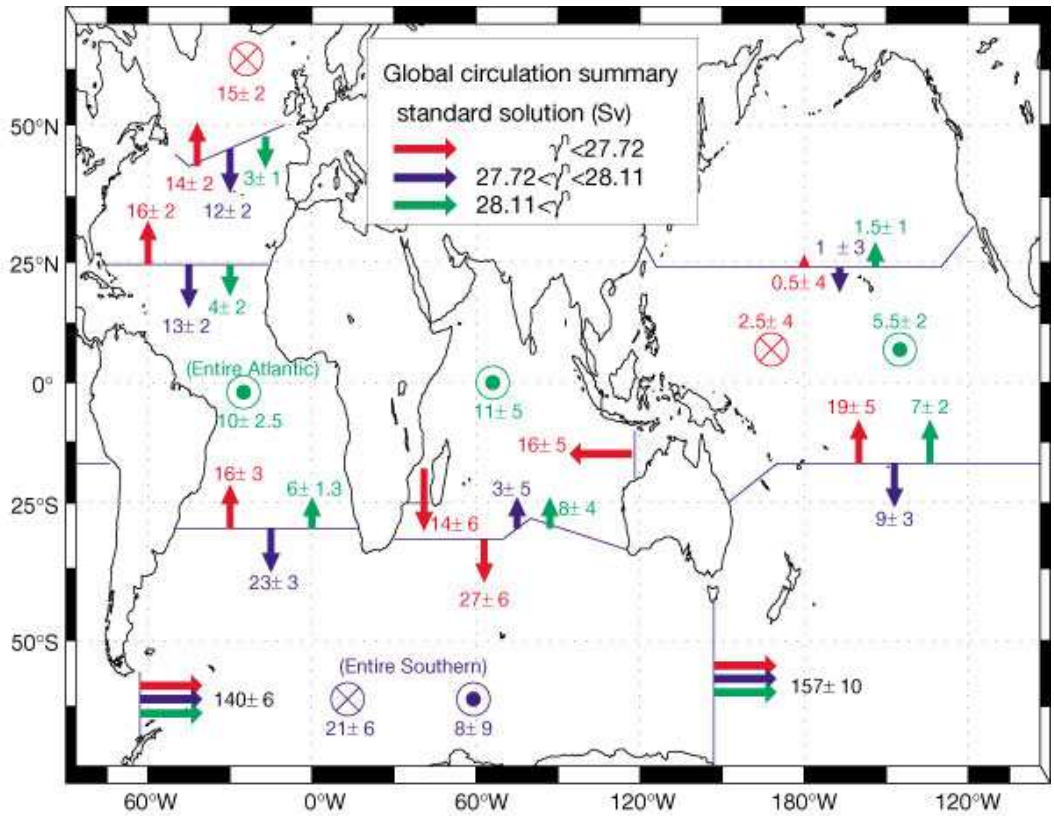

Figure 1.1: Zonally integrated layer volume transports in Sv (Sverdrups, 10^6 m^3 s^{-1}). The estimated water transports are indicated for the different density classes bounded by neutral surfaces (γ^n, in kg m^{-3}) and across selected hydrographic sections. Neutral surfaces are close to surfaces of constant density, but are chosen so that movement along them minimizes the work done against gravity. The colour of the upwelling or down-welling arrows indicates the layer from which the water is coming. In the Southern Ocean, the bottom water formation takes place mostly in the Weddell Sea, while the upwelling distribution is uncertain. In the Indian Ocean, most of the upwelling takes place north of 7°S. The South Pacific transports are given at 17°S because of the more complicated structure at 32°S. Reproduced from Ganachaud and Wunsch (2000).

distinct biota of the Antarctic from the warmer waters of the subtropical South Atlantic, South Pacific and Indian Oceans.

1.2.1 The Antarctic Circumpolar Current

There are a number of current systems in the Southern Ocean, but by far the largest is the Antarctic Circumpolar Current (ACC) - the only current to flow around the globe without encountering any continuous land barrier (Figure 1.2). Thus, the Southern Ocean joins the three main ocean basins of the Atlantic, Pacific and Indian Oceans, and the zonal transport of the ACC facilitates the exchange of water and

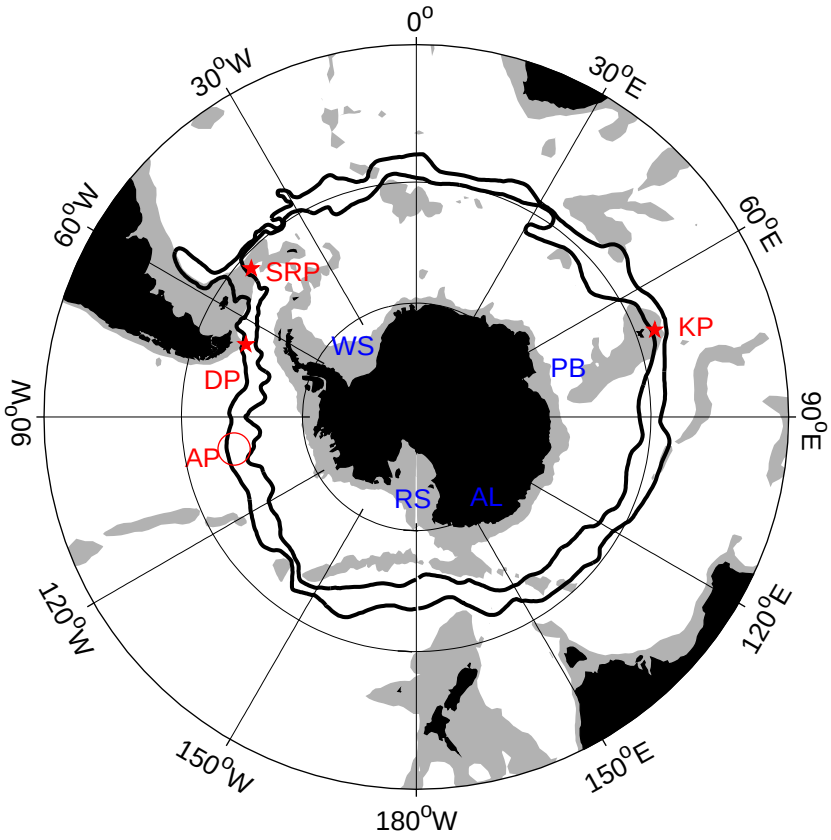

Figure 1.2: Schematic of the region south of 30°S, including the Southern Ocean. Depths shallower than 3000 m are shaded grey. Thick black contours indicate climatological mean locations of the Polar Front (south) and Subantarctic Front (north) from Orsi et al. (1995). Red markers and labels indicate the locations discussed in later chapters: the Kerguelen Plateau (KP) in chapter 2, Shag Rocks Passage (SRP) in chapter 3, and Drake Passage (DP) and the abyssal plain (AP) in the southeastern Pacific region of the Southern Ocean, in chapter 5. Blue labels indicate locations mentioned in this chapter: WS=Weddell Sea, RS=Ross Sea, AL=Adélie Land, PB=Prydz Bay.

water properties (heat, salt, nutrients, etc.) between those oceans. The extent of the ACC is usually defined in terms of the circumpolar waters that pass through Drake Passage (Orsi et al., 1995), with an associated baroclinic transport (relative to the deepest common layer) through Drake Passage of 136.7 $\pm$ 7.8 Sv (Cunningham et al., 2003). Baroclinic and barotropic variability are both important contributors to the variability of the net transport through Drake Passage, though the latter contributes most (Cunningham et al., 2003). The transport of the ACC at different longitudes, and the temporal variability of that transport, is an ongoing area of research (e.g. Ganachaud and Wunsch, 2000; Gladyshev et al., 2008; Heywood and King, 2002; Meijers et al., 2010; Rintoul and Sokolov, 2001). Observations of ACC

transport on the northern flank of the Kerguelen Plateau are the subject of chapter 2.

The ACC consists of a number of circumpolar fronts, which can correspond to water mass boundaries as well as deep-reaching jets of eastward flow (Orsi et al., 1995). Between the jets, the flow is dominated by eddies and can be in any direction (Talley et al., 2011). The two main fronts are the Polar and Subantarctic Fronts, whose climatological mean positions are shown in Figure 1.2. To the south of the ACC, cyclonic gyres are found in the embayments of the Weddell and Ross Seas, and the westward flowing Antarctic Slope Current (Jacobs, 1991) is found near the continental margin around most of Antarctica. North of the Subantarctic Front is the eastward flowing jet associated with the Subtropical Front, and further north the circulation consists of westward-intensified subtropical gyres in each ocean basin. The large topographic features in the path of the ACC, such as the Scotia Island arc east of Drake Passage and the Kerguelen Plateau in the Indian Ocean, act to steer the currents, as noted early on by Sverdrup et al. (1942), and described by Gordon et al. (1978). Form drag due to bottom topography (Munk and Palmn, 1951; Gille, 1997; Stevens and Ivchenko, 1997) is an important contributor to energy dissipation in the ACC.

1.2.2 Wind Forcing and Water Mass Formation

The wind forcing for the Southern Ocean is dominated by westerlies in the latitude band 40-60°S and easterlies close to Antarctica, south of 60°S. The surface wind stress is the primary driver of the ACC, though the coupling and relative importance of wind and thermohaline driving have not been fully investigated. South of the westerly wind stress maximum, the Ekman transport is divergent and deep water upwells into the surface layer; north of the westerly wind maximum, the Ekman transport is convergent and surface waters are downwelled into the ocean interior (Figure 1.3). This is thought to be responsible for the subduction and northward export of Antarctic Intermediate Water (Hanawa and Talley, 2001; Talley et al., 2011).

Close to the Antarctic continent, the strong easterly winds drive Ekman transport towards the continent, inducing downwelling at the boundary (Talley et al., 2011). Antarctic Bottom Water (AABW) is formed in the Weddell Sea, Ross Sea, along the coast of Adélie Land, and possibly also in Prydz Bay (Tamura et al., 2008). As very cold and dense shelf water spills down the continental slope, it mixes with Circumpolar Deep Water to form AABW. The meridional overturning circulation

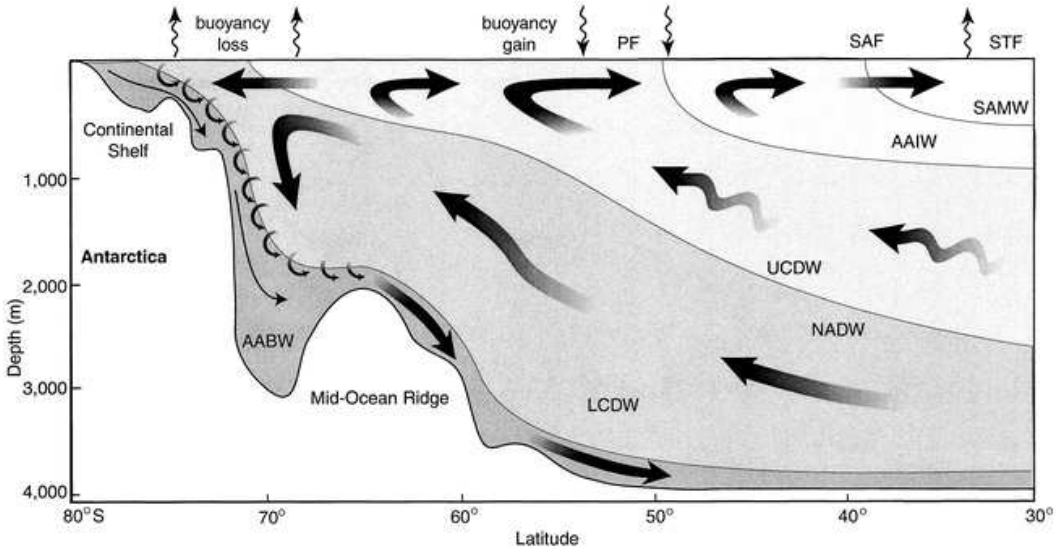

Figure 1.3: A schematic view of the meridional overturning circulation in the Southern Ocean. An upper cell is formed primarily by northward Ekman transport driven by the strong westerly winds and southward eddy transport in the UCDW layer, leading to the formation of AAIW. A lower cell is driven primarily by formation of AABW near the Antarctic continent. SAMW=Subantarctic Mode Water, AAIW=Antarctic Intermediate Water, UCDW=Upper Circumpolar Deep Water, NADW=North Atlantic Deep Water, LCDW=Lower Circumpolar Deep Water, AABW=Antarctic Bottom Water, PF=Polar Front, SAF=Subantarctic Front, STF=Subtropical Front. (See chapter 2 for front and water mass definitions.) Reproduced from Speer et al. (2000).

in the Southern Ocean thus consists of two cells, an upper cell formed primarily by northward Ekman transport driven by the strong westerly winds in the latitude band 40-60°S, and a lower cell driven primarily by formation of AABW near the Antarctic continent.

1.3 Diapycnal Mixing

In order for deep water to mix upwards into shallower waters, its density must be reduced. This is referred to as diapycnal mixing as it involves mixing across surfaces of constant density (isopycnals). If this did not occur, the ocean basins would gradually fill up with cold, dense bottom waters such as AABW. The necessary reduction in density is achieved by the downward diffusion of heat (Munk and Wunsch, 1998). Molecular diffusion does not result in sufficient diffusion of heat to balance the rate of deep water formation: turbulent diffusion is required. Measuring diapycnal mixing involves calculating the vertical diffusivity κ_z, which appears in the equation for conservation of any conservative water mass

property μ (e.g., conservative temperature, salinity, dissolved CO_2, etc):

$$\frac{\partial \mu}{\partial t} + \mathbf{v}.\nabla\mu = \kappa_H \left(\frac{\partial^2 \mu}{\partial x^2} + \frac{\partial^2 \mu}{\partial y^2} \right) + \frac{\partial}{\partial z} \left(\kappa_z \frac{\partial \mu}{\partial z} \right) + Q_\mu \,, \tag{1}$$

where t is time, **v** is velocity, κ_H the horizontal diffusivity (which in this thesis we assume is constant), x and y the horizontal spatial coordinates, and z the vertical coordinate. Q_μ is a source/sink function. When considering the steady-state case for conservative temperature Θ, it has long been considered a reasonable assumption that vertical advection is balanced primarily by vertical diffusion, which leads to the expression:

$$w \frac{\partial \Theta}{\partial z} = \frac{\partial}{\partial z} \left(\kappa_z \frac{\partial \Theta}{\partial z} \right) \,, \tag{2}$$

where w is the vertical component of velocity (Pond and Pickard, 1983).

A simple model estimate of the global average diapycnal diffusivity needed to complete the oceans' circulation is 10^{-4} m^2 s^{-1} (Munk and Wunsch, 1998). Ganachaud and Wunsch (2000) made more detailed estimates based on the observed flows between large oceanic regions (Figure 1.1 and table 1.1), and found diffusivities in the Atlantic, Indian and Pacific oceans need to be around 9-12 $\times 10^{-4}$ m^2 s^{-1} for bottom waters (below ~ 3800 m) and 3-4 $\times 10^{-4}$ m^2 s^{-1} for deep waters (~ 2000 to 3500 m) to maintain a steady-state ocean. They were unable to estimate diffusivity in the Southern Ocean.

Table 1.1: Average κ_z calculated by considering the currents into and out of different ocean basins at different depths. The 'bottom' layers are approximately 3800 m depth to the sea floor, and the deep layers are approximately 2000 - 3500 m depth. κ_z could not be resolved in the Southern Ocean. Adapted from Ganachaud and Wunsch (2000).

Ocean basin and water layer	κ_z ($\times 10^{-4}$ m^2 s^{-1})
Atlantic bottom	9 ± 4
Indian bottom	12 ± 7
Pacific bottom	9 ± 2
Southern bottom	-
Atlantic deep	3 ± 1.5
Indian deep	4 ± 2
Pacific deep	4 ± 1
Southern deep	-

1.3.1 Measuring Diapycnal Diffusivity

The most direct method to quantify diffusivity is tracer release: a chemically inert substance which can be detected at low concentrations is released at a known location and depth. The spread of the tracer, especially the diapycnal spread, is monitored over the next few months or years, which allows the diapycnal mixing to be measured (Ledwell et al., 1998). Unfortunately, although conceptually simple, large-scale experiments of this type require a great deal of funding and ship time, so are not widely used (Merryfield, 2005). Tracer release also suffers from the drawback of providing a measure of diffusivity integrated over a wide area and time span: while this may improve the accuracy of measurement, very little information can be gained about the spatial and temporal variability of the diffusivity.

The alternative is to use profiles of temperature, salinity and current velocities/shears as indicators of the diffusivity. This was originally (and is still) done using microstructure profilers (e.g. Toole et al., 1994; Polzin et al., 1996, 1997; Lueck and Mudge, 1997) measuring the variance in these quantities on centimetre-scales, but again, such instruments are very costly to build and operate, and are further limited by the difficulty of deploying the instruments in rough weather conditions. Efforts have therefore gone into developing methods for calculating diffusivity from data which can be obtained with greater ease and at less expense. There are three main methods, which will be discussed further in later chapters, two based on density profiles alone (chapter 5), and one which also requires current velocity/shear data (chapter 3), though only on scales of a few metres rather than a few centimetres.

CTD (conductivity-temperature-depth) data are routinely collected on oceanographic cruises, either by lowered instruments or expendable CTD probes (XCTDs), and more recently by autonomous platforms such as Argo floats and Seagliders. These can all be used to find profiles of density. κ_z can then be calculated using a 'Thorpe scale' analysis based on the vertical size of density overturns (e.g., Thompson et al., 2007; Sloyan et al., 2010), or from the strain, the vertical gradient in the vertical displacement of isopycnals induced by internal waves (e.g., Mauritzen et al., 2002; Sloyan, 2005). Similarly, LADCP (lowered acoustic Doppler current profiler) data are regularly collected on oceanographic cruises. κ_z can be calculated from the vertical variance of the LADCP vertical shear induced by internal waves (e.g., Naveira Garabato et al., 2004; Kunze et al., 2006).

Such methods suffer from a variety of drawbacks. κ_z can at best only be inferred to within a factor of 3 - 4 (Polzin et al., 2002), although this disadvantage

is more than offset by the significant increase in spatial coverage (e.g., Kunze et al., 2006). As discussed in section 1.3.2, spatial variability in κ_z greatly exceeds this uncertainty. Thorpe scale analyses are dependent on overturns sufficiently large to be resolved by the instruments used (chapter 5). The strain and shear methods both suffer from a potentially critical problem. What is really calculated is a measure of the energy content of the internal wave field: one must then assume that this energy is dissipated locally, relying on the premise that the nonlinear interactions of internal waves initiate an energy cascade to smaller scales, resulting in turbulent dissipation (McComas and Muller, 1981; Henyey et al., 1986). As discussed in Waterman et al. (2012a,b), this may not always be the case.

1.3.2 Example Observational Studies

The observational data reveal a much more complex, spatially-varying distribution than that suggested by the work of Munk and Wunsch (1998) and Ganachaud and Wunsch (2000). In much of the ocean interior measurements of the diffusivity have found values of around 0.1 $\times 10^{-4}$ m^2 s^{-1} (Toole et al., 1994; Ledwell et al., 1998), an order of magnitude smaller than the estimate of the global average diapycnal diffusivity (10^{-4} m^2 s^{-1}) needed to complete the oceans' circulation (Munk and Wunsch, 1998). This prompted a number of further studies, which are summarised in table 1.2.

These observations reveal that κ_z is very dependent on location. In particular, mixing is greatly enhanced in regions with strong currents and complex topography, and this can affect virtually the entire water column (see, for example, Figure 1.4), not just the first few 10s of metres above the bottom where one might expect the water to be 'stirred-up'. This suggests that there must be a mechanism for the vertical propagation of turbulence, and internal waves (section 1.3.3) are the obvious candidate.

Efforts to quantify the spatial variability of κ_z are ongoing, but temporal variability has not been widely addressed. Most existing measurements or estimates of diffusivity are either snapshots at a single time, or a single integrated value over months or years. The few time series available, such as those discussed by Inall et al. (2000); Rippeth et al. (2002); Palmer et al. (2008); Moum and Nash (2009); Shroyer et al. (2010) are from shallow shelf seas or tidal channels, and cover only a few days or weeks, with the longest (Moum and Nash, 2009) spanning a period of four months. In chapter 3, I present a method which could, if applied widely, begin to address the question of whether single estimates in the deep ocean can be

Table 1.2: Example observational studies measuring κ_z. ACC = Antarctic Circumpolar Current, AABW = Antarctic Bottom Water, N.H. = northern hemisphere, A.O., I.O., P.O., S.O. = Atlantic, Indian, Pacific and Southern Oceans, respectively, D.P. = Drake Passage, MAR = Mid-Atlantic Ridge, N, E, S, and W are the cardinal compass directions, and NE = north-east, etc.

Location	Data Type	Results	Ref.
NE P.O. and NE A.O.	Microstructure profiler.	κ_z increased from 0.1 $\times 10^{-4}$ m^2 s^{-1} in the ocean interior to more than 1 $\times 10^{-4}$ m^2 s^{-1} near steeply sloping boundaries.	Toole et al. (1994)
Romanche fracture zone, a gap in MAR.	Microstructure profiler.	Average κ_z was 150 $\times 10^{-4}$ m^2 s^{-1} in the water below 4000 m downstream from the main sill. This contrasts with the background mid-depth κ_z in that region, which is estimated as 0.2 $\times 10^{-4}$ m^2 s^{-1}.	Polzin et al. (1996)
The Brazil Basin in the S A.O.	Microstructure profiler.	κ_z fairly uniform over the smooth abyssal plains at $\sim$0.1 $\times 10^{-4}$ m^2 s^{-1}, but mixing was enhanced throughout the water column above the rough MAR, with κ_z exceeding 5 $\times 10^{-4}$ m^2 s^{-1} in the bottommost 150 m (figure 1.4).	Polzin et al. (1997)
Cobb Seamount in the NE P.O.	Microstructure profiler.	Mixing was 100 to 10,000 times greater near the seamount than the background rate in the ocean interior.	Lueck and Mudge (1997)
Brazil Basin, S A.O.	Tracer and microstructure profiler.	Estimates of κ_z over the MAR found by Polzin et al. (1997) were revised upwards by a factor of 2 - 3.	Ledwell et al. (2000)
Waters above MAR (N.H. only).	CTD.	Found κ_z of 1 - 10 $\times 10^{-4}$ m^2 s^{-1}, decreasing with height above the ridge.	Mauritzen et al. (2002)
SE P.O. and SW A.O., either side of D.P.	CTD/LADCP.	Above the nearly featureless abyssal plains of the SE P.O., κ_z $\sim$0.1 $\times 10^{-4}$ m^2 s^{-1}, but over the rough topography of D.P., the S Scotia Ridge and E Scotia Sea, κ_z $\sim$1 $\times 10^{-4}$ m^2 s^{-1} at 500 m depth, increasing to $\sim$100 $\times 10^{-4}$ m^2 s^{-1} near the sea floor, with a maximum of $\sim$1000 $\times 10^{-4}$ m^2 s^{-1} in some deep cuts in the ridges. This is consistent with the basin-wide estimate for the Scotia Sea of 39 $\pm$ 10 $\times 10^{-4}$ m^2 s^{-1} found by Heywood et al. (2002), by considering the heat budget.	Naveira Garabato et al. (2004)
S A.O., I.O., S P.O. and S.O.	CTD.	In the S A.O., I.O. and S P.O., enhanced κ_z was found over rough topography, but returned to background levels 500 - 1000 m above the sea floor. In the S.O., enhanced κ_z was found throughout the water column (below 1500 m) in the ACC over complex topography, especially in the ACC frontal jets.	Sloyan (2005)
I.O., P.O., N A.O. and S.O.	$\sim$3500 full-depth CTD/LADCP profiles.	κ_z $\sim$0.1 $\times 10^{-4}$ m^2 s^{-1} in areas near the equator, over smooth topography, and in the upper ocean, but average κ_z increased with latitude to $\sim$0.4 - 0.5 $\times 10^{-4}$ m^2 s^{-1} at latitudes of 50-70°, and was also often $\sim$1 $\times 10^{-4}$ m^2 s^{-1} in the bottom 1000 m.	Kunze et al. (2006)
ACC in S.O.	^{3}He from hydrothermal vents: a natural tracer.	Average κ_z of 3.2 $\pm$ 2.3 $\times 10^{-4}$ m^2 s^{-1} over a sector which spans nearly a tenth of the ACC.	Naveira Garabato et al. (2007)

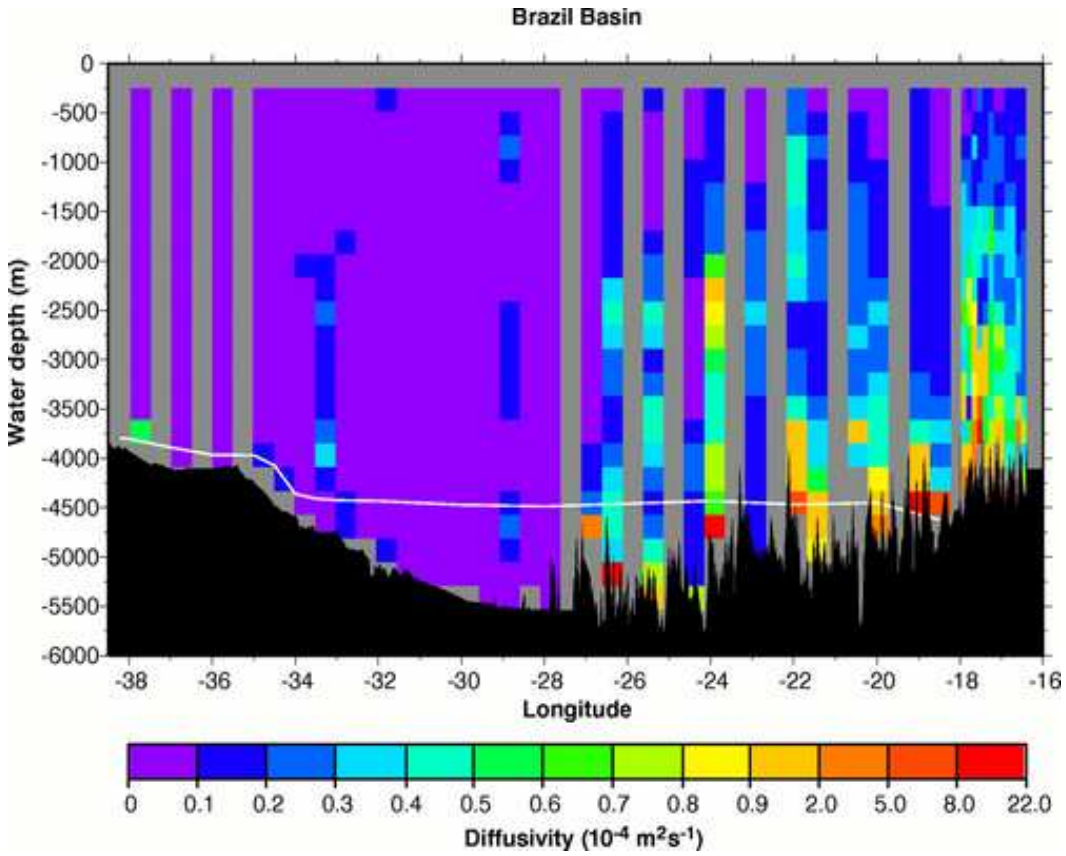

Figure 1.4: Depth-longitude section of κ_z in the Brazil Basin inferred from velocity microstructure observations. Note the nonuniform contour scale. The white line marks the observed depth of the 0.8°C surface. κ_z is greatly increased over the rough topography of the Mid-Atlantic Ridge on the right-hand side of the figure. Reproduced from Polzin et al. (1997).

considered representative of long term values.

1.3.3 Internal Waves

Internal waves are fluctuations which resemble waves at the ocean surface, but they can propagate vertically as well as horizontally, thus making disturbances at the surface or the bottom felt in the interior. They can be generated in the ocean by tidal and geostrophic currents interacting with boundaries and bottom topography (Sloyan, 2005), and by the action of the wind on the geostrophic and ageostrophic flows, and on surface waves (Kuhlbrodt et al., 2007). As internal waves propagate away from their source, energy spreads into waves with other periods and generally smaller vertical scales. This increases the vertical shear - the vertical gradient of horizontal currents - which increases the likelihood that the waves will break, thus

promoting turbulence and diapycnal mixing (Garrett, 2003). It has recently been demonstrated that this cascade is more vigorous not only when internal waves are more energetic, but also at high latitudes, due to the dependence of the dominant frequency of the internal waves on the Coriolis parameter (Gregg et al., 2003; Kunze et al., 2006).

There are two main methods by which internal waves can be generated: wind forcing, and the movement of water over rough topography. Wind forcing generates near-inertial motions, and although the large inertial oscillations seen in near-surface waters decrease in amplitude rapidly with depth below the mixed layer (Pollard, 1970; Pollard and Millard, 1970), they do penetrate somewhat into the ocean interior as internal waves (D'Asaro, 1984; Alford, 2001, 2003a). In principle, any movement of water over rough topography may generate internal waves (Bell, 1975; Baines, 1982). This can include the generation of internal waves with tidal frequencies, caused by the interaction of barotropic tidal currents with rough topography (see, for example, Garrett and St Laurent, 2002; St Laurent and Garrett, 2002; Garrett and Kunze, 2007; Heywood et al., 2007), and the generation of lee waves by geostrophic flows (Nikurashin and Ferrari, 2010a,b) over rough topography, particularly in the Southern Ocean where bottom geostrophic flows are much more intense than in most other ocean basins.

The mean flow can also interact with the internal wave field. This might involve the generation, trapping, or amplification of internal waves (Kunze and Sanford, 1984; Kunze, 1985), or alternatively the transfer of energy from the internal wave field to the mean flow (Waterman et al., 2012b).

1.3.4 Energy Budget

Consideration has also been given to the energetics of diapycnal mixing, as an energy input is required to enable water to cross the density surfaces and increase the potential energy of the fluid (Wunsch and Ferrari, 2004). Munk and Wunsch (1998) estimate that 2.1 TW (terawatts, 10^{12} W) are required for mixing to balance the formation of deep water, which occurs at a rate of approximately 30 Sv (Sverdrups, 10^6 m^3 s^{-1}). A number of authors have considered the work done by the wind on the oceans: Wunsch (1998) estimated the work done on the surface geostrophic flow to be about 1 TW; Wang and Huang (2004a) estimated the work on the ageostrophic flow at about 3 TW; Wang and Huang (2004b) estimated the work on surface waves at about 60 TW, but they point out that a large fraction of this energy is bound to be dissipated in the surface layer. In total, a rough estimate of the wind energy

input to abyssal turbulent mixing (as opposed to dissipation by other processes) is 1 TW (Kuhlbrodt et al., 2007). Tides are known from astronomy to supply 3.7 TW (Le Provost and Lyard, 1997), and although much of this is dissipated in marginal seas, it has been estimated that 0.6 - 0.9 TW are available for abyssal mixing (Egbert, 1997). Thus the amount of energy available for mixing appears to be approximately consistent with that required, at least within the fairly large uncertainties on the various estimations.

Toggweiler and Samuels (1995, 1998) present an alternative explanation in which much of the upwelling of North Atlantic Deep Water is accomplished by Ekman suction due to the strong winds over the Southern Ocean at the latitude band of Drake Passage. The northward surface flow driven by the winds can only be balanced by southward geostrophic flow below ~ 1500 m due to the requirement for topographic ridges to support east-west pressure gradients. The reduction in density then occurs primarily by surface freshening, which leads to a requirement of only around 0.6 TW for abyssal mixing (Webb and Suginohara, 2001). Wunsch and Ferrari (2004) point out that while this may be an important process in the upper ocean (at least in the Southern Ocean and the tropics), concluding that most oceanic mixing takes place at the surface would conflict with the observed need for large mixing at depth, such as that found by Ganachaud and Wunsch (2000) and discussed above.

1.3.5 Model Studies

While many general circulation models (GCMs) have used uniform κ_z (such as the global average value of 10^{-4} m^2 s^{-1} suggested by Munk and Wunsch (1998)), it is becoming increasingly common to use a spatially varying κ_z. Many studies using spatially varying κ_z have concluded that it is a critical factor controlling the strength and structure of the circulation (see, for example, Marotzke, 1997; Huang, 1999; Zhang et al., 1999; Marzeion and Drange, 2006). To give a particularly large-scale example, Schmittner and Weaver (2001) point out that given the large uncertainty still remaining in observations of ocean mixing, such as the lack of regular global coverage, it is not currently possible to quantitatively determine the conditions which could act as thresholds for the North Atlantic overturning circulation to switch between “on” and “off” modes, with the subsequent significant alteration in surface climate experienced in surrounding regions.

Kuhlbrodt et al. (2007) point out that any model which employs fixed mixing coefficients disregards the questions, discussed above, about the energy supply

required for mixing to occur. This is supported by the work of Huang (1999), who used an idealized ocean basin with only thermal forcing to compare prescribed mixing coefficients with prescribed energy profiles from which diffusivities are calculated. He found different sensitivities of meridional mass and heat transport to the meridional temperature difference in these situations. Similarly, Nilsson et al. (2003) and Mohammad and Nilsson (2004), using a model where diffusivity was explicitly dependent on the local buoyancy frequency, suggested that the Atlantic meridional overturning circulation may actually be intensified by an influx of freshwater in the North Atlantic, a result which differs significantly from that found in the majority of models using uniform diffusivity.

Hasumi and Suginohara (1999) found that topographically enhanced mixing in a global ocean model with realistic topography and wind forcing affected the upwelling and circulation of the bottom to deep water masses. More recently, Saenko and Merryfield (2005) used a global GCM in which they first set the diffusivity to the 'background' level of 0.1 $\times 10^{-4}$ m^2 s^{-1} throughout, and then re-ran the model with the diffusivity set to much higher values over rough topography, reproducing the observed variation. The uniform, low diffusivity model was unable to reproduce observed circulation patterns: the deep North Pacific Basin became a stagnant pool, with only weak circulation in the upper layers; the ACC was much weakened; the rate of bottom water formation around Antarctica was significantly reduced. The second experiment, with more realistic diffusivity, produced much more realistic circulation in these areas. Most interestingly, Saenko (2006) showed that two climate models with the same vertical distribution of diffusivity but different horizontal distribution (horizontally uniform versus topographically enhanced) have different responses to atmospheric CO_2 increase. Due to differences in oceanic heat transport, "the CO_2-induced change of the surface climate simulated by the model with strong and uniform mixing is significantly weaker than that simulated by the model with strong but only locally enhanced mixing."

Thus, it is strongly suggested that diffusivity is an important controlling factor of the global ocean circulation, and thus the global climate and its future response to anthropogenic climate change. The present and future effects on the global climate of spatially and temporally varying diffusivity (and conceivably vice versa) remain a topic of extensive research, but it is clear that increased observational coverage will be beneficial to our understanding of these processes.

1.4 This Thesis

In this thesis, I present results from three different Southern Ocean studies. Firstly, the SOFine (Southern Ocean Finestructure) project investigated the standing meander in the ACC found on the northern flank of the Kerguelen Plateau (Figure 1.2). A cruise in November-December 2008 onboard the RRS James Cook collected data for this project. Station measurements included simultaneous CTD, LADCP, and microstructure measurements. Finescale and microstructure diffusivity estimates are discussed in Waterman et al. (2012a,b). In chapter 2, I discuss the hydrographic survey, front locations, and transport through this region. The motivation for this study was to further our understanding of the circulation in this highly variable and very undersampled region: the previous hydrographic survey here was carried out nearly 20 years earlier (Park et al., 1993).

Secondly, in chapter 3, I discuss diffusivity estimates in Shag Rocks Passage (Figure 1.2), including an 18-month time series of diffusivity calculated from data taken by an Acoustic Doppler Current Profiler (ADCP) moored at 2400 m depth, 600 m above the sea floor. The aims of this study were to develop a method which could, if applied more widely, give an assessment of the validity of snapshot diffusivity estimates, and to gain some initial understanding of the magnitude of temporal variability of diffusivity. The mooring was placed in Shag Rocks Passage as part of the North Scotia Ridge Overflow Project (Smith et al., 2010). The diffusivity estimates I present here represent, to my knowledge, the first long, deep-ocean time series of diffusivity. I discuss processes that may contribute to the temporal variability of diffusivity estimates in this region. Additionally, chapter 4 contains supplementary material for this study.

Thirdly, chapter 5 contains an assessment of density-based fine-structure methods for estimating diapycnal diffusivity, i.e., relatively *inexpensive* methods of estimating diapycnal diffusivity, with the intention of determining whether these methods give accurate results in the Southern Ocean. The data used was collected as part of the Diapycnal and Isopycnal Mixing Experiment in the Southern Ocean (DIMES). DIMES' joint US/UK field program included tracer release, isopycnal following RAFOS floats, microstructure measurements, shearmeter floats, EM-APEX floats, a mooring array in Drake Passage and hydrographic observations, supplemented by inverse modelling and analysis of altimetry and numerical model output. As part of this project, CTD and eXpendable CTD (XCTD) data were collected, during a cruise on the R/V Thomas G. Thompson in October-December 2010, in Drake Passage and the abyssal plain in the southeastern Pacific region of

the Southern Ocean (Figure 1.2). The CTD/XCTD data is used to assess the Thorpe scale and strain variance methods for estimating diffusivity.

Finally, chapter 6 summarises the results of these three studies, and discusses possible future work which could expand on the results presented here.

Chapter 2

Direct Observations of ACC transport on the northern flank of the Kerguelen Plateau

This chapter has been accepted by the Journal of Geophysical Research - Oceans.

citation: Damerell, G. M., K. J. Heywood, D. P. Stevens, 2013: Direct Observations of ACC transport on the northern flank of the Kerguelen Plateau. J. Geophys. Res., in press.

2.1 Abstract

The standing meander in the Antarctic Circumpolar Current found on the northern flank of the Kerguelen Plateau was investigated during the SOFine (Southern Ocean Finestructure) cruise in November-December 2008. An 18-year time series of surface geostrophic currents from satellite altimetry shows that the meander as observed during this survey is typical of the region. Hydrographic stations were occupied between 65-75°E, 43-48°S on the shelf (∼200 m depth) and slope into the deep ocean to the north of Kerguelen (∼4700 m), providing the most detailed survey of this region to date. Geostrophic shears are referenced to lowered acoustic Doppler current profiler velocities to give the first estimate of the total volume transport in this region, and the transport budget is closed around the survey box. The Subtropical Front, Subantarctic Front and a northern branch of the Polar Front together have an associated transport of 174 ± 22 Sv eastward. While 174 Sv is large compared with typical Drake Passage transports, it is reconciled with

other estimates of the total transport with the additional 15 Sv of the Indonesian Throughflow. Baroclinic transport referenced to the deepest common level between station pairs is 119 Sv, consistent with other estimates of the baroclinic transport in this area. At this longitude the fronts of the Antarctic Circumpolar Current are exceptionally close together. We discuss the exchange of properties across the fronts.

2.2 Introduction

The Kerguelen Plateau is a volcanic ridge which forms the largest submarine plateau in the Southern Ocean (Fig. 2.1). It spans approximately 16° in latitude, from ∼65°E, 46°S, south-east to ∼85°E, 62°S, and is divided, at around 55-57°S, into the Northern and Southern Kerguelen Plateaus (NKP and SKP) by the Fawn Trough (FT), which has a sill depth of ∼2600 m. The NKP includes the Kerguelen Islands towards the north end, and the Heard/McDonald Islands towards the south. Further south, at 85°E, 63-66°S, the Princess Elizabeth Trough (PET, sill depth ∼3750 m), lies between the SKP and Antarctica.

The circulation around the plateaus and the flows through locally deeper troughs in the plateaus have long been a topic of study, yet many aspects remain to be quantified. Fig. 2.1 provides a synthesis of the historical studies listed in Table 2.1. Fig. 2.1 and Table 2.1 together summarize the main currents in the Indian Ocean sector of the Southern Ocean, as well as the flows around the Crozet and Kerguelen Plateaus. This is not a definitive collection of all studies in this region, simply a summary based, where possible, on more recent studies in which the use of Acoustic Doppler Current Profilers (ADCPs) to reference geostrophic shear allows estimates of total geostrophic transport. The hydrographic survey of Park et al. (1993) in the Crozet Basin (which included the region north of the Kerguelen Plateau discussed in the current study) did not use ADCPs and so found transport relative to the deepest common level, which we will henceforth refer to as baroclinic transport.

The Kerguelen Plateau constitutes a significant topographic barrier for the Antarctic Circumpolar Current (ACC). The ACC is associated with several main eastward flowing frontal jets, generally designated as the Subantarctic Front (SAF), Polar Front (PF), Southern ACC Front (SACCF) and Southern Boundary (SB) of the ACC (Orsi et al., 1995). Table 2.2 lists hydrographic characteristics by which these fronts are typically identified. Throughout this chapter, we use conservative temperature and absolute salinity rather than in-situ or potential temperature and practical salinity (IOC et al., 2010), though both practical and absolute salinity are given in Table 2.2 to facilitate comparison with other works. Conservative temperature in this region differs from potential temperature by a maximum of 0.02°C and an average of 2×10^{-5} °C, so they can be treated as virtually identical. We also use water mass definitions based on neutral density (γ^n, in kg m^{-3}, as defined by Jackett and McDougall (1997)), with consideration also given to definitions based on hydrographic properties (Table 2.3). The units of density (kg m^{-3}) are omitted henceforth.

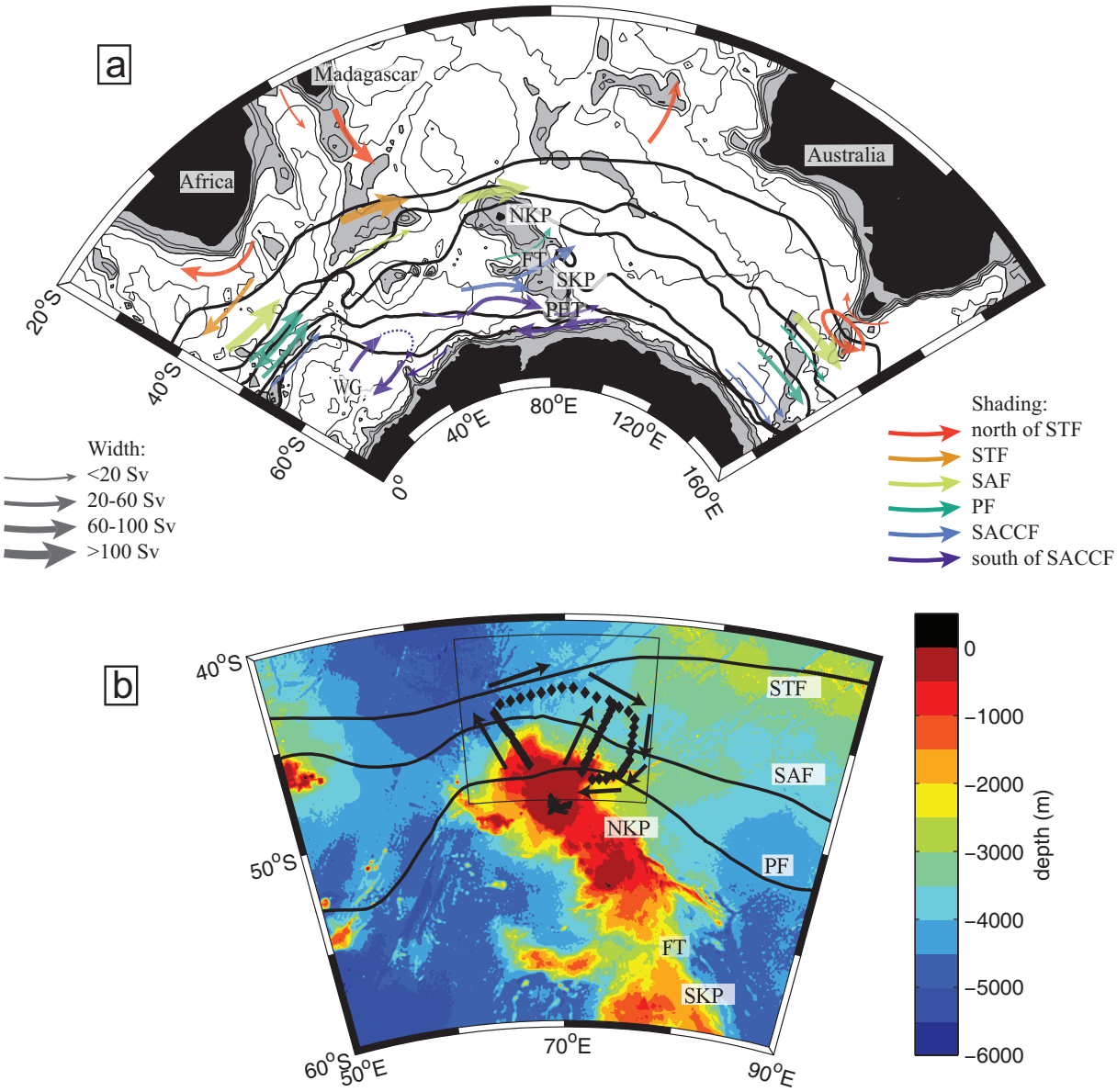

Figure 2.1: a) Regional map, with smoothed bathymetry from Smith and Sandwell (1997). Contours are every 1000 m, with grey shading to 3000 m deep. Various topographical features are indicated: NKP=North Kerguelen Plateau, SKP=South Kerguelen Plateau, FT=Fawn Trough, PET=Princess Elizabeth Trough. WG refers to the Weddell Gyre. Arrows represent currents from a variety of studies, listed in table 2.1. The width of the arrows represents the top-to-bottom transport, and the shading the north-south position relative to the main ACC fronts. Where the arrows representing the Weddell Gyre are dotted, the flow pattern is inferred due to the lack of observational data. The thick black lines are the climatological mean positions of the fronts from Orsi et al. (1995): from north to south, the STF, SAF, PF, SACCF and SB. b) Bathymetry of the NKP, showing the location of the stations occupied in the SOFine survey (black diamonds). The seven black arrows indicate the direction of the ship track along the seven transects, which is the order in which stations are shown in subsequent figures plotted against depth. The thin black lines outline the area shown in subsequent plan view figures. Topographic features and climatological mean positions of the fronts are indicated as in (a).

Table 2.1: Front locations and transports in the Indian Ocean from various hydrographic surveys, as shown in Fig. 2.1. Here listed from west to east, and from south to north. HS=hydrographic survey, GVs=geostrophic velocities.

Location	Data	Fronts/Transport	Reference
SR2, from S. Africa to Antarctica, ∼10°E	HS in 2004. GVs referenced to LADCPs.	SACCF at 53°S, 12 Sv. Two branches of PF at ∼50 & 52°S (33 & 30 Sv respectively), with westward flow (-28 Sv) between. SAF at $\sim 43-49$°S, 107 Sv. Bottom intensified westward flow beneath STF, plus eddies (Agulhas leakage) give total transport of -42 Sv between 43°S and the coast of Africa.	Gladyshev et al. (2008)
Weddell Gyre at 30°E, south of 58°S	Two HSs in 1993 and 1996. GVs referenced to VMADCP at 50 m depth.	Weddell Gyre transporting ∼40 Sv between 58-65°S, and ∼-40 Sv (i.e., westward) between 65-69°S.	Park et al. (2001)
Region south of 60°S, and 30-80°E	HS in 2006. Transport calculated from LADCP velocities.	ASF at 30°E, 67-69°S, -18 Sv. ASF at 80°E, 65-66°S, -28 Sv. SB at 50°E, 62-65°S, 15 Sv. SB and SACCF at 80°E, 62-65°S, >40 Sv. Difficulty estimating the transport of the Weddell Gyre as it appeared to break mass conservation.	Meijers et al. (2010)
25°S, Africa to Madagascar	Hydrographic inverse box model.	14 ± 6 Sv southward.	Ganachaud et al. (2000)
Crozet Basin, 40-80°E, 37-52°S	HS in 1991. GVs referenced to deepest common level.	SAF/PF, 47-50°S 50-55°E (north of Crozet), 15 Sv. Shaded in Fig. 2.1 as SAF. ARF/STF /SAF, 41-44°S 50-55°E, 130 Sv. Shaded in Fig. 2.1 as STF. STF/SAF, 44-46°S 70°E, (north of NKP), 95 Sv. Shaded in Fig. 2.1 as SAF. ARF-waters peel off to north from 50-80°E, 35 Sv.	Park et al. (1993)
Fawn Trough (FT), 72-86°E, 53-58°S	HS in 2009. Transport calculated from LADCP velocities.	SACCF, 55-57°S, 43 Sv. PF, 55°S, just south of Heard/McDonald Islands, 6 Sv.	Park et al. (2009)
Flow in PET, 85°E, 63-65°S	HS in 1993 and 1994. GVs referenced to VMADCP at 100-400 m depth.	ASF and associated westward flow, 65-66°S, -45 Sv. SACCF and SB, 63-65°S, 11 Sv.	Heywood et al. (1999)
32°S across entire Indian Ocean Basin	Hydrographic inverse box model, using GVs referenced to LADCP/VMADCP.	Complicated structure with many local north-/south-ward flows. Summarised as 70 Sv southward in the western part of the basin, and 52 Sv northward in the eastern part. The arrows on Fig. 2.1 are merely in the centre of these broad regions and do not indicate locally intense flows.	McDonagh et al. (2008)
SR3, from Tasmania to Antarctica, ~ 140°E	6 HSs between 1991 and 1996. GVs referenced to 'best guess' reference level.	SACCF-south at 64°S, 11 ±3 Sv, SACCF-north at 62°S, 18 ±3 Sv. PF-south at 59°S, 24 ±3 Sv, PF-north at 53-54°S, 5 ±5 Sv. SAF at 51-52°S, 105 ±7 Sv. Subantarctic Zone Recirculation, ∼44-49°S, 22 ±8 Sv (net transport zero). Tasman outflow immediately south of Tasmania, -8 ±13 Sv.	Rintoul and Sokolov (2001)

Table 2.2: Summary of front identification criteria after Orsi et al. (1995); Sparrow et al. (1996), and used throughout unless otherwise stated in the text. Conservative temperature (Θ, in °C), absolute salinity (S_A, in g kg^{-1}) practical salinity (S_p, in psu) and dissolved oxygen (O_2, in μ mol l^{-1}).

Front	Criteria
Agulhas Return Front (ARF)	Θ range 12-16°C at 200m
Subtropical Front (STF)	$\Theta/S_A(S_p)$ ranges of 10-12°C and 34.77-35.17(34.6-35.0) at 100m
Subantarctic Front (SAF)	rapid descent of subsurface S-min to 500-600m depth
Polar Front (PF)- subsurface	northern terminus of 2°C isotherm below 200m
Polar Front (PF)- surface	max gradient of SST regime between 2 and 6°
Southern ACC Front (SACCF)	$\Theta >$1.8°C along Θ-max at depths >500m to the north $S_A(S_p) >$34.9(34.73) along S-max at depths >800m to the north $\Theta <$0°C along Θ-min at depths <150m to the south
Southern Boundary (SB)	southern limit of UCDW - high nutrient and low $O_2<$200 μmol l^{-1} at 27.35 $<\sigma_0 <$27.75

The extent of the ACC is usually defined in terms of the circumpolar waters that pass through Drake Passage. Further south are various gyres (e.g., Weddell Gyre, Ross Sea Gyre), and the Antarctic Slope Front/Current (ASF), found above the continental slope around most of Antarctica associated with a westward flowing frontal jet. North of the SAF is the eastward flowing jet associated with the Subtropical Front (STF), which separates Subtropical Surface Water (STSW) from Subantarctic Surface Water (SASW). Within the Indian Ocean sector of the Southern Ocean, the Agulhas Return Front (ARF) is found to the north of the STF. The ARF encloses the warm and saline thermocline waters of the subtropical gyre in the South Indian Ocean.

In the South Indian Ocean, Park et al. (1993) used CTD data, taken on a cruise in April-May 1991, to find the STF and SAF blended together on the northern flank of the Kerguelen Plateau, giving a concentrated jet centered at 44-45°S with a baroclinic transport of $\sim$100 Sv. (Their criteria for the SAF are, however, different to those in Table 2.2, being θ/S ranges of 4-8°C and 34.1-34.5 at 200m. They do, however, comment that at the southward edge of this jet there is a rapid descent of the subsurface salinity minimum, corresponding to the SAF definition of Orsi et al. (1995).) Sparrow et al. (1996), using the hydrographic atlas published by Olbers et al. (1992) and the same front definitions as Orsi et al. (1995), similarly find a blended STF/SAF on the northern flank of the Kerguelen Plateau with a baroclinic

Table 2.3: Water mass definitions by neutral density (γ^n, in kg m^{-3}, as defined by Jackett and McDougall, 1997) and various hydrographic properties: Θ, $S_A(S_p)$ and O_2 as in Table 2.2.

Water mass	γ^n	references	alternative criteria	references
Antarctic Bottom Water (AABW)	>28.27	Orsi et al. (1999)	Θ<0 $S_A(S_p)$<34.9(34.73) O_2>223	Heywood et al. (1999)
ACC Bottom Water (AACbw)	28.18-28.27	Orsi et al. (1999)		
Lower Circumpolar Deep Water (LCDW)	27.98-28.18	adapted from σ_0 in Heywood et al. (1999)	$S_A(S_p)$>34.87(34.7), nutrient min	Orsi et al. (1995)
Upper Circumpolar Deep Water (UCDW)	27.55-27.98	adapted from σ_0 in Sievers and Nowlin (1984)	O_2<200 nutrient max	Sievers and Nowlin (1984)
Antarctic Intermediate Water (AAIW)	27.13-27.55	Smith et al. (2010) & Heywood and King (2002)	S min	Deacon (1937)
Subtropical Surface Water (STSW)	<27.13		Θ>12 $S_A(S_p)$>35.27(35.1) O_2<270	Park et al. (1993)
Subantarctic Surface Water (SASW)	<27.13		5<Θ<9 $S_A(S_p)$<34.16(34.0) 290<O_2<315	Park et al. (1993)
Antarctic Surface Water (AASW)	<27.13		Θ<5 $S_A(S_p)$<34.16(34.0) O_2>315	Park et al. (1993)

transport of $\sim$110 Sv.

The location of the Polar Front (or Fronts) is considerably more in question. It is now fairly common to consider a surface and subsurface expression of the PF in hydrographic surveys, as was done by Sparrow et al. (1996). Several studies have argued that each of the three primary ACC fronts actually consists of multiple branches or filaments (for example, Holliday and Read (1998), Sokolov and Rintoul (2007) and Sokolov and Rintoul (2009)). The flow through the FT has been ascribed to the surface expression of the PF (or south PF) (Sparrow et al., 1996; Moore et al., 1999; Holliday and Read, 1998; van Wijk et al., 2010), multiple branches of the PF and SACCF (Sokolov and Rintoul, 2009), or the SACCF alone (Park et al., 2009). The latter, to our knowledge, describe the only survey to date which

crossed the FT and made use of direct current measurements from ADCPs, enabling them to find a total eastward transport of 43 Sv through the FT. Sparrow et al. (1996) and Holliday and Read (1998) place the subsurface expression of the PF to the north of the Kerguelen Islands, with warmer surface temperatures than the surface PF. Another group (Park et al., 1993; Charrassin et al., 2004; Park et al., 2008b,a, 2009; Roquet et al., 2009), report finding the subsurface PF broken into multiple filaments passing through various locally deeper troughs in the NKP with a combined transport of 8 Sv, none of which passes to the north of the Kerguelen Islands. van Wijk et al. (2010) infer the presence of the subsurface PF (or north PF) to the north of the Kerguelen Islands, having found that front on the eastern side of the NKP with an associated baroclinic transport of 25 Sv to the southeast.

Moore et al. (1999) and Sokolov and Rintoul (2009) suggest that the location of the PF has varied over time. Using satellite observations of sea surface temperature (SST) Moore et al. (1999) mapped the location and dynamics of the surface PF from 1987 to 1993. The mean path of the surface signature of the PF goes through the FT, in agreement with Sparrow et al. (1996) and Holliday and Read (1998), but there is a very wide latitudinal range (nearly 10°), including, at times, north of the Kerguelen Islands, in agreement with Orsi et al. (1995). The analysis of Sokolov and Rintoul (2009) is based on sea surface height (SSH) gradient fields from satellite altimetry data taken between 1992 to 2007. The feature they identify as the northernmost branch of the PF shifted from passing to the north of the Kerguelen Plateau between 1992-2003, to passing through the FT from 2004-2007, a meridional shift of nearly 10°. They link this to the increase in average SSH in the Southern Ocean, indicating that the fronts are moving poleward.

Prior to the Southern Ocean Finestructure project (SOFine) discussed here, there was a lack of high resolution hydrographic data in the region north of the Kerguelen Plateau. The survey discussed by Park et al. (1993) had a limited number of stations (16 stations in the area in which the SOFine survey had 60 stations), and the work of Orsi et al. (1995) and Sparrow et al. (1996) was based on hydrographic atlas data so give climatological means rather than a realisation over a short time period. No previous studies on the north flank of the Kerguelen Plateau, to our knowledge, have included ADCP measurements to provide a level of known motion, so assumptions of a level of no motion have been necessary. The location and transport of the PF - or at least a northern branch of the PF - is also uncertain. A further unknown is whether the merging/bunching of fronts in a narrow meridional extent leads to the exchange of properties across the fronts.

The organisation of this chapter is as follows: section 2.3 describes the data

and methods, section 2.4 discusses the various water masses observed, section 2.5 discusses the fronts and associated transports, section 2.6 discusses the total transport through the region and compares this with other observations in the ACC, section 2.7 discusses the horizontal and vertical exchange of properties, and section 2.8 contains the conclusions.

2.3 Data and Methods

The SOFine project studied an area on the northern flank of the Kerguelen Plateau, where two main jets of the ACC form a large standing meander in climatological atlases and ocean circulation models (Sparrow et al., 1996; Sokolov and Rintoul, 2009). The SOFine survey (Naveira Garabato, 2009), undertaken onboard the RRS James Cook (Cruise number JC029) in November and December 2008, consisted of two boxes. Three sections extended from the Kerguelen Plateau, and the boxes were closed by a land boundary (Kerguelen Island) to the south and an east-west transect to the north of the plateau slopes. Fig. 2.2 shows how the stations have been divided into transects, and also shows the approximate locations of the fronts, based on a combination of their hydrographic definitions (Table 2.2) and the locations of the current jets detected by geostrophy, and by ADCP measurements. These front locations will be discussed further in section 2.5. The 60 full-depth stations were separated by an average distance of 36 km with finer sampling over steep topography and fronts.

Station measurements included simultaneous CTD and LADCP measurements. Microstructure observations are discussed by Waterman et al. (2012a). The CTD was a Sea-Bird 9/11 *plus* system with fin-mounted secondary sensors. Water samples were taken for salinity calibrations using a Guildline Autosal 8400B, calibrated using OSIL IAPSO standard seawater batch P149. Accuracies were 0.001°C for temperature and 0.001 for salinity. Also mounted on the rosette was a Sea-Bird SBE-43 oxygen sensor. Samples were not analysed for dissolved oxygen during the cruise so the instrument is uncalibrated, but the values are consistent with climatology (Orsi, A. H., and T. Whitworth III, WOCE Southern Ocean Atlas, http://woceSOatlas .tamu.edu) and reproducible for overlapping transects, so no drift was detected during the cruise. CTD data were processed using Sea-Bird software SBE Data Processing, Version 7.18, and binned into vertical profiles of 2 dbar average temperature, salinity, oxygen, and pressure.

The LADCP package consisted of two RDI 300 kHz Workhorse ADCPs, though from station 16 onwards only one instrument (downward-looking) was used. No

LADCP data are available for stations 25 and 51. LADCP data were processed using software originating from Eric Firing's group at the University of Hawaii. The Visbeck software from Lamont-Doherty Earth Observatory (version 7b) was used for obtaining bottom tracked profiles. The bottom track profiles were used to confirm the output of the University of Hawaii software, but were otherwise not used. LADCP observations (averaged over the up and down cast) provided vertical

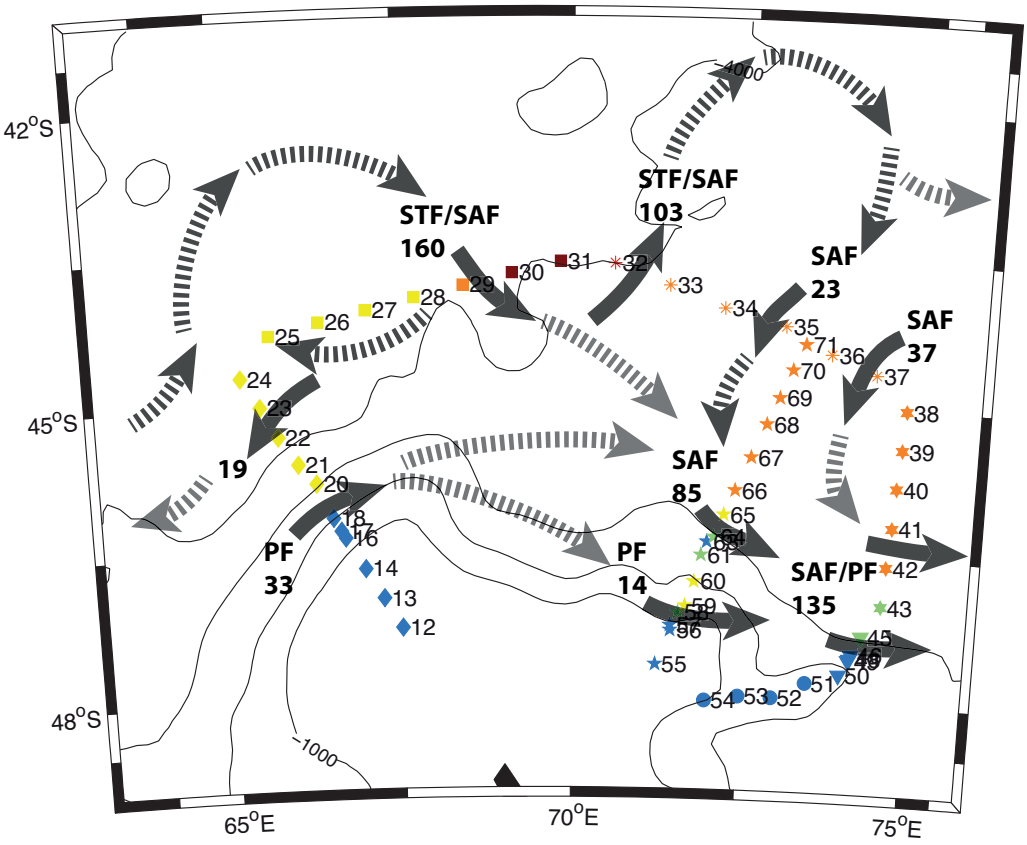

Figure 2.2: Station locations, with approximate jet locations and full-depth transports (Sv), as discussed in the text. Solid arrows indicate direct current measurements (LADCP). Black dashed arrows indicate areas where the surface current direction is taken from satellite altimetry, but we have no direct measurements of the full-depth transport from hydrographic sections. Grey dashed arrows indicate areas where the current direction is inferred; necessary because the currents as indicated by satellite altimetry are very weak, change during the course of the cruise, or are not consistent with mass conservation. Transects are shown as western (diamonds), northern transect I (squares), northern transect II (asterisks), eastern (6-pointed stars), south-eastern (triangles), southern (circles), and central (5-pointed stars). The colours indicate the surface water (based on the average properties of the top 100 m): blue = AASW, green = intermediate properties between AASW and SASW, yellow = SASW, orange = intermediate properties between SASW and STSW, red = STSW (see Table 2.3 for water mass definitions). The black lines are smoothed bathymetry contours every 1000 m.

profiles of 20 dbar average velocity. The LADCP profiles were detided using the ESR/OSU global inverse tide model TPXO7.2 (Egbert and Erofeeva, 2002). The effects of detiding are small: the total transport through the region (see section 2.6) is estimated as 171 Sv without detiding or 174 Sv after detiding, but the error estimate of $\pm$ 22 Sv is far greater than the difference caused by detiding.

The underway water sampling system consisted of a Falmouth Scientific Ocean Temperature Module (OTM) measuring the sea surface temperature (SST) at the water inlet, and a Falmouth Scientific OTM and Ocean Conductivity Module measuring temperature and conductivity in the wetlab. Two vessel mounted ADCPs (VMADCPs, 75 kHz and 150 kHz Ocean Surveyors), controlled using the RDI VmDas software, version 1.42, were run throughout the survey. The data were processed to remove bad data (e.g., from interference, bubbles, outliers), and to remove the instrument misalignments. Results from the two VMADCPs are consistent with each other, and from now on we use the data from the 75 kHz instrument, which can observe velocities down to approximately 800 m below the surface. The VMADCP profiles were similarly detided using the ESR/OSU global inverse tide model TPXO7.2 (Egbert and Erofeeva, 2002).

Geostrophic shear between adjacent station pairs, relative to the deepest common level, was calculated from the CTD data. Velocities perpendicular to the cruise track from the LADCP and VMADCP velocities were used to adjust the geostrophic shear in order to calculate the total geostrophic transport. Station pairs were divided into two groups: deep pairs, where both stations were deeper than 1500 m; and shallow pairs, where at least one station was shallower than 1500 m. For deep pairs, the depth range was selected where the shears of the LADCP and geostrophic profiles were in closest agreement, which involved excluding depths below the deepest extent of the shallower station, and depths from the surface to between 300 and 600 m. Selection of the near-surface depth range to exclude was done heuristically. The offset between the geostrophic profile and the average of the two LADCP profiles was then used to adjust the geostrophic current. These offsets were confirmed by comparison with the VMADCP profiles between the two stations. For shallow pairs, depths from the surface to between 100 and 400 m were excluded, and offsets were calculated from the average of all the LADCP and VMADCP profiles, including depths below the deepest extent of the shallower station. The station pairs with only one LADCP profile were treated in the same way as shallow station pairs. To join the end of the central transect to northern transect II (Fig. 2.2), the 'deep pair' process was also followed for stations 35 and 70, and stations 70 and 36.

The transport through 'bottom triangles' (the region below the deepest common level of two adjacent CTD stations where it is not possible to calculate geostrophic velocities directly) was calculated by extrapolating a constant geostrophic velocity below the deepest common level. Other methods were tested, such as extrapolating the geostrophic velocity gradient, or extrapolating the geopotential anomaly of the shallower station downwards (Thompson and Heywood, 2008). Very little difference was found using these alternative methods since the currents are not bottom-intensified in this region. A constant velocity gradient assumption, for example, makes a difference of only 1 Sv to the 160 Sv transport of the combined SAF/STF (see section 2.5).

The main source of uncertainty in the transport estimate is in determining the reference barotropic velocity from the ADCP data. The characteristic accuracy of the barotropic component of the ADCP flow, or, in other words, the uncertainty in referencing the geostrophic shear to the ADCP velocities, is 3 cm s^{-1} (Thompson and Heywood, 2008). To estimate error bars we apply random barotropic perturbations following a normal distribution with a standard deviation of 3 cm s^{-1} to individual velocity profiles. The error is then determined by calculating the rms deviation of 10,000 realizations of the resulting transport, and it is values calculated in this way which are quoted in sections 2.5 and 2.6.

An 18 year time series, from January 1993 to December 2010, of absolute geostrophic velocities calculated from sea surface heights above geoid obtained by satellite altimetry, was acquired from Aviso (Archiving, Validation and Interpretation of Satellite Oceanography). These are weekly gridded fields obtained on a $1/3°$ Mercator grid at 7-day intervals. The delayed-time (M)ADT 'Ref' products are used; a homogeneous data set based on two simultaneous satellite missions. These were used to produce weekly maps of geostrophic velocities in the SOFine survey region.

2.4 Water masses

The most voluminous density class found here is that of LCDW ($27.98 < \gamma^n < 28.18$, see Table 2.3), distinguished by a pronounced salinity maximum (Figs. 2.3d & 2.4). In those parts of the central, eastern, and the two northern transects that lie to the north of, or within, the SAF (see Fig. 2.2 and section 2.5 for front locations), water with the density of LCDW might more properly be labeled as North Indian Deep Water (NIDW) (Gordon et al., 1987), as is suggested by the low oxygen content (Figs. 2.4b & 2.5b). NIDW is an aged form of NADW, characterized by a relatively

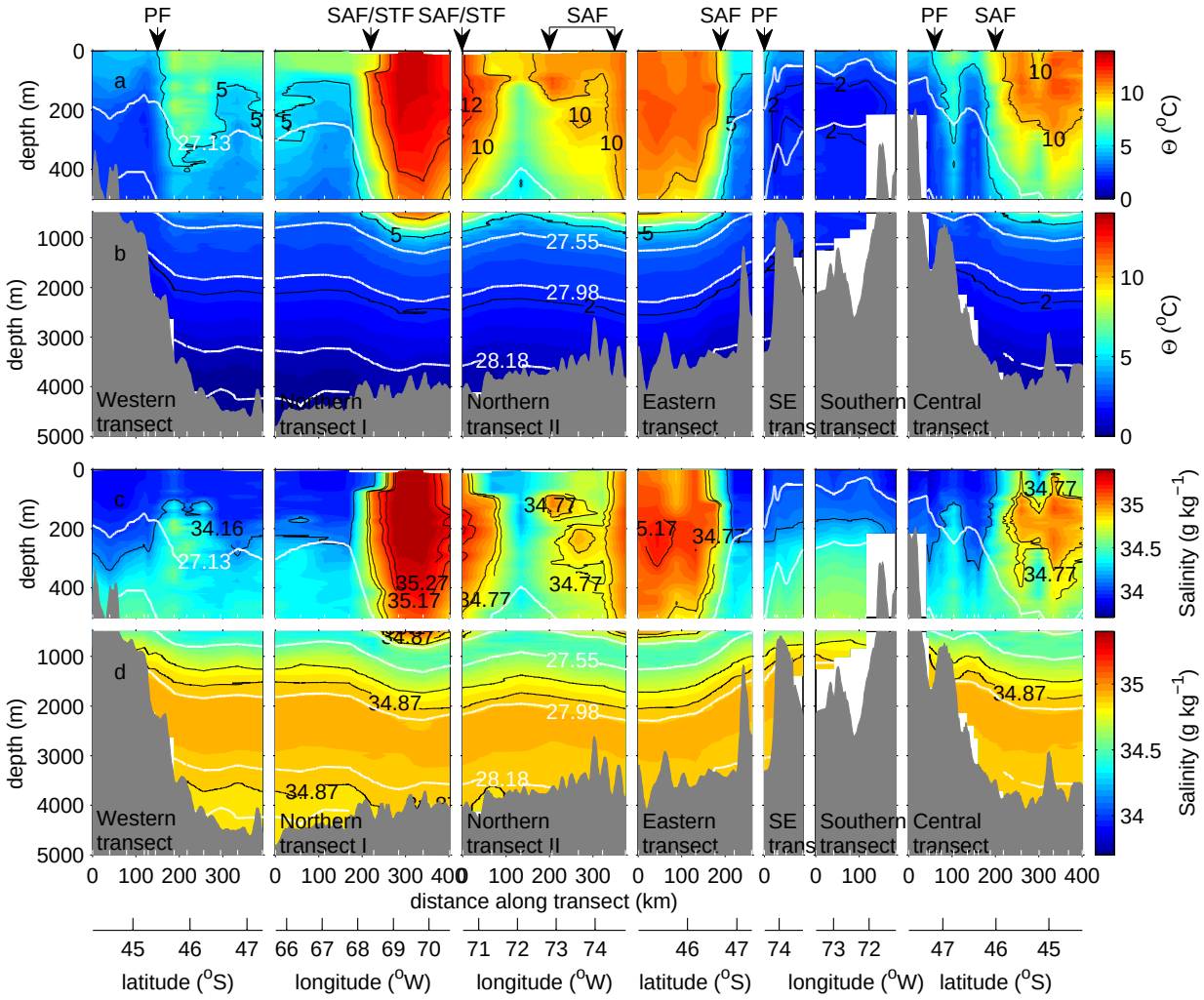

Figure 2.3: Temperature and salinity from the SOFine survey. Fields are displayed as a function of depth and along-transect distance, and the section as displayed starts in the southwestern corner of the survey domain, then runs clockwise along the rim of the region, and finally northeastward along the central transect. In all panels, neutral density contours (white) separate the water masses, according to the definitions in table 2.3. White tickmarks along the lower axis show the station locations and the fronts are identified along the upper axis [Polar Front (PF), Subantarctic Front (SAF), Subtropical Front (STF)]. (a) Conservative temperature between 0 and 500 m depth. (b) Conservative temperature between 500 and 5000 m depth. In (a) and (b), black contours show temperatures of interest for frontal and water mass definitions (2, 5, 10 and 12°C) according to the definitions in tables 2.2 and 2.3. (c) Absolute Salinity between 0 and 500 m depth. (d) Absolute Salinity between 500 and 5000 m depth. In (c) and (d), black contours show salinities of interest for frontal and water mass definitions (34.16, 34.77, 34.87, 35.17 and 35.27 g kg^{-1}) according to the definitions in tables 2.2 and 2.3.

low oxygen and high nutrient content, formed in the Indian Ocean basin. The particular hydrographic properties of NIDW are caused mainly by mineralization

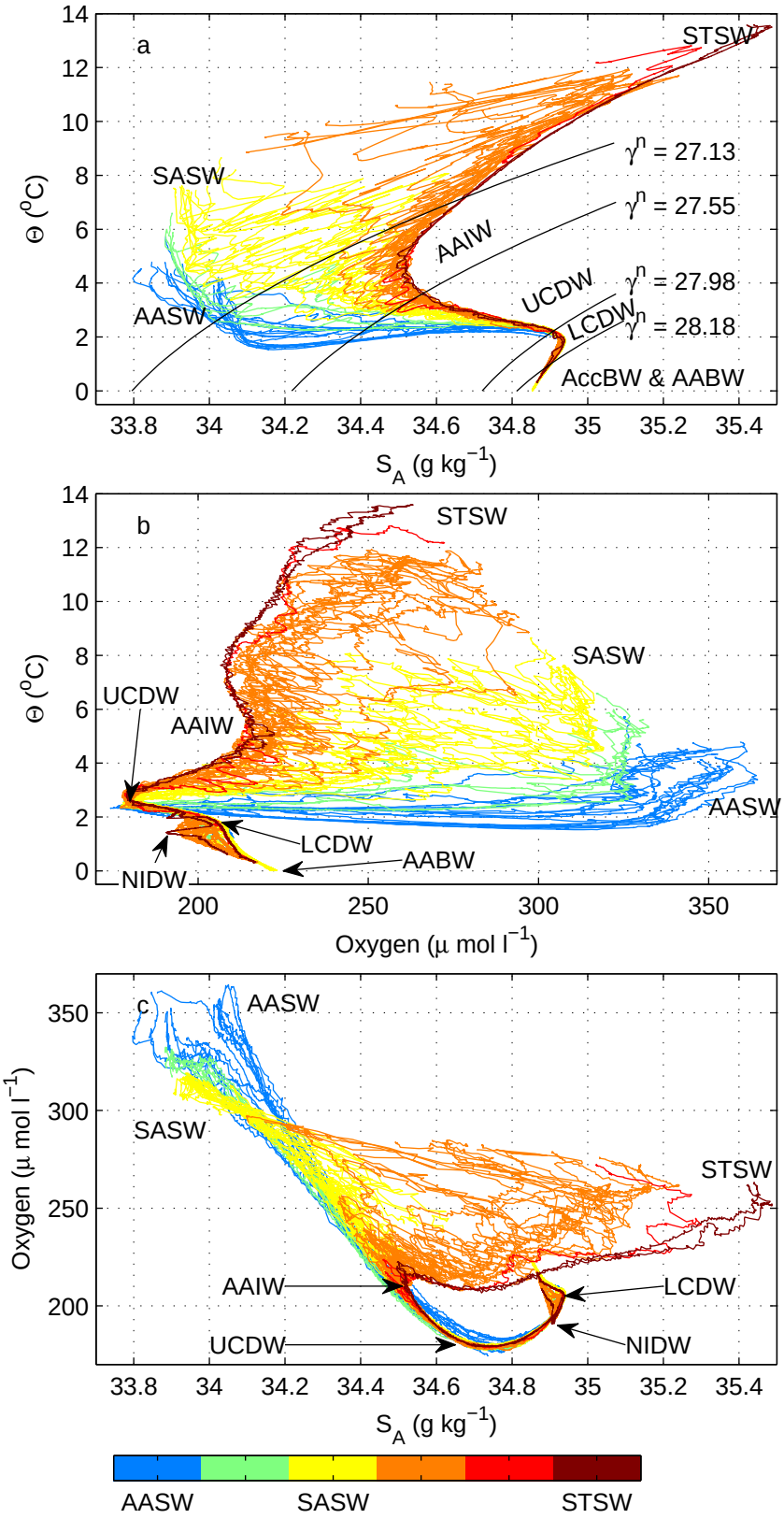

Figure 2.4: CTD Θ-S_A (a), Θ-oxygen (b) and S_A-oxygen (c) diagrams. The colours indicate the nature of the surface water (based on the average properties of the top 100 m): blue = AASW, green = intermediate properties between AASW and SASW, yellow = SASW, orange = intermediate properties between SASW and STSW, bright red = one station which had surface properties very close to STSW, except that it was slightly fresher, dark red = STSW (See table 2.3 for water mass definitions).

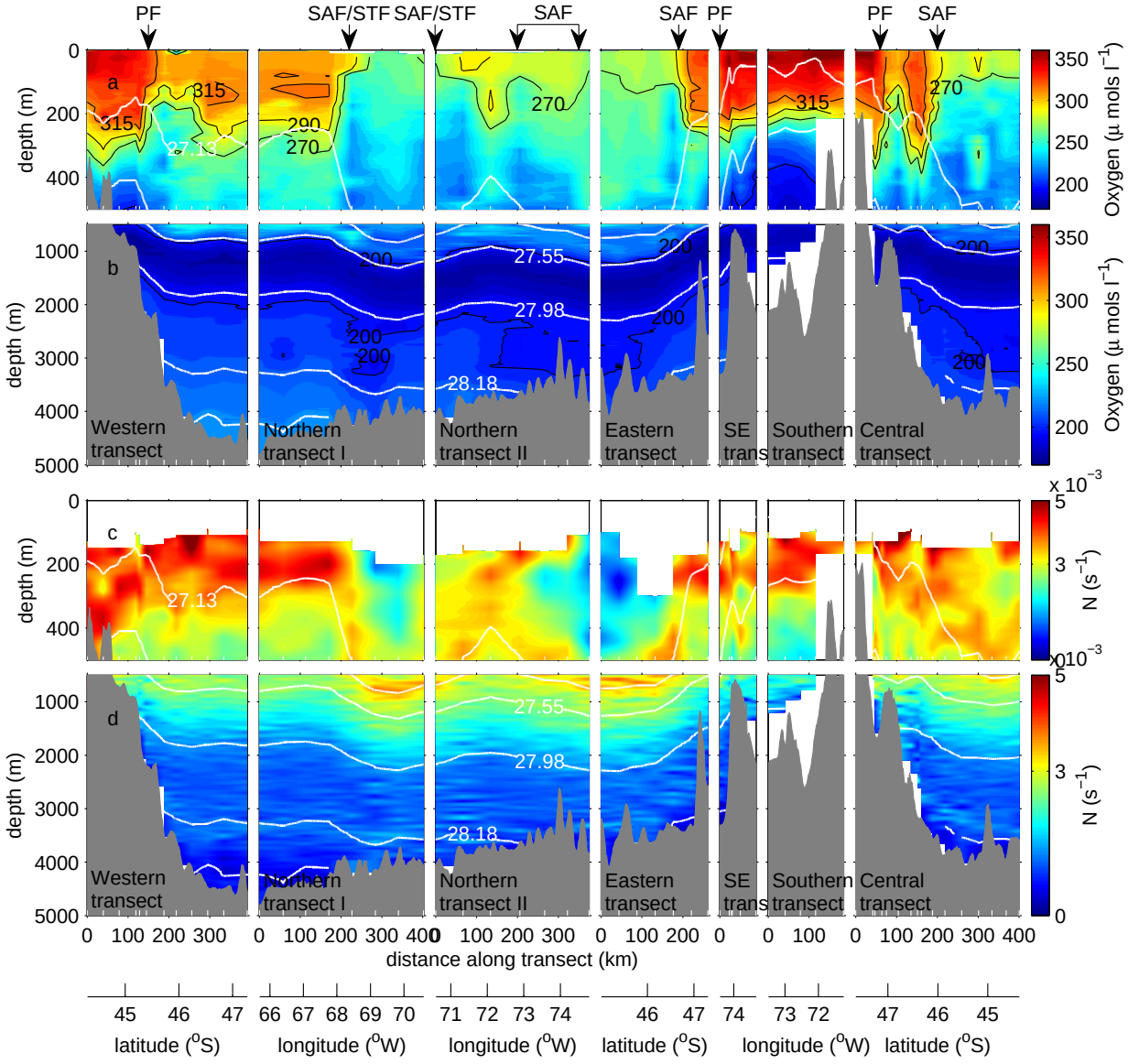

Figure 2.5: Dissolved oxygen and buoyancy frequency from the SOFine survey. This figure is laid out as in figure 2.3. (a) Dissolved oxygen between 0 and 500 m depth. (b) Dissolved oxygen between 500 and 5000 m depth. In (a) and (b), black contours show concentrations of interest for water mass definitions (200, 270, 290 and 315 μ mol l^{-1}) according to the definitions in table 2.3. (c) Smoothed buoyancy frequency (N) between 0 and 500 m depth. (d) Smoothed buoyancy frequency between 500 and 5000 m depth.

of organic matter (van Aken et al., 2004), unlike most major water masses which obtain their properties in the surface layers due to air-sea interaction. However, NIDW is usually treated as a separate water mass (Warren, 1981; Park et al., 1993; You, 2000; van Aken et al., 2004). Park et al. (1993) observed NIDW between 66° and 77°E at 38°S, and between 75-77°E at 43-41°S, north of their reported

position for the SAF/STF, and further north than observed in the SOFine survey. To our knowledge, this is the first observation of an injection of NIDW into the ACC on the northern flank of the Kerguelen Plateau. However, due to the scarcity of historical hydrographic data in this region, it would be premature to attribute this to a change in the deep circulation since it could simply be part of the natural climate variability.

Below the LCDW layer, and seen predominantly in the deeper areas of the western and northern transect I, is a water mass with densities in the range $28.18<\gamma^n<28.27$. This layer lies below the salinity maximum of LCDW, but waters of this density class are referred to by a number of different names in different locations: generally AABW in areas to the north of the ACC, Weddell Sea Deep Water within the Weddell Sea, and sometimes Modified CDW in areas to the south of the ACC (e.g., Meijers et al., 2010). We have chosen to designate this water mass as ACC bottom water (ACCbw) in line with Orsi et al. (1999). At the bottom of the western transect and northern transect I there is a thin layer of water with the density and salinity characteristics of AABW ($\gamma^n>28.27$, $S_A<34.9$ g kg^{-1}; Fig. 2.3d), though it is slightly warmer (Fig. 2.3b) and less oxygenated (Fig. 2.5b) than required by the hydrographic definition (Table 2.3).

Above the LCDW layer lies UCDW ($27.55<\gamma^n<27.98$), which has a pronounced oxygen minimum (Fig. 2.4b & 2.5b). This water mass appears thoughout the survey with fairly consistent salinity (Fig. 2.3d) characteristics, but the temperature (Fig. 2.3b) depends on the location relative to the PF. South of the PF (Fig. 2.2), the UCDW layer is colder, and considerably closer to the surface: $\sim$300-1200 m instead of $\sim$1000-2000 m to the north. Above the UCDW is a layer with the density ($27.13<\gamma^n<27.55$) of AAIW. South of the SAF, this is considered part of the surface waters, but the steep isopycnals in Fig. 2.3 show the subduction of this density class at the SAF. The subsurface salinity minimum characteristic of AAIW is clear north of the SAF, where the surface waters have high salinity (Fig. 2.3d).

The surface waters can be divided into broadly three types (Park et al., 1993). Subtropical Surface Water (STSW) lies to the north of the SAF, and is characterised by relatively high temperature and salinity (>12°C, >35.27 g kg^{-1}) and low oxygen content (<270 μmol l^{-1}). Subantarctic Surface Water (SASW) is characterized by lower temperatures and salinities (<9°C, <34.16 g kg^{-1}) and higher oxygen content (>290 μmol l^{-1}), and lies between the PF and SAF. Antarctic Surface Water (AASW) is colder (<5°C) and richer in oxygen (>315 μmol l^{-1}) and is found further south.

The different surface water characteristics lead to particularly noticable differences in the stratification of the near-surface waters. Fig. 2.5c-d shows the buoyancy frequency, smoothed by applying the adiabatic leveling method of Bray and Fofonoff (1981), with a pressure range of 100 db. North of the SAF, salinity and temperature increase towards the surface (but below the surface mixed layer) in a density-compensating manner, leading to weak stratification and a low buoyancy frequency in the STSW (N $\sim 1 - 2 \times 10^{-3}$ s^{-1}). At the base of this layer, the temperature decreases rapidly but the decrease in salinity is no longer rapid enough to be density-compensating (Fig. 2.4), leading to a band of higher stratification (N $\sim 3 - 4 \times 10^{-3}$ s^{-1}) at a density of $\sim$27.13 (Fig. 2.5c-d), the boundary between AAIW and the surface waters. South of the SAF, salinity decreases while temperature increases towards the surface (below the surface mixed layer), leading to much higher stratification in the SASW and AASW (N$\sim 4 - 5 \times 10^{-3}$ s^{-1}).

2.5 Fronts and Transport

A simplified schematic of the fronts and main water mass pathways is shown in Fig. 2.6; for more detail see Fig. 2.2. A combined SAF/STF (Table 2.2) crosses the northern transects in a meander to the south and then to the north (Figs. 2.2 and 2.6). This can be seen clearly in the sharp horizontal gradients in temperature and salinity (Fig. 2.3: the transects cross the 10-12°C and 34.77-35.17 g kg^{-1} bands at 100 m, coincident with the rapid descent of the subsurface salinity minimum). These coincide with strong jets in the currents southward and then northward (Figs. 2.7 & 2.8b), also seen in the surface geostrophic velocity fields derived from satellite altimetry (Fig. 2.9). The sharp horizontal change across this front in surface temperature and salinity is also evident in Fig. 2.7. However, we deduce from Fig. 2.10 that not all the water that enters in this meander (160 $\pm$ 18 Sv between stations 25 and 31) leaves again to the north (103 $\pm$ 13 Sv between stations 31 and 34). Some of this water, with the surface water characteristics of SASW (Table 2.3 and Fig. 2.2), is part of an eddy centered at approximately 70°E 43°S, seen clearly in the geostrophic velocity fields derived from satellite altimetry (Fig. 2.9), particularly during the early weeks of the cruise. Thus some of the 160 Sv entering between stations 25 and 31 travels west and leaves through the northern end of the western transect. We also surmise that some of the 160 Sv entering between stations 25 and 31 continues to the east, rather than returning north. This is reasonably consistent with the transports through the central (99 $\pm$ 10 Sv between station 55 and 70) and

eastern transects (135 ± 11 Sv between stations 38 and 46) being much greater than the transport through the western transect (33 ± 5 Sv from station 12 to 21, i.e., south of the westward flow associated with the eddy centered at approximately 70°E 43°S).

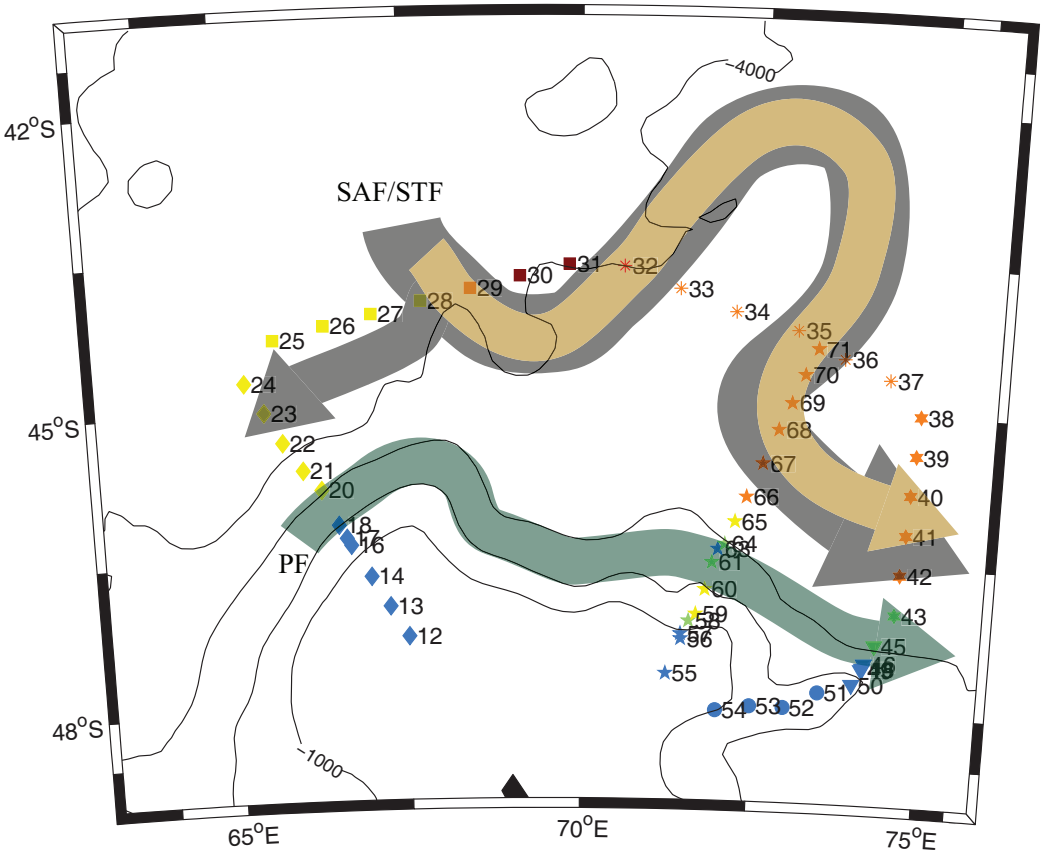

Figure 2.6: A simplified schematic of water mass pathways. Grey arrows show where all density classes are moving along the same pathway. The green arrow shows shallower waters only (UCDW, AAIW and surface waters). The orange arrow shows NIDW. Station locations are shown as in figure 2.2, with transects denoted by different symbols, and colours representing different suface water properties. The thin black lines are smoothed bathymetry contours every 1000 m.

Further east along northern transect II, a broad band of water enters the survey area heading southwest, seen in the velocity fields (Figs. 2.7 & 2.8) and in the altimetry-derived geostrophic currents (Fig. 2.9). The associated transport is 58 ± 14 Sv between stations 34 and 38 (Fig. 2.10). Fig. 2.3 shows a gradual descent of the subsurface salinity minimum across this transect, indicating that this is the SAF, and the surface waters have intermediate properties between SASW and STSW (Table 2.3 and Fig. 2.2). 37 ± 10 Sv crosses northern transect II to the east of the central transect (stations 70 to 38), and 23 ± 10 Sv to the west (stations 34 to 70),

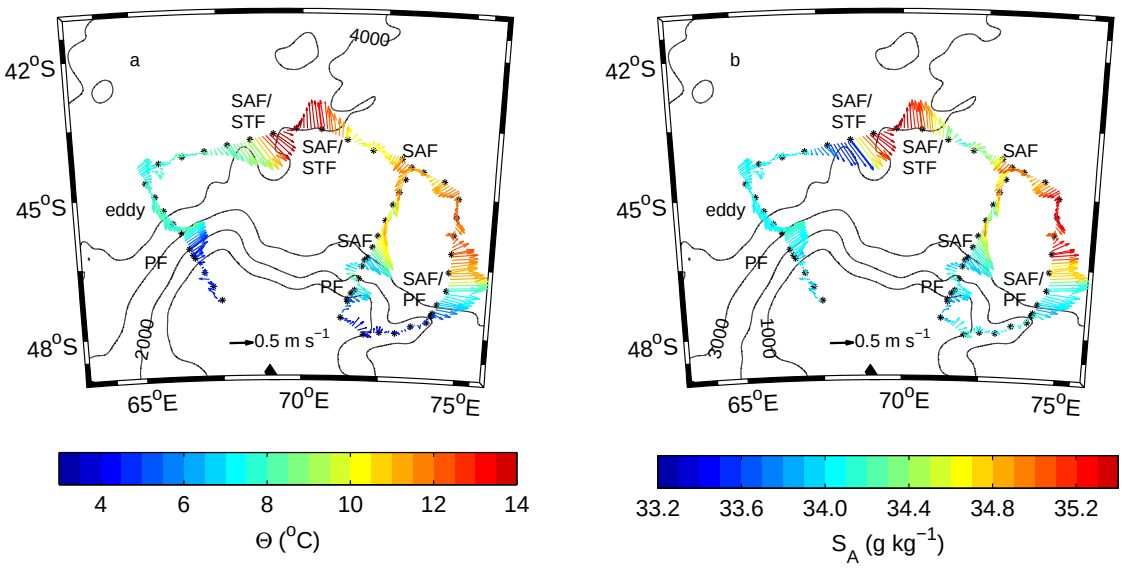

Figure 2.7: Current velocities observed by the 75 kHz VMADCP, averaged every 30 minutes, and over depths from 50-600 m where consistently good data was acquired. In (a), these are coloured by the SST, in (b) by the sea surface salinity (SSS) from the underway system. Front locations are indicated as follows: Polar Front (PF), Subantarctic Front (SAF), Subtropical Front (STF). The black lines are smoothed bathymetry contours every 1000m.

in good agreement with the 58 Sv from stations 34 to 38.

The altimetry-derived geostrophic currents (Fig. 2.9) show the broad SAF entering the survey area across northern transect II becoming a narrower, faster flowing jet at around 71°E, 46°S (an area not covered by the hydrographic stations), particularly during the early weeks of the cruise. This jet then bends around to cross the central transect in a south-easterly direction, and then the eastern transect flowing almost due east (particularly clear during the later weeks of the survey). This scenario, summarized in Figs. 2.2 and 2.6, is consistent with the velocities recorded by the ADCPs (Figs. 2.7 & 2.8), with the positions of the descent of the subsurface salinity minimum in Fig. 2.3, and with the large transports across the central and eastern transects. The transport across the central transect between stations 63 and 70 (i.e., the SAF), is 85 $\pm$ 9 Sv (Fig. 2.10). The sea surface salinity (SSS) of the water crossing the central transect (Fig. 2.7b) appears slighty fresher than in other jets which we consider to be the SAF, but we can see in Fig. 2.3c that there is a thin fresher layer at the surface in these areas, with more saline water beneath. This could be due to surface Ekman drift pushing fresher water northward across the frontal zone.

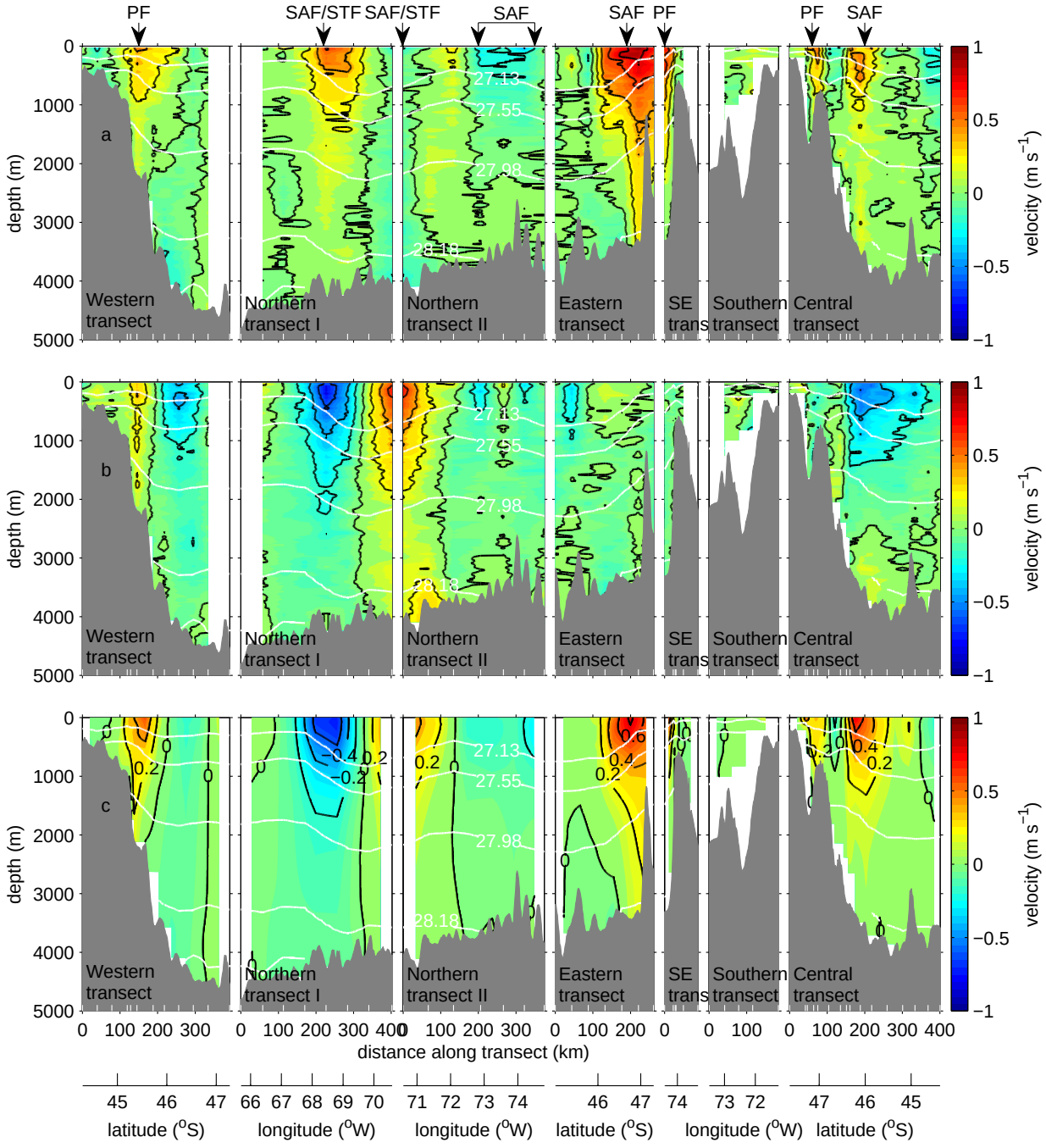

Figure 2.8: (a) eastward and (b) northward LADCP velocity, and (c) cross-track geostrophic velocity, referenced to the LADCP velocities (all m s^{-1}, colour). Fields are displayed as a function of depth and along-transect distance, and the section as displayed starts in the southwestern corner of the survey domain, then runs clockwise along the rim of the region, and finally northeastward along the central transect. In all panels, neutral density contours (white) separate the water masses, according to the definitions in table 2.3. White tickmarks along the lower axis show the station locations and the fronts are identified along the upper axis [Polar Front (PF), Subantarctic Front (SAF), Subtropical Front (STF)].

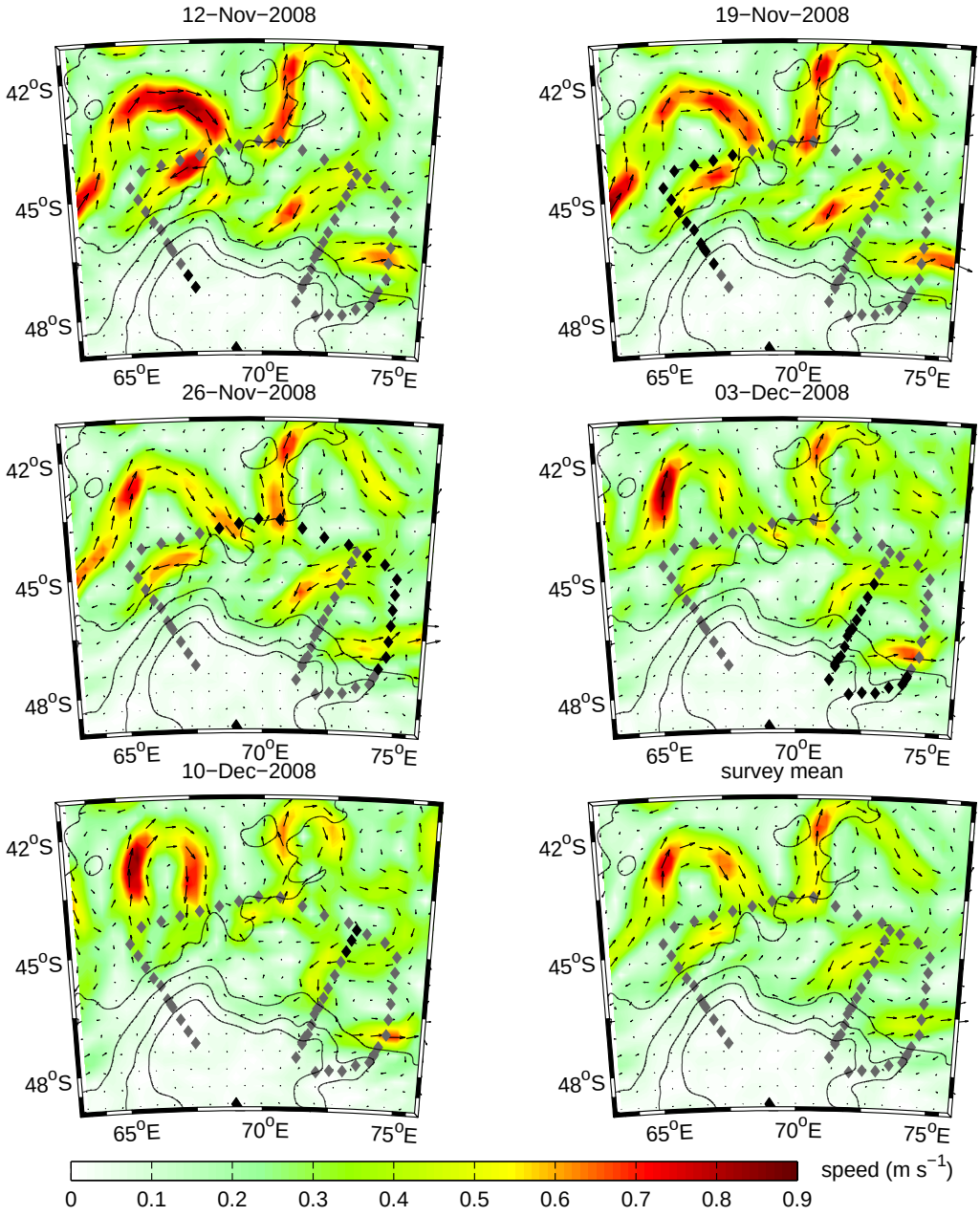

Figure 2.9: Geostrophic currents (black arrows) from satellite altimetry, with current speed in colour. These are the merged-satellites, gridded, absolute geostrophic velocities produced by Aviso. The black lines are smoothed bathymetry contours every 1000m. Diamonds show the station locations, with the stations occupied during the week represented by each altimetry map in black, and the other stations in gray.

South of the SAF, another jet crosses the western and central transects (Figs. 2.7 & 2.8a), becoming closer to the SAF as it travels east, until at the eastern transect there is no clear separation between the SAF and this more southern jet. We consider this to be the subsurface expression of the PF because the subsurface

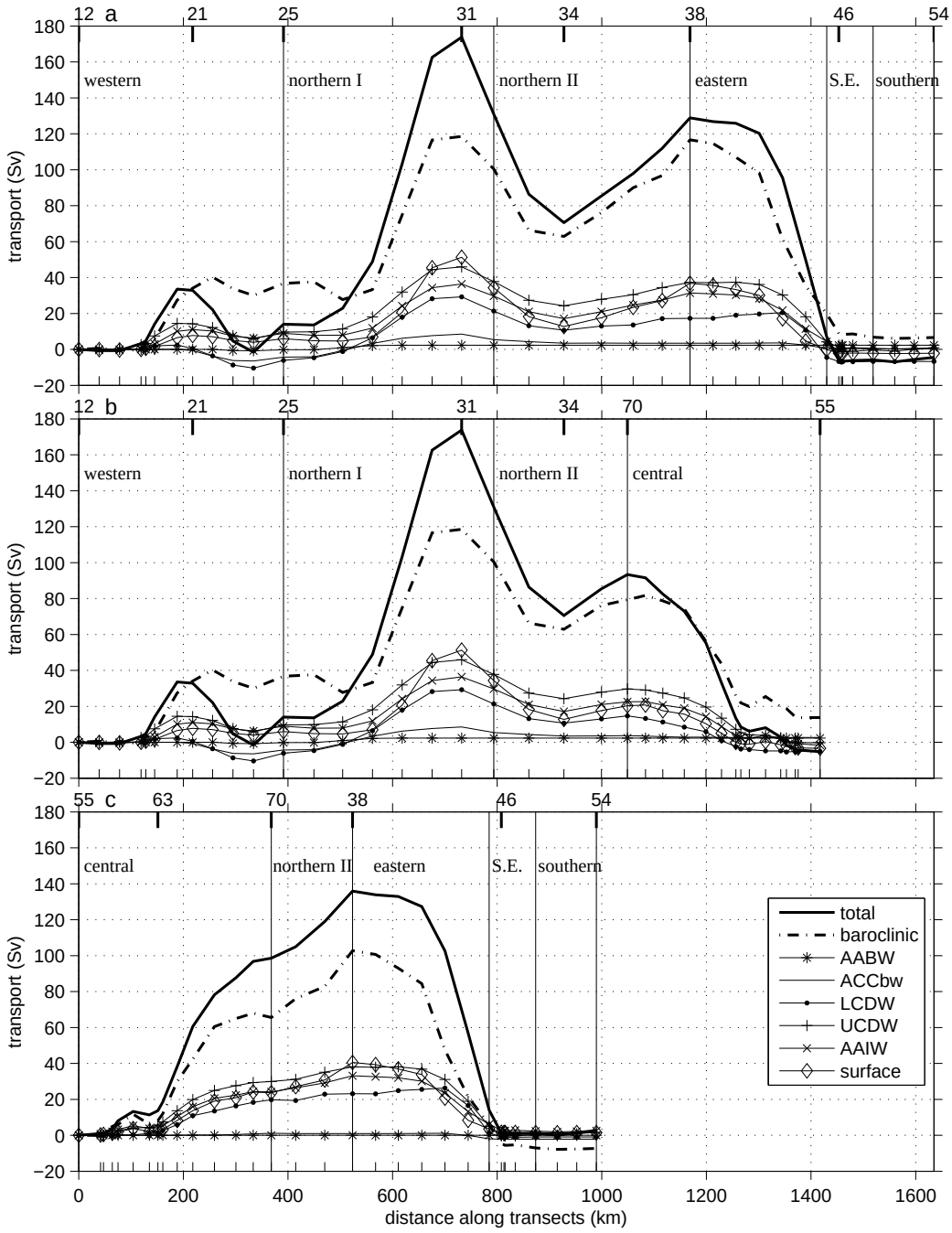

Figure 2.10: Transport of different water masses, summed over depth, around the 3 boxes formed by the survey. It is assumed that there is zero net transport over the shallow topography between the southernmost ends of the western and central transects. (a) The largest box from the western to the eastern transect, with the southern boundary partially closed by the southern transect, and partially by the above assumption. (b) The western box from the western to the central transect, with the southern boundary closed by the above assumption. (c) The eastern box from the central to the eastern transect, which is closed by the southern transect. All station locations are marked as ticks along the lower axis, with particular stations which are used to separate fronts marked on the upper axis. The dash-dot line in all three plots is the transport relative to the deepest common level.

2°C isotherm is found in the southeast (S.E.) and southern transects, just to the south of the location of this jet in the central and eastern transects (Fig. 2.3a). The subsurface 2°C isotherm is not present in the western transect, and presumably is located further south. In all three of the western, central and eastern transects there is a rapid descent of isotherms near the location of this southernmost jet, as is commonly found in the vicinity of the PF, and cold, highly oxygenated surface waters with the properties of AASW lie to the south (Table 2.3 and Fig. 2.2). Overall, this seems consistent with a northern branch of the PF, such as those found by Sokolov and Rintoul (2009) and Holliday and Read (1998). In the SOFine study region we do not find the surface expression of the PF, which was placed to the north of the Kerguelen Plateau by Orsi et al. (1995).

Crossing the western transect the transport of the PF between stations 12 and 21 is 33 $\pm$ 5 Sv (Fig. 2.10). Crossing the central transect the PF is associated with a transport of 14 $\pm$ 3 Sv between stations 55 and 63, although the rapid reversal in current direction (westward between the jets we associate with the PF and SAF) suggests that there may also be a small eddy in this region, making it difficult to accurately estimate the transport of a particular jet. In the eastern transect it is not possible to separate the SAF and PF. Overall, it is difficult to estimate the transport of the PF due to the merging of the fronts and presence of eddies, but it seems likely that it is more than zero, as was reported by Park et al. (1993, 2008a, 2009).

The altimetry-derived geostrophic currents do not always entirely agree with the currents found by the SOFine survey, particularly in the shallower areas of the survey region, and thus the jets we associate with the PF are not evident in Fig. 2.9. A possible explanation for this discrepancy is that the resolution of the gridded altimetric dataset is 1/4°, considerably coarser than the station spacing over the continental slope where the PF jets are found. We also suggest that both the tide model and the geoid (used in the calculation of absolute geostrophic velocity from sea surface height measurements) may be less accurate over the continental slope and shelf than in deep waters. Griesel et al. (2012) compare four Mean Dynamic Ocean Topography (MDT)products, in which the geoid is a major source of uncertainty. They find that the standard deviation of the four products reaches $\geq$20 cm in localized areas where MDT gradients are high and the surface flow is restricted by topography, such as near the Kerguelen Plateau.

The altimetry-derived geostrophic currents in the deeper (northern) parts of the survey region are in good agreement with the currents observed in the SOFine survey. Altimetry-derived geostrophic currents from January 1993 to December 2010 show that the currents observed in the northern parts of the SOFine survey

region are typical for this area. Large meanders and eddies are a persistent feature, though their precise location varies. This is further supported by eddy kinetic energy maps such as those discussed by Sallee et al. (2008); Trani et al. (2011), which show a relative maximum in eddy kinetic energy in the region of the Kerguelen Plateau. Unsteady jet behavior involving persistent jet formation and merging has been linked to interactions with eddies and topography (Thompson, 2008; Thompson et al., 2010; Thompson and Richards, 2011). In particular, Thompson (2010) demonstrate that topography does not simply steer jets in a passive manner, but can generate a range of patterns of unsteady jet behavior through modification of the mean flow and of local potential vorticity gradients and the subsequent feedback on baroclinic instability. Fig. 2.11a shows a broad band of high mean current speed across the northern part of the survey region, coincident with the location of the STF/SAF observed in the SOFine survey, and with the main jets in other hydrographic surveys (Park et al., 1993; Sparrow et al., 1996). The currents in this band are also the most highly variable in the survey region, evidenced by the high standard deviation of the speed (Fig. 2.11b). In the eastern part of this region, the currents in this band are slower and less variable. Moore et al. (1999) noted that large-scale meandering of fronts was inhibited near large topographic features because of the large gradients in planetary potential vorticity, which is consistent with the reduced variability in current speed observed as the main jet encounters the Kerguelen Plateau.

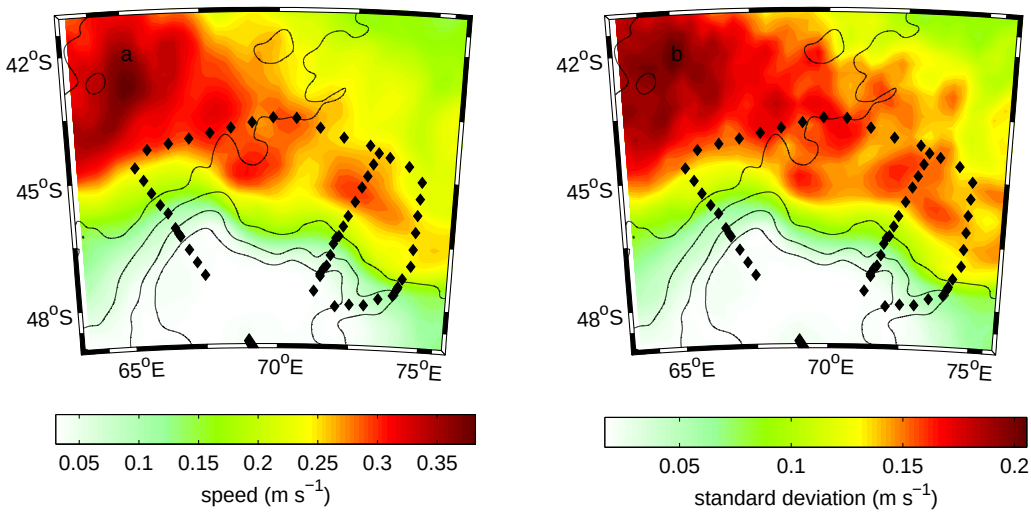

Figure 2.11: Altimetry-derived geostrophic currents from 1992-2010. The black lines are smoothed bathymetry contours every 1000m, and the black diamonds are the station locations. (a) mean speed, (b) standard deviation of the speed.

2.6 Total transport through the region

The baroclinic transport (i.e., calculated assuming a level of no motion at the deepest common level) through this region is 119 Sv (cumulative transport from station 12 to station 31), comparable with the baroclinic transports found by Park et al. (1993) and Sparrow et al. (1996) of $\sim$100 and 110 Sv respectively. The total transport through this region is 174 $\pm$ 22 Sv (cumulative transport from station 12 to station 31). An alternative, "worst case" scenario for estimating the error is obtained following Gordon et al. (2001) by assuming that all the LADCP profiles are systematically biased by 1 cm s^{-1}. This yields an error estimate of $\pm$ 39 Sv for the total transport between stations 12 and 31. The presence of the large eddy centered at approximately 70°E 43°S does not affect the total transport, because water associated with this eddy which enters the box across northern transect I also leaves the box across the northern end of the western transect.

At first glance, 174 Sv might seem rather large when compared with other ACC transport measurements, but in the SOFine region the transport associated with the ACC may be augmented by the $\sim$15 Sv of the Indonesian Throughflow (Sprintall et al., 2009) as it returns eastward. Moreover, we are not, in fact, measuring the transport of the ACC, since our survey encompasses the STF, which does not pass through Drake Passage, and does not cover the whole PF, nor the SACCF or SB. In addition, the SOFine survey is one snapshot measurement of a variable system, and may not be entirely representative of the long-term average. Several authors have shown that the barotropic component of the total transport can have high temporal variability (e.g., Cunningham et al. (2003)), although the altimetric observations suggest that the values found during the SOFine survey are unlikely to be significantly atypical.

The total cumulative transport between station 12 and station 31 of each watermass is shown in Fig. 2.12, with transport in neutral density layers. We compare these with the baroclinic transport of Rintoul and Sokolov (2001) calculated for five repeat sections along SR3 from Tasmania to Antarctica (their Plate 2), and the baroclinic and total transport found by Cunningham et al. (2003) for three repeat sections along SR1 across Drake Passage (their Tables 4 & 5). In the SOFine survey region, the total eastward transport of surface waters ($\gamma^n < 27.13$) is 51 Sv, far greater than that observed by Cunningham et al. (2003) in Drake Passage. The STF does not pass through Drake Passage, and we see in Fig. 2.10 that much of this surface water transport is associated with the combined STF/SAF, so the difference between this region and Drake Passage is not surprising. However, the

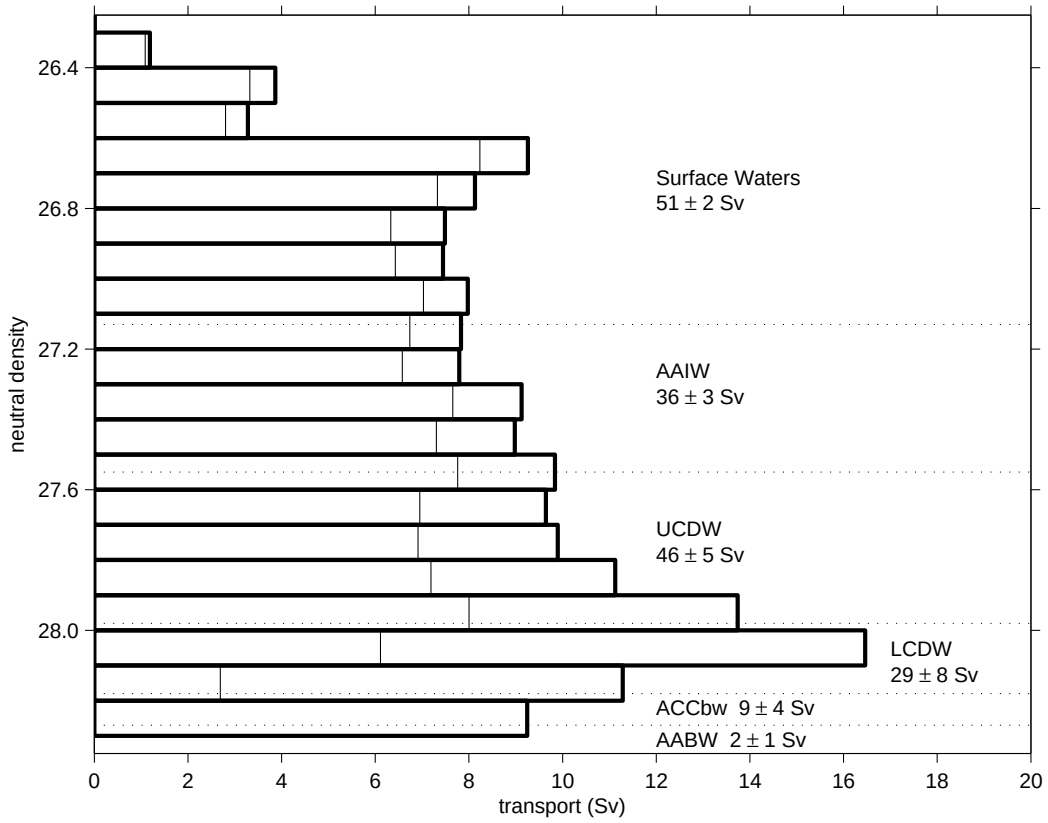

Figure 2.12: Transport in neutral density layers, summed from station 12 to station 31. The thick line is the total transport, the thinner line is the baroclinic transport. In the lightest density layer, the baroclinic transport hard to distinguish from the total because they are both 1 Sv. In the densest layer the baroclinic transport is zero. Dashed lines indicate water mass boundaries.

baroclinic transport of water with $\gamma^n < 27.13$, 45 Sv, is also significantly greater than that found by Rintoul and Sokolov (2001), whose survey does cross the STF. This may be partially due to the westward transport of light waters by the Tasman Outflow, offsetting some of the eastward transport of the STF, but we also speculate that some of this surface water may recirculate within the Indian Ocean basin.

The transport of AAIW and the lighter UCDW layers ($27.13 < \gamma^n < 27.8$) is broadly similar in all three regions (SR1, SR3, and the SOFine survey region), and across the various years of observation, with around 8-12 Sv for every 0.1 kg m^{-3}. In all three regions, the transport of water with γ^n in the range 27.8-28.2 is larger than other density layers, and particularly large in 1997 and 2000 in Drake Passage (74 and 93 Sv total transport respectively, compared with 53 Sv (total), 24 Sv (baroclinic), in the SOFine region (Fig. 2.12)). Since the surface expression of the PF, plus the SACCF and SB, pass through Drake Passage it is not surprising

that greater volumes of dense water are found in Drake Passage than in the SOFine survey region, which does not encompass those fronts. In Drake Passage, water with γ^n in the range 27.8-28.2 also displays the greatest barotropic component (with which our results agree), and the greatest temporal variability in the total transport (Cunningham et al., 2003). Rintoul and Sokolov (2001) found larger baroclinic transports of LCDW than in the present study or in the results of Cunningham et al. (2003), and less temporal variability in the baroclinic transport of denser waters than lighter, but it is unknown whether either finding is true of the total transport across SR3.

For water with $\gamma^n > 28.2$, the baroclinic transports observed by Cunningham et al. (2003) and Rintoul and Sokolov (2001) are broadly consistent with each other, though much greater than observed here since the surface PF, SACCF and SB pass the Kerguelen Plateau to the south of the SOFine survey region. The total transport of water with $\gamma^n > 28.2$ we observe (9 Sv) is well within the temporal variability of the total transport observed in Drake Passage.

An alternative way of considering the transport of AABW is to consider the transport of deep water with a potential/conservative temperature less than $0°$C, instead of water with a particular density. We do not observe any water with a conservative temperature less than $0°$C. Park et al. (2009) do not report any water with a potential temperature less than $0°$C passing through the FT. Heywood et al. (1999) report a net westward transport of water with a potential temperature less than $0°$C of ~ 17 Sv passing through the PET. While these studies were all based on different datasets and were taken at different times, collectively they suggest that there is no net eastward transport of AABW (by that definition) at these longitudes. It is only by using a density-based definition that we find net eastward transport of AABW of 2 ± 1 Sv, and that is more than offset by the westward transport through the PET reported by Heywood et al. (1999).

2.7 Vertical and Horizontal Exchange

The net transport around all three of the boxes formed by the survey is close to zero (Fig. 2.10), indicating that it was reasonable to assume zero net transport over the shallow topography between the southernmost ends of the western and central transects. The net transport of each watermass is also zero (Table 2.4) within the estimated errors, indicating that no substantial diapycnal water mass transformation takes place in this region. This is perhaps somewhat surprising as one might have expected this to be a region of high mixing given the bathymetric

slopes and close proximity of major jets. Waterman et al. (2012a) use centimeter scale shear measured by a microstructure profiler to calculate turbulent dissipation. They find that the enhancement of turbulent dissipation at depth, in association with ACC jets flowing over small-scale topography in the SOFine study region, is not as pronounced as expected from past finescale parameterization studies and lee wave radiation calculations. They suggest that this may be due in part to the modest small-scale topographic roughness in the SOFine region, but also that a non-local balance applies: the energy generated propagates away and is deposited elsewhere, possibly due to internal wave-mean flow interactions.

Bower et al. (1985) assessed the ability of the Gulf Stream to act as a 'barrier' or 'blender' to transport by contouring water properties against potential density instead of pressure. Plots of conservative temperature, absolute salinity and dissolved oxygen against neutral density (Fig. 2.13) show strong horizontal gradients across isopycnals corresponding to surface waters ($\gamma^n < 27.13$) at front locations indicating that the fronts act as barriers to transport within this density range. Deeper in the water column, for isopycnals characteristic of AAIW and UCDW ($27.13 < \gamma^n < 27.98$), the property gradients become weaker, and deeper still, for LCDW, ACCbw and AABW ($\gamma^n > 27.98$), properties are almost entirely homogeneous on isopycnals (apart from the low oxygen signature of NIDW). At first glance one might take this to mean that these water masses are well mixed across fronts, and the fronts are acting as 'blenders' deep in the water column. However, if that were the case, the low oxygen signature of NIDW would also have been mixed, and would thus be indistinguishable. Instead, the LCDW and NIDW have similar temperature and salinity characterististics because they are

Table 2.4: Cumulative transport of each water mass from station 12 to station 54.

Water mass	Total Transport (Sv)
AABW	2 ± 2
ACCbw	0 ± 4
LCDW	-7 ± 12
UCDW	1 ± 8
AAIW	1 ± 4
SW	-2 ± 4
Total	-4 ± 31

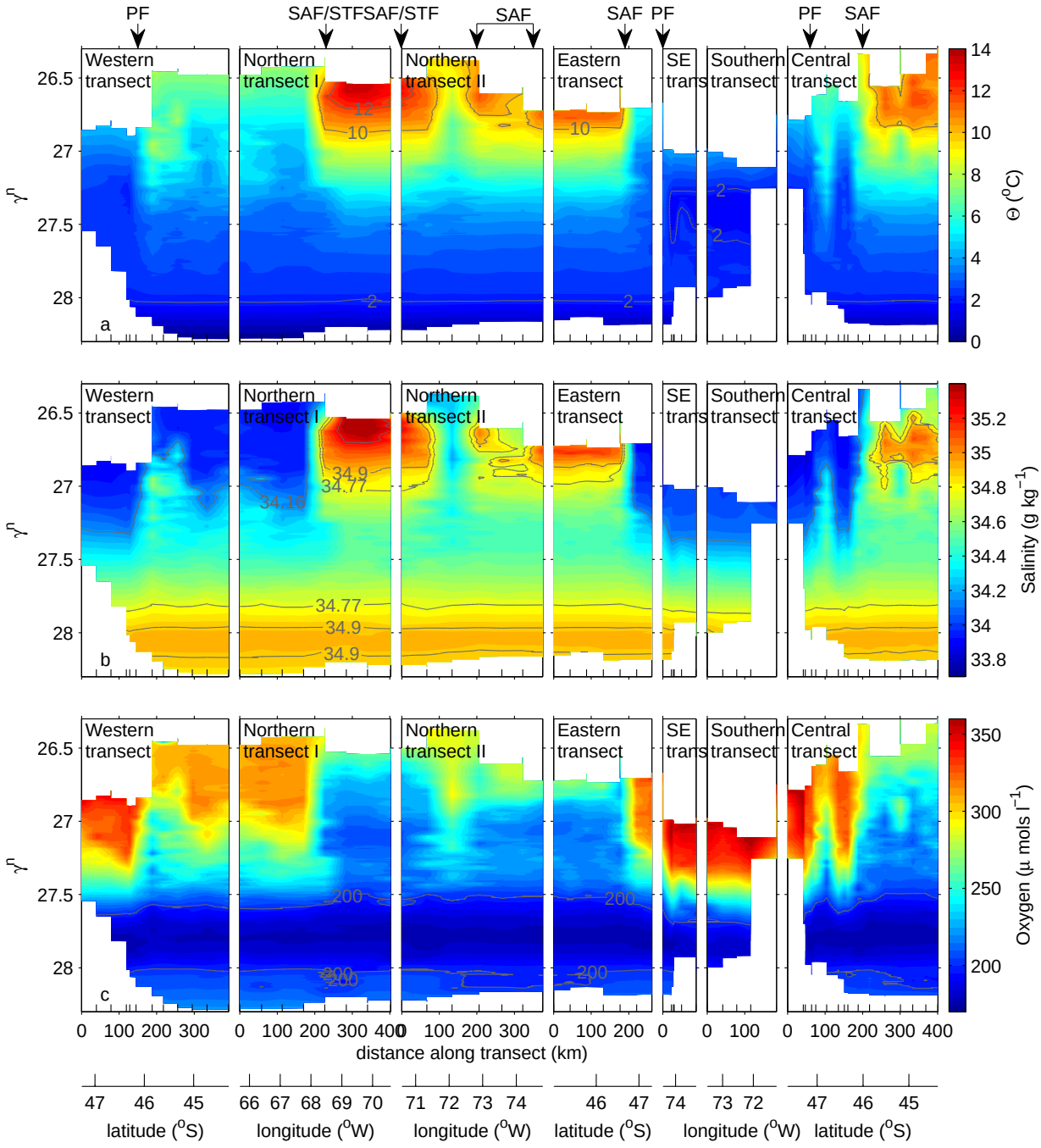

Figure 2.13: Temperature, salinity and dissolved oxygen against neutral density. In all panels, black tickmarks along the lower axis show the station locations and the fronts are identified along the upper axis [Polar Front (PF), Subantarctic Front (SAF), Subtropical Front (STF)]. (a) Conservative temperature. Grey contours show the temperatures of interest for frontal definitions (2°C, 10°C and 12°C) according to the definitions in table 2.2. (b) Absolute Salinity. Grey contours show some of the salinities of interest for frontal and water mass definitions (34.16, 34.77, 34.9 and 35.27 g kg^{-1}) according to the definitions in tables 2.2 and 2.3. (c) Dissolved oxygen. Grey contours show where the concentration is <200 μ mol L^{-1}, indicating the presence of UCDW (table 2.3).

both modified forms of NADW, but the distinct low oxygen signal indicates that the fronts are acting as barriers to transport at depth as well as for the surface waters.

2.8 Conclusions

We have presented a high resolution hydrographic survey carried out on the northern flank of the Kerguelen Plateau. We identified a complex meandering current system with a blended STF/SAF to the north, a subsurface expression of the PF to the south, and a blended SAF/PF to the east, summarized as a schematic in Fig. 2.2. An 18-year time series of surface geostrophic currents from satellite altimetry shows that the meanders and eddies observed during this survey are typical of the region, though the exact location of such features varies. The eastward baroclinic transport referenced to the deepest common level is 119 Sv, consistent with previous estimates in this region. The total eastward volume transport in the region is 174 $\pm$ 22 Sv, considerably larger than previous baroclinic estimates because of the large barotropic component of the total flow, but still broadly consistent with other estimates of transport in the Indian Ocean (Fig. 2.1). Most of this transport is associated with the blended STF/SAF. It proved difficult to estimate the transport of the subsurface PF due to the merging of the fronts and presence of eddies, but our results suggest a transport between 14 and 33 Sv. The fronts act as barriers to the exchange of water mass properties across surface waters, but may be acting as blenders deeper in the water column. Significant water mass transformation across isopycnals is not required to balance the budgets in this region. To our knowledge, we identify for the first time the presence of NIDW in the ACC on the northern flank of the Kerguelen Plateau.

This study has highlighted the complexity of the circulation in the Kerguelen region. The study presented here, as that discussed by Park et al. (1993), was a snapshot of the circulation at a particular time. One remaining question is the representativeness of such surveys in such a highly variable domain. Although altimetric currents are promising in deep water, they are currently not accurate over the continental slope and shelf. Future efforts could focus on repeat hydrographic measurements, perhaps incorporating data from autonomous vehicles such as gliders and floats.

Chapter 3

Temporal Variability of Diapycnal Mixing in Shag Rocks Passage

This chapter is published in the paper "Temporal Variability of Diapycnal Mixing in Shag Rocks Passage" in the Journal of Physical Oceanography.

citation: Damerell, G. M., K. J. Heywood, D. P. Stevens, A. C. Naveira Garabato, 2012: Temporal variability of diapycnal mixing in Shag Rocks Passage. J. Phys. Oceanogr., 42 (3), 370-385.

3.1 Abstract

Diapycnal mixing rates in the oceans have been shown to have a great deal of spatial variability, but the temporal variability has been little studied. Here we present results from a method developed to calculate diapycnal diffusivity from moored Acoustic Doppler Current Profiler (ADCP) velocity shear profiles. An 18-month time series of diffusivity is presented from data taken by a LongRanger ADCP moored at 2400 m depth, 600 m above the sea floor, in Shag Rocks Passage, a deep passage in the North Scotia Ridge (Southern Ocean). The Polar Front is constrained to pass through this passage, and the strong currents and complex topography are expected to result in enhanced mixing. The spatial distribution of diffusivity in Shag Rocks Passage deduced from lowered ADCP shear is consistent with published values for similar regions, with diffusivity possibly as large as 90×10^{-4} m^2 s^{-1} near the sea floor, decreasing to the expected background level of $\sim 0.1 \times 10^{-4}$ m^2 s^{-1} in areas away from topography. The moored ADCP profiles spanned a depth range of 2400 to 1800 m; thus the moored time series was obtained from a region

of moderately enhanced diffusivity.

The diffusivity time series has a median of 3.3×10^{-4} m^2 s^{-1} and a range of 0.5×10^{-4} m^2 s^{-1} to 57×10^{-4} m^2 s^{-1}. There is no significant signal at annual or semiannual periods, but there is evidence of signals at periods of approximately fourteen days (likely due to the spring-neaps tidal cycle), and at periods of 3.8 and 2.6 days most likely due to topographically-trapped waves propagating around the local seamount. Using the observed stratification and an axisymmetric seamount, of similar dimensions to the one west of the mooring, in a model of baroclinic topographically-trapped waves, produces periods of 3.8 and 2.6 days, in agreement with the signals observed. The diffusivity is anti-correlated with the rotary coefficient (indicating that stronger mixing occurs during times of upward energy propagation), which suggests that mixing occurs due to the breaking of internal waves generated at topography.

3.2 Introduction

Diapycnal mixing is considered to be an important component of the three-dimensional ocean circulation (Wunsch and Ferrari, 2004). A global average diapycnal diffusivity κ_z of approximately 10^{-4} m^2 s^{-1} is required to maintain the abyssal stratification (Munk and Wunsch, 1998). Measurements in the ocean interior, away from boundaries and complex topography, have typically found κ_z of order 0.1×10^{-4} m^2 s^{-1} (Toole et al., 1994; Ledwell et al., 1998; Kunze et al., 2006), whereas in areas with strong currents and complex topography diffusivities can be several orders of magnitude larger (Polzin et al., 1997; Mauritzen et al., 2002; Naveira Garabato et al., 2004; Sloyan, 2005). However, most existing measurements or estimates of diffusivity are either snapshots at a single time, or a single integrated value over months or years. The few time series available, such as those discussed by Inall et al. (2000); Rippeth et al. (2002); Palmer et al. (2008); Moum and Nash (2009); Shroyer et al. (2010) are from shallow shelf seas or tidal channels, and cover only a few days or weeks, with the longest (Moum and Nash, 2009) spanning a period of four months.

Here we present a method which could, if applied widely, begin to address the question of whether single estimates in the deep ocean can be considered representative of long term values. We derive an 18-month time series of the rate of dissipation of turbulent kinetic energy (ϵ) and κ_z, and discuss some possible mechanisms for the temporal variability seen in these series.

The Scotia Sea, an area of complex topography on the eastern side of Drake Passage (Fig. 3.1a), has been the focus of a number of studies considering mixing rates (Heywood et al., 2002; Naveira Garabato et al., 2003, 2004). Here, the Subantarctic Front and Polar Front veer northward over the ~ 2000 km long North Scotia Ridge, where the shallow (200-2000 m) topography presents an obstacle to the circumpolar flow of deep waters. The Polar Front is constrained to cross the ridge through Shag Rocks Passage, a 180 km-wide, 3200 m deep fracture zone between $49.6°$W and $47.1°$W (Moore et al., 1997; Arhan et al., 2002).

As part of the North Scotia Ridge Overflow Project (Smith et al., 2010), CTD (Conductivity-Temperature-Depth) and LADCP (Lowered Acoustic Doppler Current Profiler) profiles were collected between 23 April and 5 May 2003 along the length of the North Scotia Ridge (Fig. 3.1). Six moorings were placed in Shag Rocks Passage between April 2003 and November 2004 (Walkden et al., 2008), one of which (mooring Shag 2b, water depth 3000 m) included an upward-looking LongRanger ADCP 600 m above bottom (mab) (Table 3.1 and Fig. 3.1). The

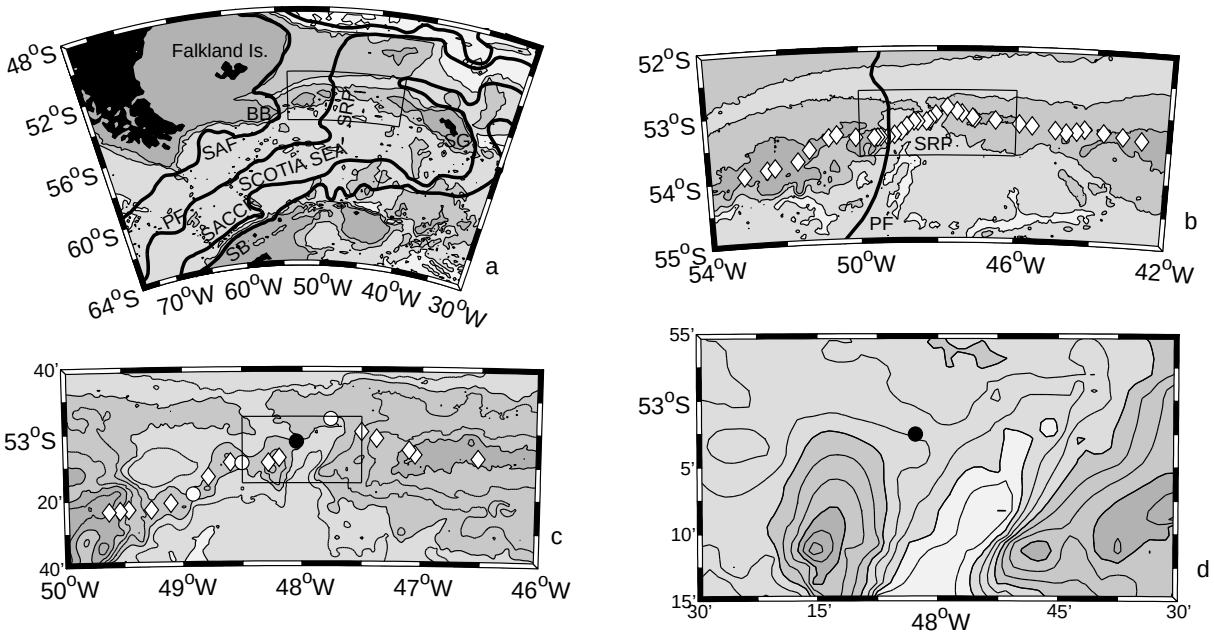

Figure 3.1: Regional map, with bathymetry from Smith and Sandwell (1997), and climatological trajectories of the ACC fronts from Orsi et al. (1995). (SAF = Subantarctic Front, PF = Polar Front, SACCF = Southern ACC Front, SB = Southern Boundary of the ACC.) Contour intervals are every 1500m in (a) and (b). The following topographic features are indicated by their initials: Burdwood Bank (BB), South Georgia (SG), Shag Rocks Passage (SRP). (a) Overview of the Scotia Sea. (b) North Scotia Ridge, with deployment cruise station locations indicated by diamonds. (c) Overview of Shag Rocks Passage. Contour intervals are now every 500m with shading every 1500m. The circles are the mooring locations, at which CTDs were deployed during both the deployment and recovery cruises; other deployment cruise station locations are indicated by diamonds. From west to east, the moorings are Shag1a, Shag1b, Shag2(a and b) and Shag3(a and b). This study is concerned primarily with mooring Shag2b, which is the black circle. (d) Shag Rocks Passage. Contour intervals are now every 200m with shading every 600m. The black circle is mooring Shag2b. Note the seamount of height $\sim$ 1600 m southeast of the mooring location. In (a), (b) and (c), the thin black rectangle indicates the area shown in the next panel.

ADCP recorded velocity in 40 bins with a thickness of 16 m, thus observing a total depth of 640 m.

We calculate an 18-month κ_z time series using the method previously used in the Scotia Sea by Naveira Garabato et al. (2004), (originally developed by Gregg and Kunze, 1991, with further modifications following Polzin et al., 2002 and Gregg et al., 2003), wherein κ_z can be estimated from profiles of temperature, salinity and current velocity. This relies on the premise that the nonlinear interactions of internal waves initiate an energy cascade to smaller scales, resulting in turbulent dissipation (McComas and Muller, 1981; Henyey et al., 1986) from which κ_z can be inferred

Table 3.1: Instruments moored in Shag Rocks Passage from 06/05/03 - 27/11/04. mab = metres above bottom.

Mooring	Latitude	Longitude	Water Depth (m)	Instrument Type	mab	Sampling Interval
Shag 1a	53°18.251′S	48°54.828′W	2960	Aanderaa RCM8	30	hourly
Shag 1b	53°09.018′S	48°29.948′W	2766	Aanderaa RCM8	400	hourly
				RDI 300 kHz Workhorse ADCP	600	20 mins
				Pressure/Temp. logger XR420 TD	600	3 mins
Shag 2a	53°02.510′S	48°02.313′W	2996	Aanderaa RCM8	30	hourly
				Aanderaa RCM8	100	hourly
Shag 2b	53°02.510′S	48°02.770′W	2999	Aanderaa RCM8	400	hourly
				RDI 75 kHz LongRanger ADCP	600	2-hourly
				Pressure/Temp. logger SBE 39	600	10 mins
Shag 3a	52°55.653′S	47°45.992′W	2928	Aanderaa RCM8	30	hourly
				Aanderaa RCM8	100	hourly
Shag 3b	52°55.670′S	47°45.550′W	2945	Aanderaa RCM8	400	hourly
				RDI 300 kHz Workhorse ADCP	600	20 mins

(Osborn, 1980). This method can therefore only assess mixing due to internal wave breaking (and not that due to other non-internal wave processes). This is a valid assumption for this region, as the instruments are not in a region where waters are cascading over a sill, are 600 m off the sea floor so should be away from bottom boundary layers which might be dominated by bottom friction, and are observing water deep enough ($>$1800 m) that direct wind-driven mixing, such as occurs in the surface mixed layer, is unlikely to occur.

Possible mechanisms for internal wave generation include:

i Wind forcing can generate near-inertial motions, and, although the large inertial oscillations seen in near-surface waters decrease in amplitude rapidly with depth below the mixed layer (Pollard, 1970; Pollard and Millard, 1970), they do penetrate somewhat into the ocean interior as internal waves (D'Asaro, 1984; Alford, 2001, 2003a,b). These could then interact further with the local topography, much of which, along the North Scotia Ridge, is only a few hundred meters deep.

ii In stratified waters, the interaction of barotropic tidal currents with variable

bottom topography can result in the generation of internal tides (Heywood et al., 2007). As discussed by Garrett and St Laurent (2002); St Laurent and Garrett (2002); Garrett and Kunze (2007), most of the energy flux is associated with low modes that propagate away from the generation region, but intense beams of internal tidal energy are generated by certain 'critical' slopes, and lead to local mixing.

iii In principle, any movement of water over rough topography may generate internal waves (Bell, 1975; Baines, 1982), which can then initiate an energy cascade to smaller scales and cause turbulent dissipation (McComas and Muller, 1981; Henyey et al., 1986). As well as internal tides, this can be through the generation of lee waves by geostrophic flows (Nikurashin and Ferrari, 2010a,b), particularly in the Southern Ocean where bottom geostrophic flows are much more intense than in most other ocean basins. The complex topography in Shag Rocks Passage (Fig. 3.1d) includes many features at which lee waves could be generated.

iv The mean flow can also interact with the internal wave field. For example, Kunze and Sanford (1984) and Kunze (1985) observed intense, focussed beams of downward-propagating near-inertial waves at the base of regions of upper ocean negative vorticity. They determined that a wave-mean flow interaction model which predicts trapping and amplification of near-inertial waves in regions of negative vorticity best explained their observations.

The generation from, and interaction with, geostrophic flows may also lead to another indirect link between internal waves and wind forcing, as increased wind speeds can lead to intensified currents, or result in increased eddy activity which transmits momentum downwards through the water column (Bryden, 1979; Olbers, 1998).

The organisation of this chapter is as follows: section 3.3 begins with a description of the method and uses this to produce a section of κ_z along the North Scotia Ridge, thus setting the spatial context for the moored time series. Section 3.4 discusses the modifications to the method for use with mooring data and the time series thus obtained. In section 3.5, spectral analysis is used to identify significant periodicities, and potential sources of temporal variability in κ_z are identified. Section 3.6 presents the conclusions.

3.3 Spatial Variability of Diffusivity in Shag Rocks Passage

First, we recap the methodology used by several authors (e.g., Polzin et al., 1995, 2002; Naveira Garabato et al., 2004; Kunze et al., 2006) to estimate ϵ and κ_z from LADCP data. Estimates of κ_z are inferred from velocity shear estimates using a model that assumes a statistical balance between turbulent production, buoyancy flux, and dissipation (Osborn, 1980). In common with previous LADCP analyses, we assume that subinertial shear is small compared with that in the internal wave field. The dissipation rate and diapycnal diffusivity are related by $\kappa_z = \Gamma\epsilon/N^2$ where Γ is the mixing efficiency (generally assumed to be 0.2) and N is the buoyancy frequency. The turbulent dissipation rate can be found from:

$$\epsilon = \epsilon_0 \times \frac{f}{f_0}\frac{N^2}{N_0^2}\frac{\cosh^{-1}(N/f)}{\cosh^{-1}(N_0/f_0)}\frac{\langle V_z^2\rangle^2}{\left\langle V_{z-GM}^2\right\rangle^2}\, h_1(R_\omega) \tag{3}$$

(Gregg and Kunze, 1991; Polzin et al., 1995, 2002; Gregg et al., 2003). Here $\epsilon_0 = 7.8\times10^{-10}$ W kg^{-1} is the turbulent dissipation rate of the background internal wave field in stratification defined by a buoyancy frequency $N_0 = 5.24\times10^{-3}$ rad s^{-1} at a latitude of $30°$, as predicted for the Garrett and Munk (GM) model (Garrett and Munk, 1975). f and f_0 are the inertial frequencies at the latitude of observation and at $30°$ respectively ($f_0 = 7.3\times10^{-5}$ s^{-1} and $f = 1.2\times10^{-4}$ s^{-1}). The latitudinal dependence of the energy cascade to smaller scales is discussed by Gregg et al. (2003). $\langle V_z^2\rangle$ is the variance of the LADCP vertical shear, normalised by N, and $\left\langle V_{z-GM}^2\right\rangle$ is the same variable, as predicted by the GM model. $h_1(R_\omega)$ is a function of the frequency content of the internal wave field (Polzin et al., 1995) estimated from the shear-to-strain ratio R_ω, discussed below.

To derive $\langle V_z^2\rangle$, each LADCP shear profile is divided into overlapping 320 m segments spaced at 100 m intervals, and normalized by the average buoyancy frequency $\overline{N}$ for that segment. The normalised shear in each segment is Fourier-transformed (64 points) to compute the vertical wavenumber power spectral density. This spectrum is corrected to account for the smoothing in the velocity profiles at high vertical wavenumbers, caused by the spatial averaging inherent in LADCP measurement and data processing (Polzin et al., 2002). Specifically, the corrections described by Polzin et al. (2002) for the finite acoustic transmission and reception intervals, first-differencing of the resulting single-ping velocity profiles, interpolation of the first-differenced profiles onto a regular depth grid,

and instrument tilt are applied. $\langle V_z^2 \rangle$ is calculated by integrating the corrected power spectral density between the maximum vertical wavelength of 300 m and a minimum vertical wavelength of 90 m, chosen to minimize the contamination by instrument noise that can occur at higher wavenumbers. This minimum vertical wavelength threshold is selected heuristically by examination of the shear spectra, and the resulting ϵ and κ_z are insensitive to the exact value. $\left\langle V_{z-GM}^2 \right\rangle$ is integrated over the same wavelength range as $\langle V_z^2 \rangle$.

The shear/strain variance ratio R_ω is a measure of the internal wave field's frequency content (Kunze et al., 1990) and is used to parameterize the turbulent dissipation rate in equation (3). R_ω is found from

$$R_\omega = \frac{\langle V_z^2 \rangle}{\langle \xi_z^2 \rangle} = 3 \times \frac{\langle V_z^2 \rangle}{\left\langle V_{z-GM}^2 \right\rangle} \frac{\left\langle \xi_{z-GM}^2 \right\rangle}{\langle \xi_z^2 \rangle}. \tag{4}$$

$\langle \xi_z^2 \rangle$ is the variance of strain, the vertical gradient of the vertical displacement of isopycnals induced by internal waves. $\left\langle \xi_{z-GM}^2 \right\rangle$ is the same variable, as predicted by the GM model, and integrated over the same wavelength range as $\langle \xi_z^2 \rangle$. The factor of three arises because $\left\langle V_{z-GM}^2 \right\rangle / \left\langle \xi_{z-GM}^2 \right\rangle = 3$. Strain is estimated from CTD density profiles using a scale separation assumption (Polzin et al., 1995) and $\langle \xi_z^2 \rangle$ (and R_ω) are calculated in 320 m segments identical to the $\langle V_z^2 \rangle$ bins. R_ω is then averaged horizontally over all stations to give a profile which varies with depth, but does not vary from station to station. $h_1(R_\omega)$ is calculated (Polzin et al., 1995) for each depth as

$$h_1 = \frac{3(R_\omega + 1)}{2\sqrt{2} R_\omega \sqrt{R_\omega - 1}}. \tag{5}$$

The average of R_ω throughout Shag Rocks Passage is 6.0, corresponding to $h_1(R_\omega) = 0.56$. At the depths observed by the mooring, the average R_ω is 7.6, giving $h_1(R_\omega) = 0.47$, and it is this value which is used to parameterize diffusivities calculated from the mooring data, as discussed below.

The κ_z section across Shag Rocks Passage produced from the CTD/LADCP profiles (Fig. 3.2) shows greatly enhanced κ_z at depth and over complex topography ($\sim 90 \times 10^{-4}$ m^2 s^{-1}), decreasing to a background level of $< 0.1 \times 10^{-4}$ m^2 s^{-1} (consistent with the findings of Toole et al., 1994; Ledwell et al., 1998; Kunze et al., 2006) in areas well away from the sea floor, and at depths of no more than 1000 m. Similarly ϵ varies between $\sim (0.02 - 23) \times 10^{-9}$ W kg^{-1}, and has a comparable spatial pattern (not shown). Both κ_z and ϵ are smoothed horizontally using a 5-station running mean. This section is comparable to published sections elsewhere, particularly those in and around the Scotia Sea (Naveira Garabato et al.,

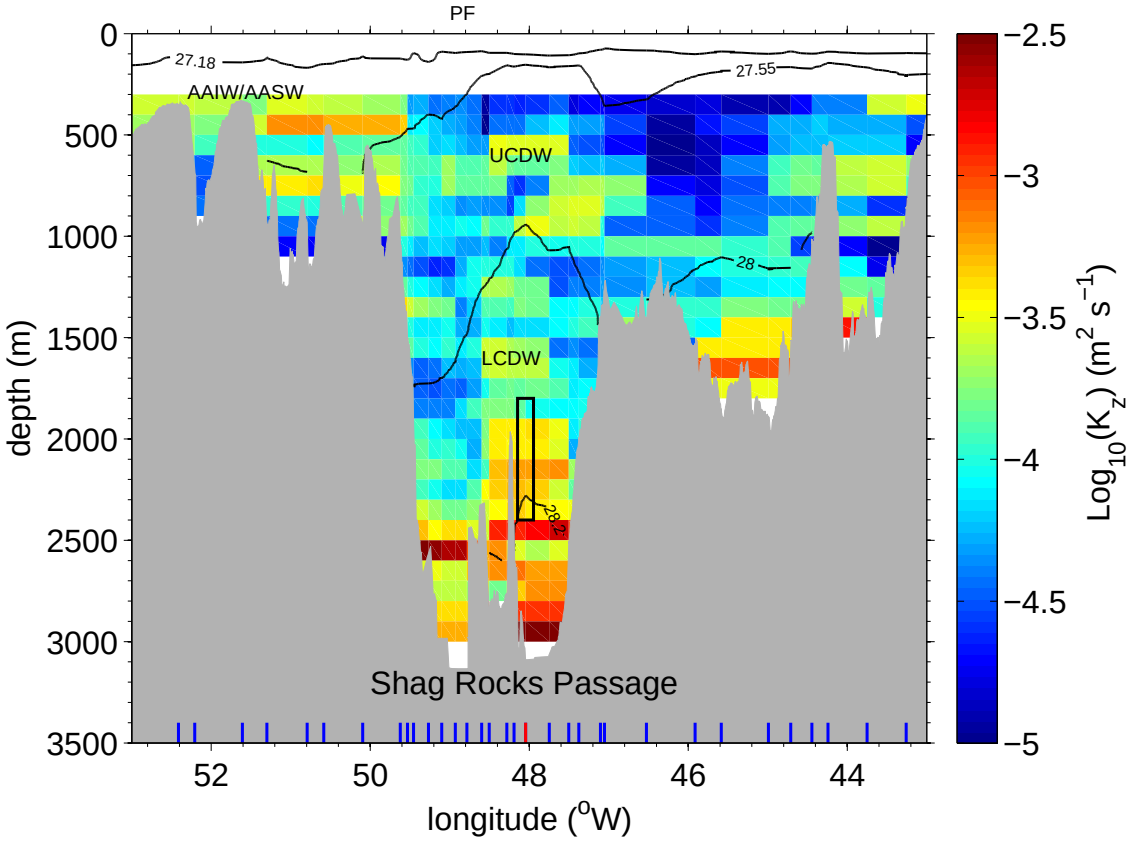

Figure 3.2: Vertical diffusivity (κ_z) along the North Scotia Ridge. Density surfaces, shown as black lines, separate different water masses (AAIW/AASW, Antarctic Intermediate Water/Antarctic Surface Water, $27.18 < \gamma^n < 27.55$; UCDW, Upper Circumpolar Deep Water, $27.55 < \gamma^n < 28.00$; LCDW, Lower Circumpolar Deep Water, $28.00 < \gamma^n < 28.20$, where γ^n is the neutral density, in kg m^{-3}, as defined by Jackett and McDougall, 1997). Station positions are indicated by blue tickmarks at the base of the topography, with the mooring position as a red tickmark. The approximate location of the Polar Front is marked as PF on the upper axis. The black rectangle in Shag Rocks Passage gives an approximate indication of the extent of the LongRanger ADCP at mooring Shag 2b; the horizontal extent of the rectangle is for illustrative purposes only.

2004; Sloyan, 2005). Sloyan's meridional section across the Scotia Sea (her Fig. 3a) is calculated using CTD strain variance techniques, and shows $\kappa_z \sim (10 - 100) \times 10^{-4}$ m^2 s^{-1} near the sea floor, decreasing to $\sim 0.1 \times 10^{-4}$ m^2 s^{-1} or less away from rough topography, consistent with what is observed here.

The section of Naveira Garabato et al. (2004) shows $\kappa_z \sim 100 \times 10^{-4}$ m^2 s^{-1} near the sea floor, with a maximum of nearly 1000×10^{-4} m^2 s^{-1} at the sea floor of Drake Passage and in a deep gap (Orkney Passage) in the South Scotia Ridge (their Fig. 2). Fairly low values of $\sim (0.4 - 4) \times 10^{-4}$ m^2 s^{-1} were observed over the Falkland Plateau, geographically the closest region to the North Scotia

Ridge. The much smoother topography of the Falkland Plateau compared with Shag Rocks Passage explains these lower values. The most similar region, in terms of roughness and depth of topography, is the South Scotia Ridge, which shows correspondingly similar results, including enhanced mixing over shallow (< 1500 m depth) topography to the west of the South Orkney Islands, analogous to that seen in Fig. 3.2 to the west of Shag Rocks Passage. The considerably greater κ_z found by Naveira Garabato et al. in Orkney Passage (nearly 1000×10^{-4} m^2 s^{-1}) than seen anywhere in Shag Rocks Passage may be due to the stronger currents at the sea bed there (velocities approaching 50 cm s^{-1} (Naveira Garabato et al., 2002) as opposed to ~ 20 cm s^{-1} in Shag Rocks Passage). Naveira Garabato et al. (2004) found a sharp reduction in κ_z to values only slightly above 0.1×10^{-4} m^2 s^{-1} in the uppermost 300-400 m of their section in Drake Passage, Orkney Passage and the Scotia Sea. A similar pattern is seen in Fig. 3.2 between approximately $44 - 49°$W. This region has comparable depths and roughness to the Drake Passage, Orkney Passage and Scotia Sea sections of Naveira Garabato et al. (2004), which have comparable κ_z patterns.

Kunze et al. (2006) raised doubts about the applicability of the shear parameterization in very low abyssal stratifications (their Fig. 3). They argue that noise in LADCP measurements prevents measurement of the shear in areas with $N < 4.5 \times 10^{-4}$ rad s^{-1}, casting doubt on the very high diffusivities at the sea floor of Naveira Garabato et al. (2004). Polzin and Lvov (in press) argue that what has previously been considered noise may in fact be a slow mode consisting of, at lowest order, the steady geostrophic balance. Higher order contributions are time dependence, nonlinearity and the effects of a variable rate of planetary rotation (f). In the section presented here, $N > 4.5 \times 10^{-4}$ rad s^{-1}, except in a very small area below 2700 m, east of the central seamount in Shag Rocks Passage. Moreover, we obtain similar values (not shown) from a strain-only calculation of κ_z independent of the LADCP shear, as used by Mauritzen et al. (2002) and Sloyan (2005). This strain-based calculation of κ_z gives a range of $\sim (0.05 - 100) \times 10^{-4}$ m^2 s^{-1} and a similar spatial pattern to κ_z calculated using LADCP shear. The shear parameterization should therefore be applicable to the moored ADCP time series.

The rotary coefficient of the vertical shear is the ratio of the clockwise and counter-clockwise components of the shear variance, and is a proxy for the ratio of upward to downward energy propagation. It is calculated following Gonella (1972) for the stations in Shag Rocks Passage deeper than 2000 m and lying to the east of the central seamount (Fig. 3.3). Above ~ 1500 m the propagation is mostly downward, and most likely wind-driven (Alford, 2003a). Below ~ 1500

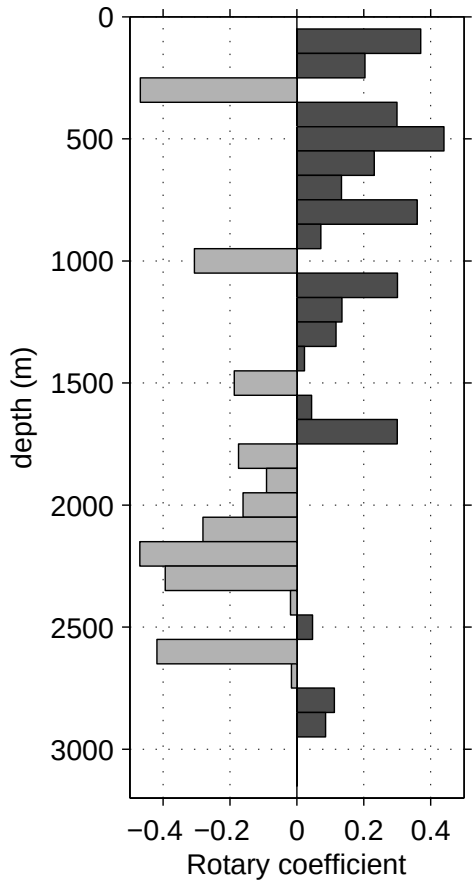

Figure 3.3: Rotary coefficient (dimensionless) for the stations in Shag Rocks Passage deeper than 2000 m. Values less than zero indicate upward propagation of energy, values greater than zero indicate downward propagation.

m the propagation is mostly upward, likely due to internal waves generated at the topography (Baines, 1973, 1982; Thorpe, 1992).

3.4 Temporal Variability of Diffusivity in Shag Rocks Passage

3.4.1 Methodology

The ADCP at mooring Shag2b produced time series of velocity profiles at 2-hour intervals. The method adopted here to calculate κ_z for the time series is essentially the same as described in Section 2 for the LADCP data, repeated for each time interval. There are some modifications to the calculations.

i Depth Segment and Fourier transform

The shears are treated as one 640 m segment centered at 2100 m depth. After quality control (which consisted of the rejection of points where less than 50% of the measurements had four-beam solutions), generally around 400-500 m remained for use in the Fourier transform, and occasionally as little as 300 m. κ_z is insensitive to the chosen percentage for quality control; using either 25% or 75% as the rejection threshold makes a difference of around 4% to the calculated values, which is small compared with other uncertainties. Since the calculation requires depth bins of at least 320 m of good data, the data were not divided into depth segments in order to retain enough information to calculate the spectral densities. The ADCPs on moorings Shag1b and Shag3b (Table 3.1 and Fig. 3.1) recorded velocities in 23 bins of 8 m thickness. After quality control, insufficient depth range remained to resolve wavelengths of 90 m or more, so these could not be used to calculate κ_z.

Each velocity measurement of the ADCP on mooring Shag2b is based on 31 pings, corresponding to an accuracy of approximately 0.6 cm s^{-1}. The LADCP measurements are based on an average of $\sim$120 pings, giving an accuracy of approximately 0.3 cm s^{-1}. In the stratification observed here (N typically $\sim 8 - 9 \times 10^{-4}$ s^{-1} in the CTD stations at the depths ensonified by the moored ADCP), typical internal wave speeds are $\sim 1 - 5$ cm s^{-1} (Thorpe, 2005), considerably greater than the accuracy of either instrument.

ii Buoyancy Frequency

Time series of temperature and salinity were not measured in the volume of water above the mooring in which the currents are sampled by the ADCP. However, a SeaBird Electronics temperature sensor (SBE-39) was mounted on the ADCP, which has a comparable accuracy (± 0.002°C) to the ship's CTD (SBE-3*plus*, accuracy ± 0.001°C). Each rotary current meter (Table 3.1) recorded temperature with an accuracy of ± 0.05°C. All moored temperature sensors agreed with CTD casts at the beginning and end of the mooring deployment. Here we discuss how best to use these time series to provide time series of temperature and salinity (and hence buoyancy frequency) appropriate to the water column monitored by the ADCP.

13 full depth CTD stations were occupied in Shag Rocks Passage during the deployment cruise, and four during the recovery cruise, that can be used to infer relationships between temperatures at different depths (Fig. 3.4). The four temperature time series from mooring Shag2(a and b) are linearly related,

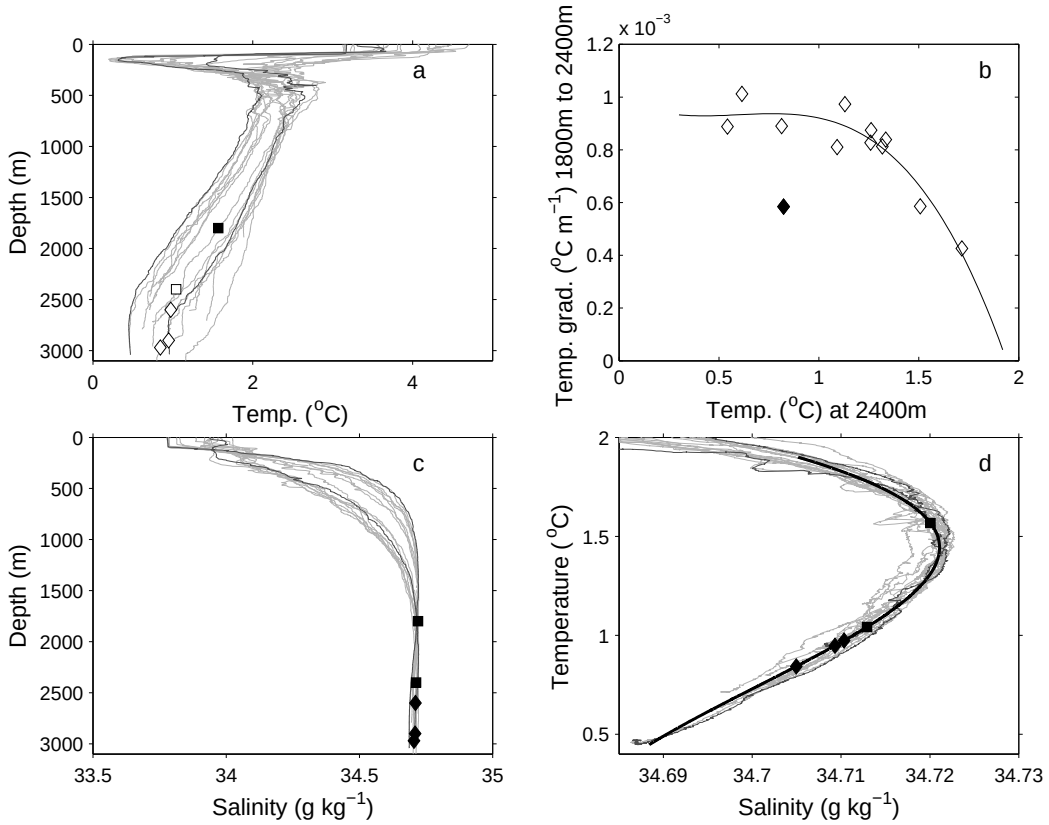

Figure 3.4: The extrapolation of temperature and fitting for salinity used to derive the timeseries of buoyancy frequency. In (a), (c) and (d), the grey lines are profiles of the Shag Rocks Passage CTD stations, with the darker grey being the closest station of each cruise. (a) Temperature against depth. The white diamonds are the mean temperatures recorded by the three RCMs, 30, 100 and 400 meters above bottom (mab), the white square is the mean temperature recorded by the sensor on the ADCP 600 mab, and the black square is the mean extrapolated temperature at 1200 mab. (b) Relationship between the temperature at 2400 m and the temperature gradient between 1800 and 2400 m, i.e., the depth range observed by the moored ADCP. The black line is the cubic fit used to extrapolate temperatures above 2400m during the mooring time series. The black diamond is station 58 of the deployment cruise, which was excluded as an outlier. (c) Salinity against depth. The black diamonds and squares are the mean fitted salinities at 30, 100, 400, 600 and 1200 mab. (d) T–S relationship. The black line represents the cubic fit used to calculate salinity from temperature, and the black diamonds and squares represent the mean T–S values at 30, 100, 400, 600 and 1200 mab.

as are the CTD temperatures at the same depths as the moored temperature sensors. Therefore we fitted the CTD temperature gradient between 1800 and 2400 m, (the depth range observed by the moored ADCP), to the temperature at 2400 m. Fig. 3.4(b) illustrates the cubic fit which was found to best reproduce the observed temperature profile. The CTD temperature profiles (Fig. 3.4a) fall into two groups: a warmer group and a colder group, which lie north and south of the Polar Front respectively. Stations with a higher

temperature at 2400 m have a lower temperature gradient, and vice versa (Fig. 3.4b). The spread in temperatures is thus less at 1800 m depth than at 2400 m. The cubic fit to the CTD stations was used, in conjunction with the temperature at 2400 m recorded by the ADCP, to generate temperature gradients, and thus temperatures, between 1800 and 2400 m for the entire time series.

Similarly, a cubic fit to the CTD T - S relationship (in-situ temperature and salinity respectively) is used to infer salinities between 1800 - 2400 m (Fig. 3.4). From the temperatures and salinities a time series of buoyancy frequency is deduced. The parameter that has the greatest impact on the calculated κ_z is the temperature gradient, which varies by more than a factor of ten during the time series. As is apparent in Fig. 3.4(d), salinity varies by no more than 0.009 g kg^{-1} in the ADCP ensonified volume; the effect of salinity on the variability of κ_z is very small.

iii Spectral Corrections

The corrections described by Polzin et al. (2002) for the finite acoustic transmission and reception intervals, and first-differencing of the resulting single-ping velocity profiles, are applied exactly as for the LADCP shear spectra. We do not need to apply the correction for interpolation of the first-differenced profiles onto a regular depth grid as no interpolation is performed for a moored instrument.

iv Smoothing

The finescale parameterization used here assumes a stationary internal wavefield, and the stationarity assumption is more likely to hold over a time scale $> 1/f$ (15 hours) than over 2 hours. In a manner similar to the horizontal smoothing of κ_z and ϵ for the spatial section using a 5-station running mean, here we calculate a running mean over 24 hours for κ_z and ϵ. (The length of the running mean was chosen as a compromise between maintaining temporal resolution and the desire to justify the stationarity assumption.) All values quoted from now, or shown in figures or tables, will be those found after applying the running mean unless stated otherwise.

v Shear-to-strain ratio parameterization

Since we do not have time series of temperature and salinity in the water mass ensonified by the ADCP, we cannot estimate $\langle \xi_z^2 \rangle$ as described in Section 2, and thus cannot calculate a time series for R_ω. Instead, we use the average

value of R_ω from the LADCP section over the ensonified depths, which gives $h_1(R_\omega) = 0.47$.

Some examples of the vertical wavenumber spectra of the shear are shown in Fig. 3.5, and are comparable to those in the literature (e.g., Fig. 2 of Kunze et al., 2006). Fig. 3.5 also shows the vertical wavenumber spectrum for shear noise: rms noise levels are about $(3.2\,\mathrm{cm\,s^{-1}})/\mathrm{nping}^{1/2}$ for a large number of scatterers (Polzin et al., 2002), where nping is the number of pings used for each velocity measurement. Over the interval of integration (90 - 300 m), the spectra are relatively flat, and are clearly distinguishable from the noise spectrum. At higher wavenumbers (wavelengths $<$90 m) the spectra are dominated by noise, which illustrates the validity of the choice of 90 m as the minimum wavelength over which the spectra are integrated.

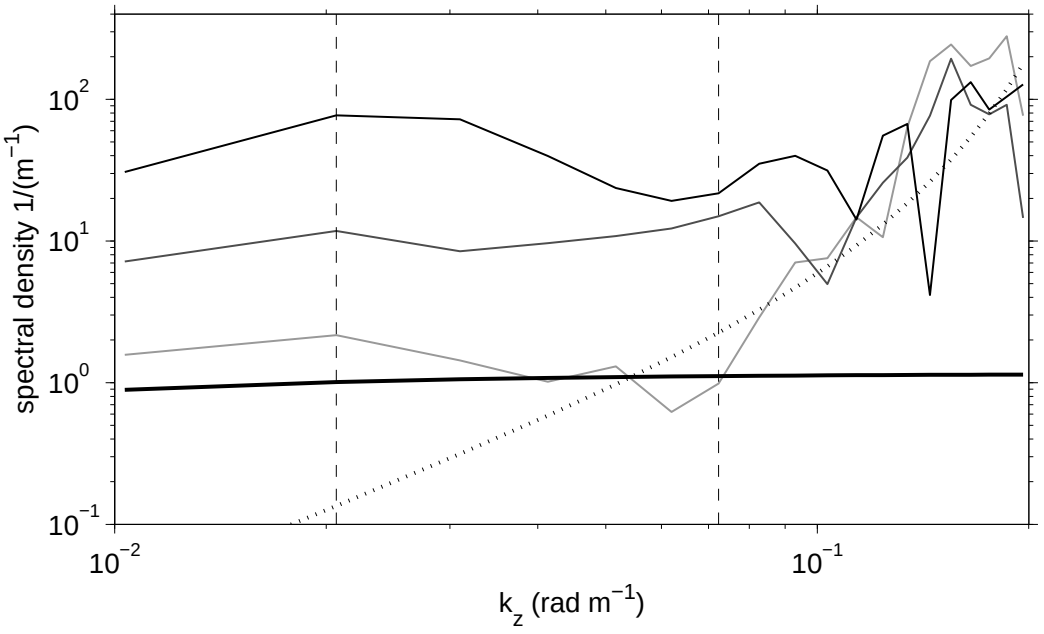

Figure 3.5: Some example vertical wavenumber spectra. The thin solid lines are the spectra for the times when the calculated diffusivity was the minimum (pale grey), median (darker grey), and maximum (black) value of the time series. The thick solid black line is the GM model spectrum, the dotted line is the spectrum for shear noise of velocity variance $(3.2\,\mathrm{cm\,s^{-1}})^2/\mathrm{nping}$, where nping is the number of pings used for each velocity measurement. The vertical dashed lines are the limits of integration, corresponding to wavelengths of 300 m and 90 m.

3.4.2 Resultant Time Series

Fig. 3.6 shows the time series of ADCP velocity, integrated shear variance, temperatures, depth-average buoyancy frequency $\overline{N}$, rotary coefficient and the derived κ_z. The integrated shear variance is $\langle V_z^2 \rangle$ without the normalization by $\overline{N}$, so as to show the shear and buoyancy frequency separately. Included for comparison is the 6-hourly wind speed from the ECMWF reanalysis dataset ERA-Interim, (ECMWF, cited 2009), at the nearest grid point ($48°$W, $52.5°$S) to mooring Shag2b. All the mooring time series show good agreement with the values obtained from the closest CTD/LADCP stations of the deployment and recovery cruises. The time series of ϵ is not shown, as it is so strongly correlated with κ_z ($r = 0.98$) that it does not provide additional information.

κ_z has a mean of 4.1×10^{-4} m^2 s^{-1}, median of 3.3×10^{-4} m^2 s^{-1} and covers a range from 0.5×10^{-4} to 57×10^{-4} m^2 s^{-1}. At the depths ensonified by the moored ADCP, the spatial section (Fig. 3.2) has κ_z varying from 0.3×10^{-4} to 20×10^{-4} m^2 s^{-1}, with a mean of 3.1×10^{-4} m^2 s^{-1}. The range in the spatial section across Shag Rocks Passage is consistent with the range of the time series, especially given the inherent uncertainty in the method (reported by Polzin et al. (2002) to be around a factor of 3-4).

None of the time series (Fig. 3.6) display annual or semi-annual signals, such as those seen by Large and Van Loon (1989) in Southern Ocean winds. There is no significant correlation between the local wind speed and any of the mooring records (Fig. 3.6), or the velocity and temperature of the other moorings in Shag Rocks Passage (Table 3.1 and Fig. 3.1). The possible influence of the winds or atmospheric pressure (direct or indirect) was further investigated by searching for correlations between κ_z and the wind speed and atmospheric pressure at sea level, bandpass filtered to near-inertial periods, using the ERA-Interim dataset, (ECMWF, cited 2009) in the entire region south of $30°$S. Lags of up to 80 days were considered. No significant correlations were found.

Table 3.2 lists statistics of the time series of integrated shear variance, buoyancy frequency, dissipation rate, rotary coefficient and diffusivity. The agreement is good between the first values of the time series and the LADCP values taken from the nearest station of the deployment cruise and averaged over the same depths observed by the moored ADCP. This station was occupied approximately 7 hours before the start of the mooring record. All (except the rotary coefficient) have rather non-normal distributions, as indicated by their large skewness and excess kurtosis, although the integrated shear variance and buoyancy frequency are much

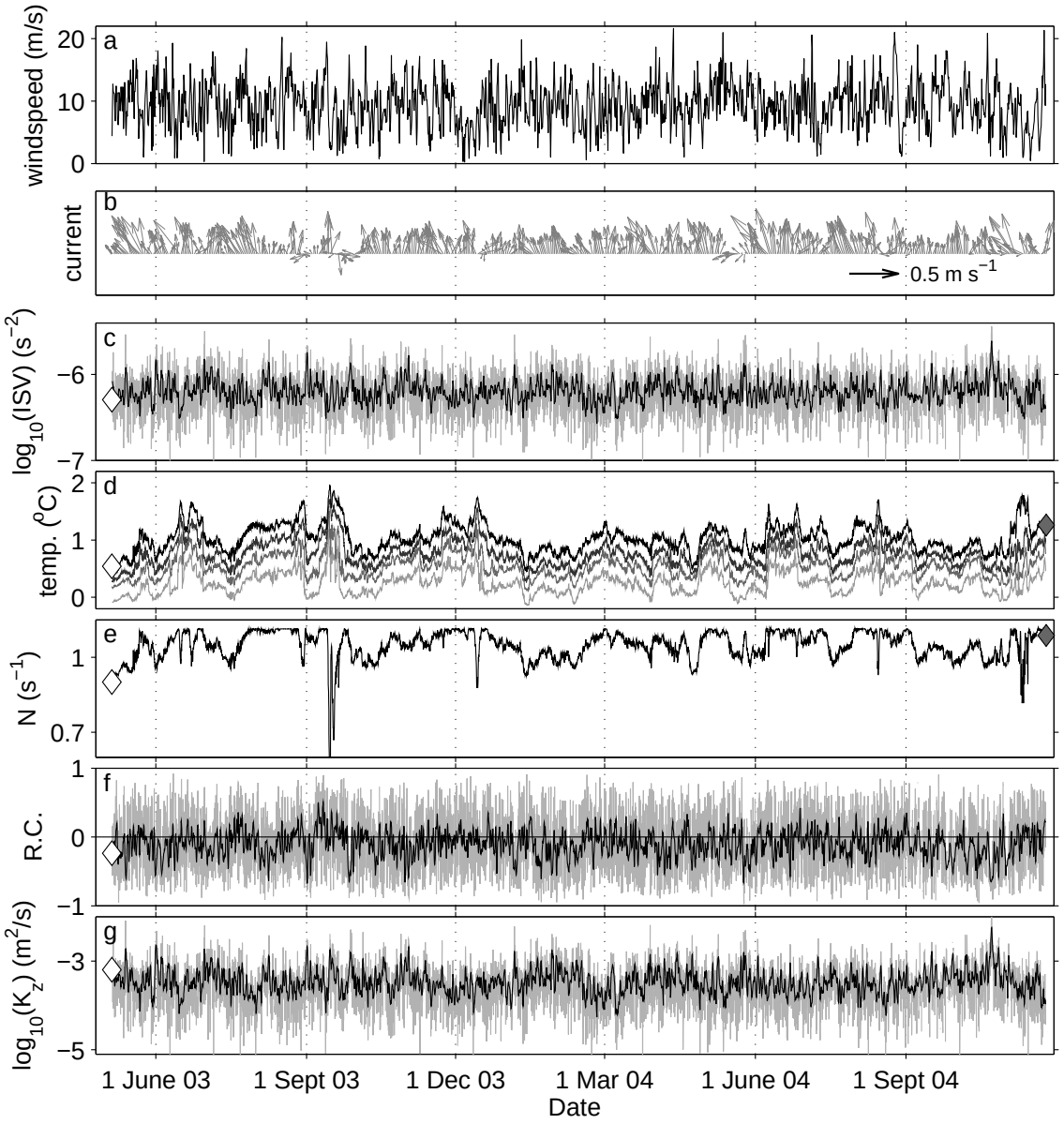

Figure 3.6: Time series at the moored array in Shag Rocks Passage. (a) ECMWF reanalysis wind speed from the closest grid point. (b) Depth-averaged daily currents recorded by the moored ADCP. The first arrow at the start of the time series is that recorded by the LADCP on the closest station of the deployment cruise (station 56). (c) Log_{10}(integrated shear variance) (s^{-2}). (d) Temperatures ($^\circ$C). The palest line is the temperature recorded 30 mab, offset by -0.6°C, the mid-grey line is that recorded 100 mab, offset by -0.4°C, the darkest grey line is that recorded 400 mab, offset by -0.2°C, and the black line is that recorded 600 mab. The white diamond is that recorded by the CTD at station 56, and the grey diamond is that recorded by the CTD on the closest station of the recovery cruise (station 19), both at 2400 m. (e) Buoyancy frequency ($\times 10^{-3}$ s^{-1}). The grey diamond is that recorded at station 19 of the recovery cruise, averaged over the depths observed by the moored ADCP. (f) Rotary coefficient (dimensionless). (g) $\mathrm{Log}_{10}(\kappa_z)$ (m^2 s^{-1}). The horizontal line is the median value. For subplots (c),(e),(f) and (g), the grey line is the unsmoothed quantities, the black line is daily average values, and the white diamond is that recorded at station 56 of the deployment cruise, averaged over the depths observed by the moored ADCP.

less extreme than ϵ and κ_z. Higher kurtosis indicates that more of the variance is the result of infrequent extreme deviations, as opposed to frequent modestly sized deviations. Averaging over periods of 5 days or more gives a significantly more stable mean. The distribution of κ_z is shown in Fig. 3.7, and is log-normal, consistent with microstructure turbulence observations (e.g., Gregg et al. 1993).

Table 3.2: Various statistics of the time series of integrated shear variance (ISV), buoyancy frequency ($\overline{N}$), dissipation rate (ϵ), diffusivity (κ_z) and rotary coefficient (R.C.), with the equivalent values as found by the LADCP, taken from the nearest station of the deployment cruise and averaged over the same depths observed by the moored ADCP. (st. dev. = standard deviation, %ile = percentile. All values given to 2 s.f., except for the buoyancy frequency which is given to 2 d.p. in order to distinguish the median, 75th percentile, maximum and mean. All time series values are after applying the running 24-hour mean. The skewness and excess kurtosis are not scaled by the factors given in the column headings, and are both dimensionless numbers.)

	ISV ($\times 10^{-7}\,\mathrm{s}^{-2}$)	$\overline{N}$ ($\times 10^{-3}\,\mathrm{s}^{-1}$)	ϵ ($\times 10^{-9}\,\mathrm{W\,kg}^{-1}$)	κ_z ($\times 10^{-4}\,\mathrm{m}^2\,\mathrm{s}^{-1}$)	R.C.
Minimum	2.7	0.57	0.32	0.54	-0.68
25th percentile	5.3	1.01	1.3	2.2	-0.22
Median	6.2	1.05	1.8	3.3	-0.093
75th percentile	7.6	1.09	2.6	4.9	0.029
Maximum	24	1.11	28	57	0.51
Mean	6.6	1.05	2.2	4.1	-0.10
Std dev	2.1	0.06	1.7	3.4	0.19
Skewness	1.6	-1.62	4.4	4.8	-0.19
Excess kurtosis	6.0	7.68	42	51	-0.066
First value	8.4	0.93	3.1	7.2	-0.070
LADCP	5.1	0.90	1.9	6.4	-0.23

The time-varying temperature gradient used to calculate the buoyancy frequency affects the calculated κ_z. If we had instead used a constant temperature gradient of that measured at the nearest station of the deployment cruise (averaged over the appropriate depths), the range of κ_z would instead be $(0.3 - 62) \times 10^{-4}$ m^2 s^{-1}, with a median of 3.2×10^{-4} m^2 s^{-1}. Using the fit described above to extrapolate temperature, but replacing the fit for salinity with the average CTD salinity profile (i.e., not varying salinity with time), the range of κ_z would be $(0.5 - 54) \times 10^{-4}$ m^2 s^{-1}, with a median of 3.2×10^{-4} m^2 s^{-1}. The time series of κ_z calculated using a constant salinity profile is virtually indistinguishable from that calculated using the fitted salinities.

The distribution of the rotary coefficient (Fig. 3.8) is approximately normal, as indicated by the low skewness and excess kurtosis, and the mean value of -0.11 indicates weak upward energy propagation at these depths (1800 - 2400 m). The

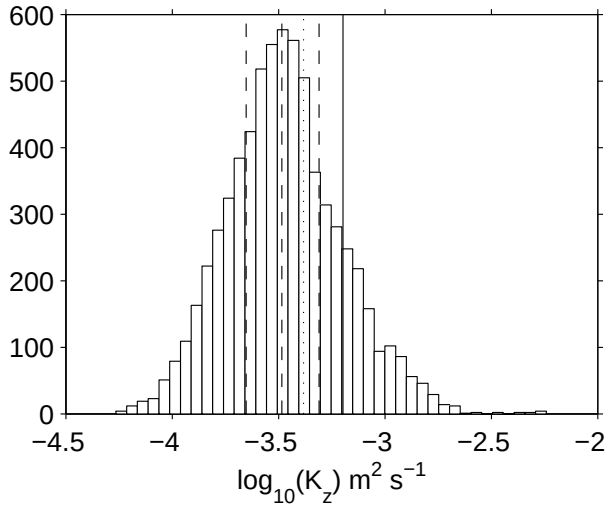

Figure 3.7: Distribution of time series diffusivity. The dashed lines are the 25th, 50th (median) and 75th percentiles, the dotted line is the mean, and the solid line is the diffusivity found by the LADCP, averaged over the waterdepth observed by the moored ADCP.

LADCP-derived rotary coefficient is only just within one standard deviation of the time series mean, but still lies well within the range of the time series. The rotary coefficient is relatively low at the start of the time series (Fig. 3.6), i.e., when the LADCP-derived value was obtained.

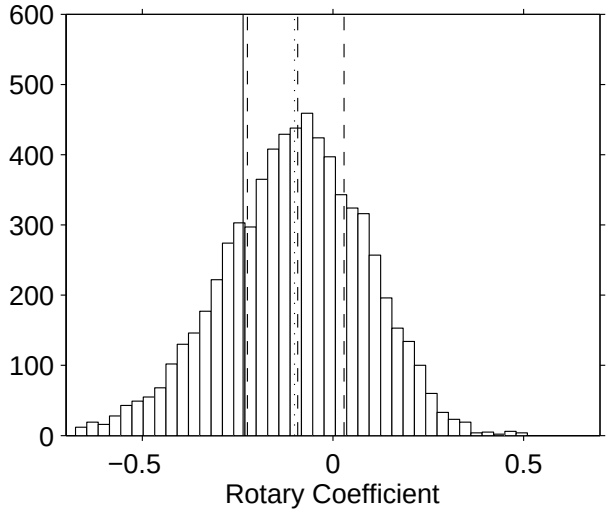

Figure 3.8: Distribution of time series rotary coefficient. The dashed lines are the 25th, 50th (median) and 75th percentiles, the dotted line is the mean, and the solid line is the rotary coefficient found by the LADCP, averaged over the waterdepth observed by the moored ADCP.

Comparison of these time series shows the separate effects of shear and buoyancy frequency in the derivation of κ_z: peaks in integrated shear variance appear as peaks in κ_z (with a particularly strong peak in October 2004), whereas peaks in buoyancy frequency appear as troughs in κ_z. Correlations between the time series (Table 3.3) show that integrated shear variance and κ_z are strongly correlated, with $r = 0.89$, whereas buoyancy frequency and κ_z are much more weakly anti-correlated ($r = -0.31$), indicating that variations in κ_z are dominated by variations in shear.

Table 3.3: Correlations between the time series of temperature (T) 600 mab, buoyancy frequency, integrated shear variance, dissipation rate, rotary coefficient and diffusivity, all after applying the running 24-hour mean. Values in bold are significant at the 95% confidence level.

	T	ISV	$\overline{N}$	ϵ	R.C.	κ_z
T	1	-0.19	**0.47**	-0.23	0.27	-0.26
ISV		1	-0.04	**0.94**	**-0.38**	**0.89**
$\overline{N}$			1	-0.15	0.15	**-0.31**
ϵ				1	**-0.39**	**0.98**
R.C.					1	**-0.40**
κ_z						1

The moderately strong correlation between temperature and buoyancy frequency ($r = 0.47$) is apparent in Fig. 3.6, although due to the nature of the fit used (Fig. 3.4) strong peaks in temperature appear as troughs in buoyancy frequency rather than peaks. The mooring lies very close to the Polar Front (Fig. 3.2), so we hypothesize that the front may have moved over the mooring, possibly multiple times during the 18 month deployment. The CTD stations confirm that the front moved over the mooring at least once: the deployment cruise CTD closest to mooring Shag2b is the coldest of the profiles (Fig. 3.4a) and lies to the south of the Polar Front, whereas the recovery cruise CTD taken at the same location is within the warmer group to the north of the Polar Front. Smith et al. (2010) observed that the front moved $\sim 1^\circ$ (65 km) to the west in 11 days during the deployment cruise. The temperature time series is not correlated with the velocity or shear, and the stratification of the CTD stations north and south of the front is similar (the range in buoyancy frequency is small), so the possible movement of the front during the mooring deployment does not have a strong influence on κ_z.

The weak anti-correlation between κ_z and rotary coefficient ($r = -0.40$) suggests that when the rotary coefficient is low, indicating more upward propagating energy (probably from internal waves generated at the topography), κ_z is high, presumably from more internal wave breaking. Fig. 3.6 reveals coincident troughs

in rotary coefficient and peaks in κ_z.

The effects of mooring knockdown and tilt have been considered. From the ADCP pressure record the maximum knockdown of 180 m occurred during a 2-week period of particularly strong currents in May 2003, but, during the rest of the record, the knockdown rarely exceeded 20 m. Similarly the pitch and roll reach maxima of $3°$ and $5°$ respectively during the same period, but otherwise rarely exceed $1°$. These are not thought to have a significant effect on the shear or buoyancy frequency, and thus on κ_z, for two reasons. Firstly, the depth, pitch and roll are not correlated with shear, buoyancy frequency or κ_z. Secondly, we considered what size of knockdown or tilt would be necessary to produce the observed ranges of shear and buoyancy frequency in the absence of varying currents and temperatures. The required knockdowns of nearly 700 m to produce the observed range in shear, and over 1500 m to produce the observed range in buoyancy frequency, are both greater than the total height of the mooring, and far exceed the observed knockdown. Buoyancy frequency will not be affected by the tilt, since it is extrapolated from temperature readings at the depth of the ADCP only. The tilt required to produce the observed range in shear is nearly $65°$; far greater than the observed range in pitch or roll. We therefore conclude that the variations seen in κ_z are caused by changes in the ocean's turbulent flow and not artefacts of the mooring motion.

3.5 Spectral Analysis

Using the multi-taper method (Thomson, 1982; Percival and Walden, 1993), we performed spectral analysis to search for significant periodicities which could be linked to a particular source of variability. Spectra are shown in Fig. 3.9 for the northward and eastward depth-mean velocities, temperature at 2400 m, ECMWF reanalysis wind speed at the nearest grid point to mooring Shag2b, integrated shear variance (both with and without the smoothing described in section 3.4.1.iv), buoyancy frequency, and κ_z with the smoothing described in section 3.4.1.iv. We include the smoothed integrated shear variance for ease of comparison with the smoothed κ_z. Each plot also shows the theoretical red noise spectrum calculated from the lag-1 auto-correlation coefficient for that variable, except for plot (e), the unsmoothed integrated shear variance. Since many oceanographic quantities are approximately red, this was used as a null hypothesis: peaks in the spectra are considered significantly different from a red noise background if they lie above the 95% confidence limit of the red noise spectrum.

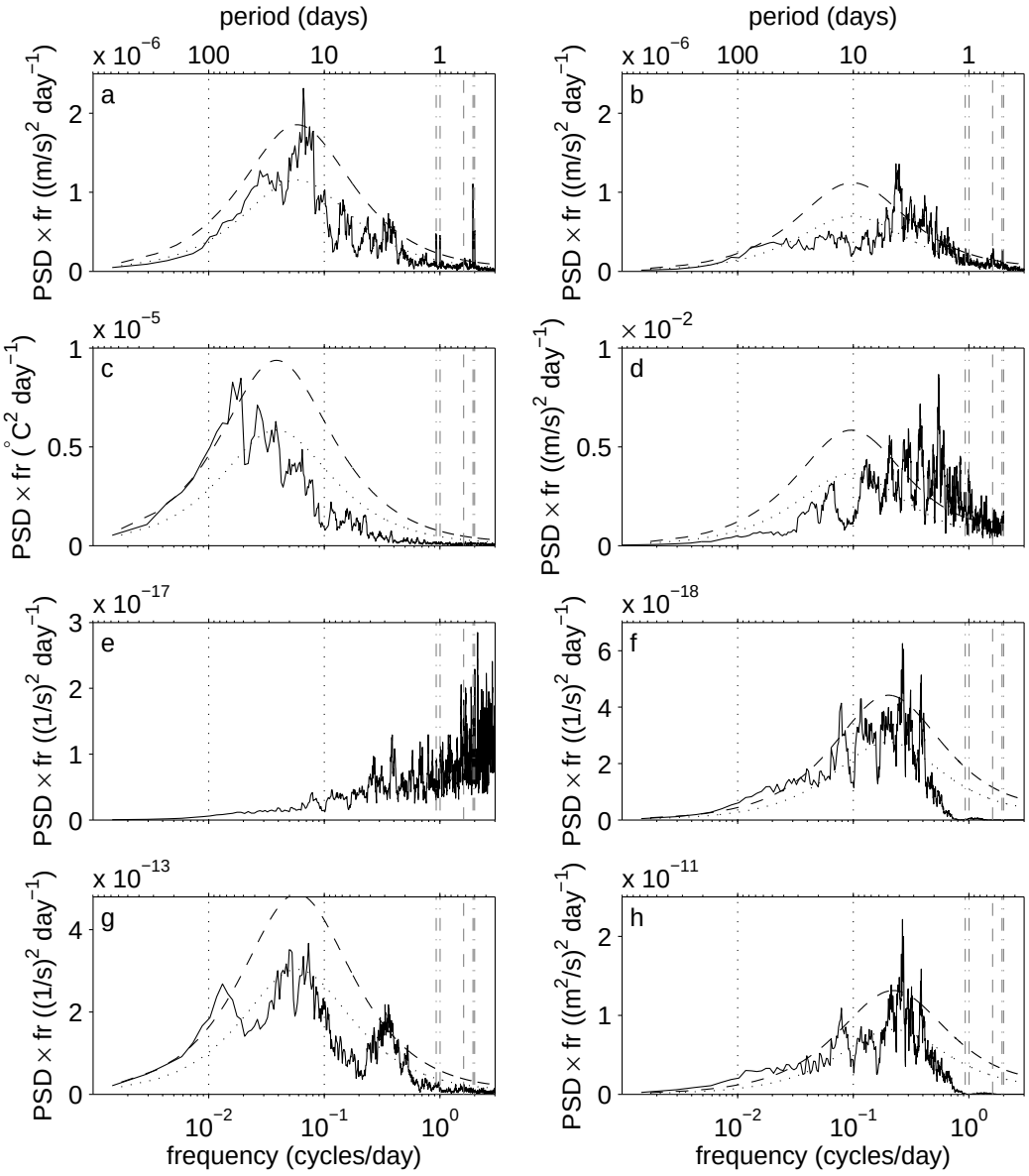

Figure 3.9: Variance preserving spectra. In each plot, the vertical axis is the power spectral density $\times$ frequency (PSD $\times$ fr). The dotted curve is the theoretical red noise spectrum based on the lag-1 auto-correlation coefficient, and the dashed curve is the 95% confidence limit. The vertical dashed line is the inertial frequency, and the vertical dot-dash lines are the main diurnal and semi-diurnal tidal frequencies. (These are O1, K1, M2 and S2 from left to right, although M2 and S2 are very close together and so may appear as one thick dot-dash line.) (a) Northward and (b) eastward depth-mean velocity: these are largely representative of the spectra for individual levels as the currents in this area are quite barotropic. (c) Temperature from the instrument located 600 mab. (d) 6-hourly ECMWF reanalysis wind speed at the nearest grid point to mooring Shag2b. (e) Integrated shear variance without the smoothing described in section 3.4.1.iv. (f) Integrated shear variance with the smoothing described in section 3.4.1.iv. (g) Buoyancy frequency. (h) κ_z with the smoothing described in section 3.4.1.iv.

The main diurnal (O1 and K1) and semi-diurnal (M2 and S2) tidal frequencies are visible in the velocities (Fig. 3.9a & b), particularly in the northward velocity. Very small peaks at the local inertial frequency (0.067 cycles/day, period 15.0 hours) are also present. The spectrum of the integrated shear variance calculated without the smoothing described in section 3.4.1.iv. (Fig. 3.9e) shows that the integrated shear variance is very energetic at high frequencies. This demonstrates the validity of the assumption stated in section 2 that subinertial shear is small compared with that in the internal wave field. Both the unsmoothed integrated shear variance and unsmoothed κ_z (not shown) are energetic at high frequencies, but do not display a particularly noticeable increase in activity at inertial, diurnal or semi-diurnal frequencies. While this might suggest that the inertial and diurnal/semi-diurnal tidal components of the velocities are barotropic rather than baroclinic, Sherman and Pinkel (1991) point out that small scale internal waves (which contribute the most shear) are vertically heaved by other internal waves. This Doppler shifts the encounter frequency as measured by a fixed mooring across frequency space so that the intrinsic frequency of the waves cannot be identified.

The northward (along-stream) velocity shows high spectral energy in a broad band from 10 to 60 days, with a noticeable peak around 14 days, the period of the spring-neaps tidal cycle, whereas the eastward (cross-stream) velocity is most energetic in the band from 2 to 5 days, with a particularly large peak at a period of approximately 4 days. Although the wind speed shows variability at periods between 6 hours and $\sim$6 days, it is not correlated or coherent with the current velocity, so is not a direct driver of that variability. Comparison with other ACC current meter velocities suggests that the topographic constriction in the east-west direction is responsible for the difference, in the energetic frequencies, exhibited by the northward and eastward velocities. Bryden and Heath (1985) examined moored current meter data southeast of New Zealand, and in central Drake Passage. Phillips and Rintoul (2000) examined moored current meter data in the ACC south of Australia. Both studies suggest that, in areas with topographic constrictions, the cross-stream velocity tends to exhibit variability at shorter periods than the along-stream velocity. The spectrum of the temperature time series shows rather different behavior to the velocities, with low variability at high frequencies but a significant peak at periods of $\sim$ 50 - 100 days. This is comparable to the temperature spectra found by Bryden and Heath (1985) and Phillips and Rintoul (2000).

The variability at periods of 10-20 days in the spectra of integrated shear variance and buoyancy frequency, and thus κ_z and rotary coefficient (spectrum not shown, but broadly similar to the spectra of κ_z and integrated shear variance),

is most likely due to the spring-neaps tidal cycle, combined with eddy activity, which several authors have reported as important at these periods (Bryden, 1979; Sciremammano, 1980; Bryden and Heath, 1985).

The large peak at a period of 3.8 days seen in the spectra of eastward velocity, integrated shear variance and κ_z is particularly unexpected. Bandpass filtering reveals that the signal is very persistent, appearing throughout the κ_z record, with an average amplitude of approximately 1.5×10^{-4} m^2 s^{-1}. It is not an instrumental fault as the same signal appears in the velocities recorded by the RCMs below the ADCP. It is not directly wind-driven, as the winds are neither correlated nor coherent with κ_z. Moreover, wind-driving would be expected to be apparent over a fairly wide area, and the velocities at moorings Shag1 and Shag3 (Fig. 3.1(c) and Table 3.1) do not show a signal at that period. It is not caused by seiching, as the constricted channel is too short in the north-south direction and too wide in the east-west direction to set up such a resonance. In 4 days, water is advected north by an average of 60km, which is more than the north-south length of the constriction. Bandpass filtering the velocities and plotting a progressive vector diagram (not shown) reveals that this east-west oscillation has an amplitude of approximately 5km. This is too great to be caused by mooring motion since the ADCP is only 600 m off the sea floor, and spectra of the mooring's depth, pitch and roll do not reveal a large 3.8-day signal. One remaining possibility is topographically-trapped Rossby waves propagating around the local seamount. The mooring is located on the north-east flank of a seamount (Fig. 3.1(c) and Fig. 3.2) with a radius of $\sim$15 km at its base, and a slope of $\sim$55 m/km. LeBlond and Mysak (1978) state that wave-trapping by a cylindrical seamount (i.e., a seamount with vertical sides) is only possible if the radius of the seamount is greater than the barotropic Rossby radius (1300 km in Shag Rocks Passage, so much greater than the radius of this seamount). However, subinertial waves can be trapped by a seamount with sloping sides (Rhines, 1969; Brink, 1989; Sanson, 2010) even if the radius of the seamount is less than the barotropic Rossby radius.

Using the model of Brink (1989) with the stratification observed during the deployment cruise and an idealised, axisymmetric seamount (Fig. 3.10) of similar height, radius and slope to the one immediately west of the mooring, we find trapped waves with azimuthal wavenumber $n = 1$ and a frequency of 3.0 $\times 10^{-6}$ s^{-1} (period 3.8 days), consistent with the observed primary peak in the κ_z spectrum of 3.8 days. (Model downloaded 6/20/2011 from http://www.whoi.edu/page.do?pid=23361.) At $n = 2$ the model finds a trapped wave with a frequency of 4.5 $\times 10^{-6}$ s^{-1} (period 2.6 days), consistent with the second most prominent peak in the spectrum of κ_z.

Although the velocities in Fig. 3.9(a) and (b) do not have obvious peaks at a period of 2.6 days, these are the spectra of the depth-mean velocities, i.e., the barotropic component. The integrated shear variance (Fig. 3.9f) has peaks at periods of 3.8 days and 2.6 days, indicating that these are baroclinic motions. Such baroclinic motions can increase the internal wave shear variance and thus κ_z.

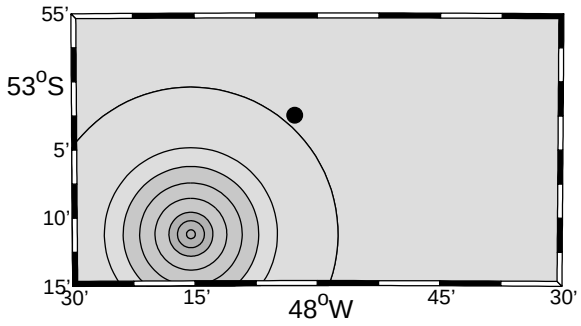

Figure 3.10: Idealised axisymmetric seamount used with the Brink model, for comparison with Fig. 3.1d. Contour intervals are every 200m with shading every 600m in the same colors as Fig. 3.1d. The black circle is mooring Shag2b.

3.6 Conclusions

An 18-month time series of internal wave driven diapycnal diffusivity from Shag Rocks Passage was inferred from fine scale shear using a method modified from that used to calculate κ_z from LADCP shears. The mean κ_z was 4.1×10^{-4} m^2 s^{-1}, consistent with the value obtained from LADCP data of 6.4×10^{-4} m^2 s^{-1} at the depths ensonified by the moored ADCP. κ_z varies by a factor of just over 100, much greater than the factor of 3-4 uncertainty inherent in the method (Polzin et al., 2002), from 0.5×10^{-4} to 57×10^{-4} m^2 s^{-1}. This range is slightly greater than the spatial variability seen in Shag Rocks Passage at the same depths as ensonified by the moored ADCP. The record shows no obvious annual or semiannual cycle, despite being at a high latitude where seasonality is often quite marked. The record displays variability over timescales of 10 to 20 days thought to be driven by eddy activity and the spring-neap tidal cycle, and variability at periods of 3.8 and 2.6 days most likely due to topographically-trapped waves propagating around the local seamount. κ_z is anti-correlated with the rotary coefficient (indicating that stronger mixing occurs during times of upward energy propagation), which suggests that mixing occurs due to the breaking of internal waves generated at topography. We

have demonstrated that time series can, to an extent, shed light on the mechanisms causing mixing.

The results presented here are from a single moored ADCP in a rather atypical location, where a strong flow is extremely constrained by the topography. The moorings used were not designed to measure κ_z, but we have demonstrated that the method used to calculate κ_z from CTD/LADCP profiles can be adapted for use with moored instruments. If measuring κ_z were the aim, then in regions with a less stable temperature-salinity relationship, or where a linear temperature gradient is not an appropriate assumption, the moorings would need to include temperature and salinity sensors spanning the depth range ensonified by the moored ADCP. It is also necessary to programme the ADCP to provide both sufficient vertical resolution, and enough depth bins to perform a Fourier transform in the vertical. The vertical sampling frequency must be at least twice the largest wavenumber included in the integration, i.e. the length of the depth bins must be, at most, half the smallest wavelength included. Moreover, finescale parameterizations have not been assessed for depth bins greater than 20m. We would therefore recommend using depth bins of no more than 20-40 m. The decision on what constitutes 'enough' depth bins is rather heuristic, but we would recommend a minimum of 15-20 bins of good data (i.e. after the data quality control cuts, such as that based on the percentage of good beam solutions, have been made).

Time series at other locations will be important in assessing whether diapycnal mixing commonly varies over a similar range, or whether this is simply a feature of this particular location. In the Scotia Sea region, there is considerable atmospheric variability such as storms and seasonal cycles, and in the ocean, variability includes extensive eddy activity, strong currents, and movement of fronts. Shag Rocks Passage has complex topography, with which varying water motions can interact. We postulate that other regions with less atmospheric and oceanic variability, and less complex topography, may experience less temporal variability in κ_z at the depths observed here. We are therefore cautiously optimistic about the validity of 'snapshots' of κ_z, though we would prefer to see further studies of temporal variability over at least a year at a range of locations, especially since local topography (e.g., small seamounts) can provide variability on timescales unrelated to large-scale atmospheric forcing.

Chapter 4

Supplementary Material for the Shag Rocks Passage Study

4.1 Introduction

This chapter expands on two aspects of the study in Shag Rocks Passage discussed in chapter 3. Firstly, it will discuss how we addressed the need for a time series of buoyancy frequency (N) for use in the calculation of diffusivity (κ_z). This was problematic because the ADCP was the uppermost instrument on the mooring, so there were no temperature and salinity sensors in the water depths ensonified by the moored ADCP. Secondly, we will discuss the use of models to assess the effects of the seamount in Shag Rocks Passage on the variability in the time series of κ_z.

4.2 Buoyancy Frequency

A number of methods, of varying complexity, to provide a time series of N were considered. As discussed in section 3.4.1, time series of temperature and salinity were not measured in the volume of water ensonified by the ADCP, but there was a temperature sensor on the ADCP, and on the three rotary current meters (RCMs) in the water column below (Table 3.1). Some different approaches to using these time series to provide time series of temperature and salinity (and hence buoyancy frequency) appropriate to the water column monitored by the ADCP, were considered.

i The simplest approach would be to hold N constant, in which case the temporal variability in the calculated κ_z would be entirely due to variability in the shear. Using a constant value of N, calculated from the CTD profile

of the nearest deployment station to the mooring location and averaged over the water depths ensonified by the moored ADCP, gave the time series of κ_z shown in Figure 4.1b. This value of N is shown as the white diamond in Figure 4.1a. While straightforward, this was not considered to be an adequate solution, as the stratification is unlikely to be constant.

ii Hold salinity constant at the values of the CTD profile of the nearest deployment station to the mooring location. Use the various temperature times series to provide a time series of temperature gradient, which can then be used to extrapolate temperature upwards to the water depths ensonified. This relies on the assumption that the gradient of temperature is the same above and below the ADCP. The CTD data taken during the deployment and recovery cruises do show largely similar gradients above and below the ADCP (Figure 3.4a). At each time step, the mean of the temperature gradients between each pair of the three temperature sensors on the RCMs (30, 100 and 400 metres above bottom (mab)) was calculated. Then, using $y = mx + c$, where x is the depths ensonified, m is the gradient at each time step, and c is the temperature recorded by the sensor on the ADCP at each time step, it was possible to extrapolate y, the temperature at each depth ensonified, for each time step. N was then calculated in the usual way, and the time series of N is shown in Figure 4.1a in blue, with the resulting κ_z in Figure 4.1c.

iii Follow the temperature gradient approach above, but use a fit to the T - S relationship (in-situ temperature and absolute salinity, respectively) of the deployment and recovery cruise CTD profiles, to also infer a time series of salinity. A cubic fit was found to be a good match to the CTD profiles (Fig. 4.2). As discussed in section 3.4.1, the most important component of this process, in terms of the impact on the calculated κ_z, is the temperature gradient; the effect of salinity on N is, in essence, an enhancement of the effect of the temperature gradient. The times series of N calculated in this way is shown in Figure 4.1a in green, with the resulting κ_z in Figure 4.1d.

iv The final approach used did not involve the temperature extrapolation described in (ii) above. Instead, the CTD temperature gradient between 1800 and 2400 m (1200 and 600 mab, respectively, the depth range ensonified by the moored ADCP), of the deployment and recovery cruise stations in Shag Rocks Passage, was fitted to the temperature at 2400 m for each of

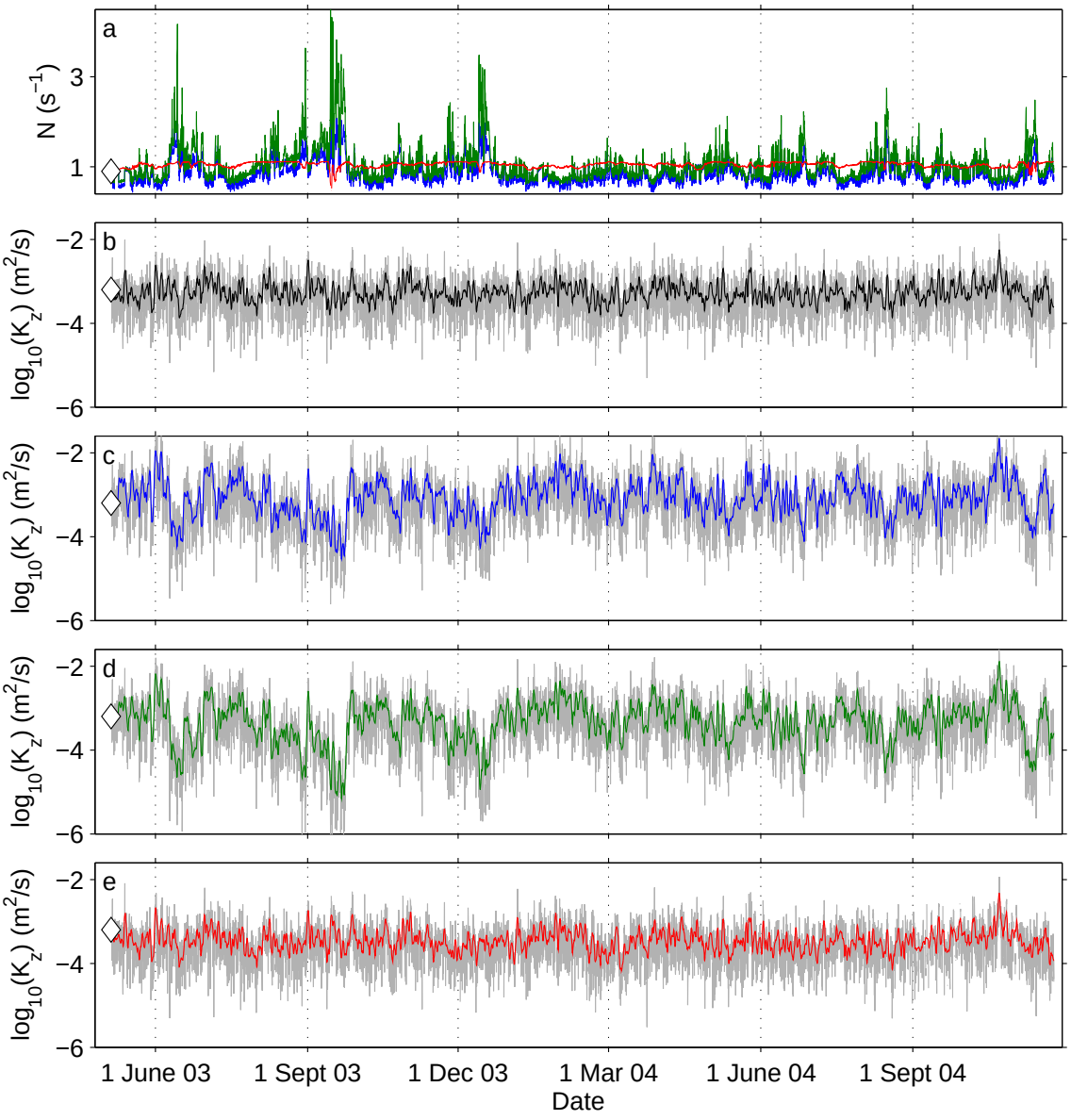

Figure 4.1: Times series of buoyancy frequency and diffusivity in Shag Rocks Passage. (a) Buoyancy frequency ($\times 10^{-3}$ s^{-1}) found in different ways: blue as described in (ii) in the text, green as described in (iii) in the text, red as described in (iv) in the text. The white diamond is buoyancy frequency at station 56 of the deployment cruise, averaged over the depths observed by the moored ADCP. (b)-(e) Log$_{10}(\kappa_z)$ (m^2 s^{-1}). In each plot, the grey line is the unsmoothed quantities, the coloured/black line is daily average values, and the white diamond is that recorded at station 56 of the deployment cruise, averaged over the depths observed by the moored ADCP. (b) The black line is κ_z found by holding N constant, as described in (i) in the text. (c)-(e) κ_z found using the time series of N in (a) of the same colour.

those stations. Fig. 3.4(b) illustrates the cubic fit which was found to best reproduce the observed temperature profile. The cubic fit to the CTD stations was used, in conjunction with the temperature at 2400 m recorded by the ADCP, to generate temperature gradients, and thus temperatures, between

1800 and 2400 m for the entire time series. The cubic fit for salinity described in (iii) above was also used. The resulting times series of N is shown in Figure 4.1a in red, with the resulting κ_z in Figure 4.1e. These are the same time series previously shown in Figure 3.6e and g.

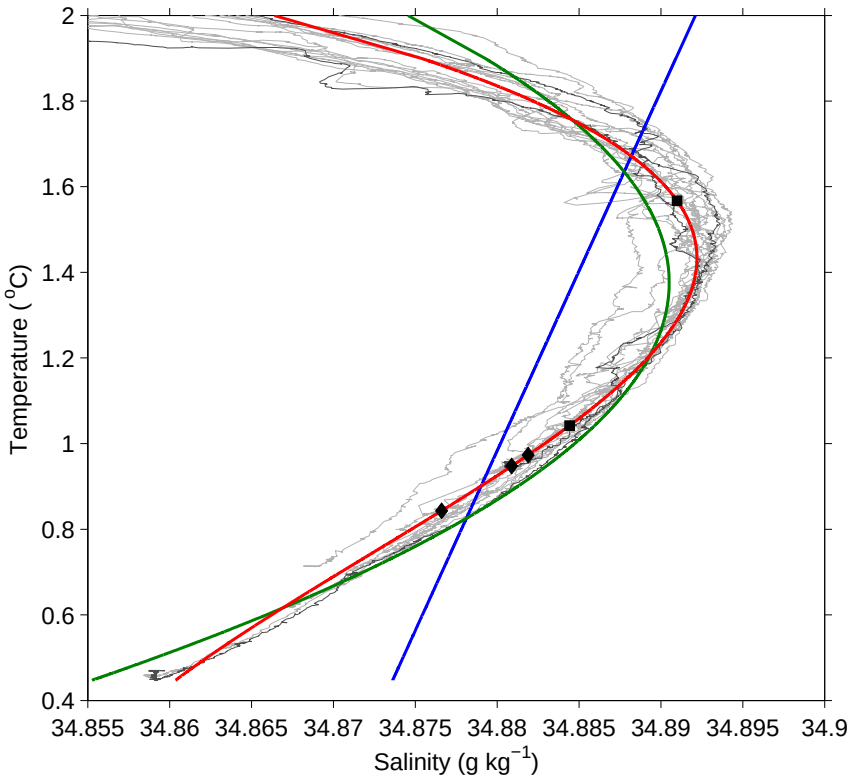

Figure 4.2: Fitting salinity to temperature as part of the derivation of the time series of buoyancy frequency. The grey lines are profiles of the Shag Rocks Passage CTD stations (deployment and recovery cruises), with the darker grey being the closest station of each cruise. The coloured lines represent possible salinity fits: blue = linear, green = quadratic, red = cubic. The black diamonds and squares represent the mean T–S values at 30 mab, 100 mab, 400 mab (diamonds), 600 mab and 1200 mab (squares) using the chosen cubic fit. The water depths ensonified by the moored ADCP lie between the two black squares, the diamonds are at the depths of the rotary current meters.

The goodness of fit of the various extrapolation methods for N can be illustrated using the CTD profiles in Shag Rocks Passage. Using the temperatures at the depths of the RCMs and the ADCP on each profile, N was calculated using each of the extrapolation methods above. In Figure 4.3, these are plotted against the real values of N for each CTD profile (all averaged over the depths ensonified by the moored ADCP). It is clear that the final approach (in red) is best, since the extrapolated values lie closer to the black line, which indicates where extrapolated values are equal to the real values. The temperature extrapolation described in (ii) above was

not the best way to proceed. The absolute accuracy of the built-in temperature sensors on RCM8 current meters is not comparable to that of high-precision (e.g. MicroCAT) CTD-loggers, such as on a ship's CTD, or that mounted on the moored ADCP. Moreover, the lowest RCM is located only 30 m above the bottom. This position is quite likely inside the bottom boundary layer, where there might be substantially reduced stratification. Finally, the assumption that the gradient of temperature is the same above and below the ADCP may not be justified. Together, these issues introduce considerable (non-realistic) variability in the calculated N, and thus in κ_z. A more conservative approach, as described in (iv), was better.

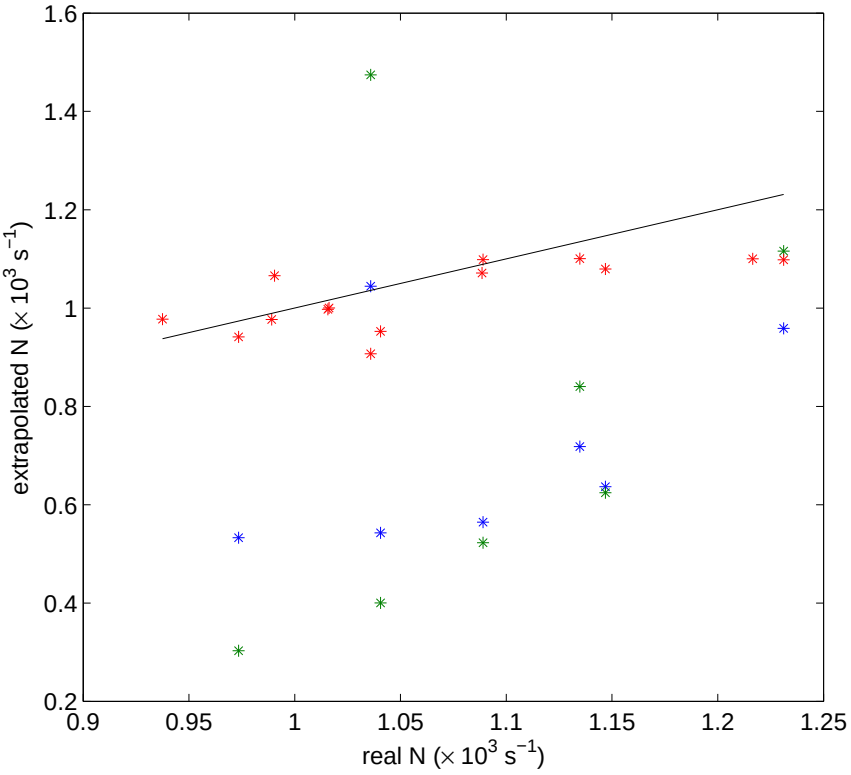

Figure 4.3: Goodness of fit for the various methods of extrapolating N. Using the temperatures, on each CTD profile, at the depths of the three RCMs and the ADCP, N was extrapolated as described in the text, then plotted against the real N of the same profile. (All values $\times 10^3$, all averaged over the depths ensonified by the ADCP.) Blue as described in (ii), green as described in (iii), red as described in (iv). The black line is $y = x$, i.e., extrapolated values equal to real values.

In Figure 4.1, we see that the final approach (in red) greatly reduces the overall variability in both N and κ_z, compared with the other extrapolation methods. Table 4.1 gives the mean, median and range of N and κ_z calculated by the various extrapolation methods. The κ_z range for method (iv) is fairly similar to that for a

constant N (method (i)), indicating that the final extrapolation approach did not substantially increase the variability in κ_z beyond the variability produced by the changing shear.

Table 4.1: Mean, median and range of N and κ_z, calculated using the various extrapolation methods discussed in the text. All values given to 2 s.f., except for N calculated by extrapolation method (iv) which is given to 2 d.p. in order to distinguish the mean, median and maximum. All κ_z values are after applying the running 24-hour mean.

Extrapolation	$\kappa_z \times 10^{-4}$ m^2 s^{-1}			$\overline{N} \times 10^{-3}$ s^{-1}		
Method	Mean	Median	Range	Mean	Median	Range
i	6.3	5.2	1.0 - 67	0.90		
ii	13	8.5	0.22 - 270	0.87	0.82	0.43 - 2.4
iii	7.8	5.2	0.049 - 160	1.0	0.94	0.60 - 4.6
iv	4.1	3.3	0.54 - 57	1.05	1.06	0.48 - 1.11

4.3 Models used to assess the effect of the seamount

Two models were used to consider the effect of the seamount on the variability in the time series of velocity, shear, and hence diffusivity, at the mooring site discussed in chapter 3. Notable features in the time series at periodicities which are not readily explained by other mechanisms are the 4-day signal in the eastward velocities, and the 3.8-day and 2.6-day signals in the integrated shear variance (section 3.5 and Fig. 3.9a & f). The first is barotropic (seen at all depths in the velocities), but the 3.8-day and 2.6-day signals are baroclinic, appearing strongly in the shear. The first model discussed below is for barotropic trapped waves, and is based on the work of Sanson (2010). The second model discussed is for baroclinic trapped waves, and is based on the work of Brink (1989). Here we describe the setup of both models and the methodologies for determining the periodicities that might be caused by waves propagating around the seamount in Shag Rocks Passage. This expands on the results quoted in chapter 3.

4.3.1 Barotropic Waves

4.3.1.1 Model Description

Sanson (2010) derives exact solutions of the linear, barotropic, shallow-water equations with a rigid lid to give a dispersion relation for barotropic trapped waves around axisymmetric seamounts. In polar coordinates the linear shallow-water

equations for a homogeneous fluid layer in a rotating system are:

$$\begin{aligned} u_t - fv &= -g\eta_r \,, \\ v_t + fu &= -\frac{g}{r}\eta_\theta \,, \\ \frac{1}{r}(rhu)_r + \frac{1}{r}(hv)_\theta &= 0 \,. \end{aligned} \tag{6}$$

Here, and in equations 10 below, the radial, azimuthal and vertical directions are given by (r, θ, z) and velocities by (u, v, w), f is the Coriolis parameter (assumed constant), g is the acceleration due to gravity, and subindices denote partial derivatives. η is the free-surface deformation, and h is the fluid-layer depth. Drag is assumed to be zero. The rigid lid approximation has been applied in the continuity equation: the fluid depth $h(r)$ is time-independent. Since we are considering an axisymmetric seamount only, the fluid depth is also independent of θ.

An approximate analytical solution for these equations was first found by Rhines (1969) for topography in which the fluid depth increases proportionally to exp(r^2), where r is the radial distance from the centre of the seamount. Sanson (2010) expands on this by deriving exact (rather than approximate) analytical solutions of the barotropic problem, valid for a wider range of topographies from flat-topped seamounts or guyots to sharp, cone-shaped seamounts. The shape of the seamount is modelled as

$$h(r) = h_0 \exp(\lambda r)^s \,, \tag{7}$$

where r is the radius, $h(r)$ is the water depth at radius r, h_0 is the water depth at the summit of the seamount, λ^{-1} is the horizontal length scale of the seamount, and the real number $s > 0$ is a parameter which measures the shape of the seamount. Fig. 4.4 shows example seamount profiles for different values of s and λ, values chosen to include those used for the seamount in Shag Rocks Passage ($s = 1$ and $\lambda^{-1} = 20$ km).

The derived dispersion relation of the waves takes the form

$$\frac{\omega}{f} = \frac{n}{sp + n} \,, \tag{8}$$

where ω is the wave frequency, f is the inertial frequency, $n \geqslant 0$ is the azimuthal wavenumber and $p \geqslant 0$ the radial wavenumber, with n and p integers. The angular phase speed of waves propagating around the seamount is given by

$$c_{n,p}(s) = \frac{\omega}{n} = \frac{f}{sp + n} \,, \tag{9}$$

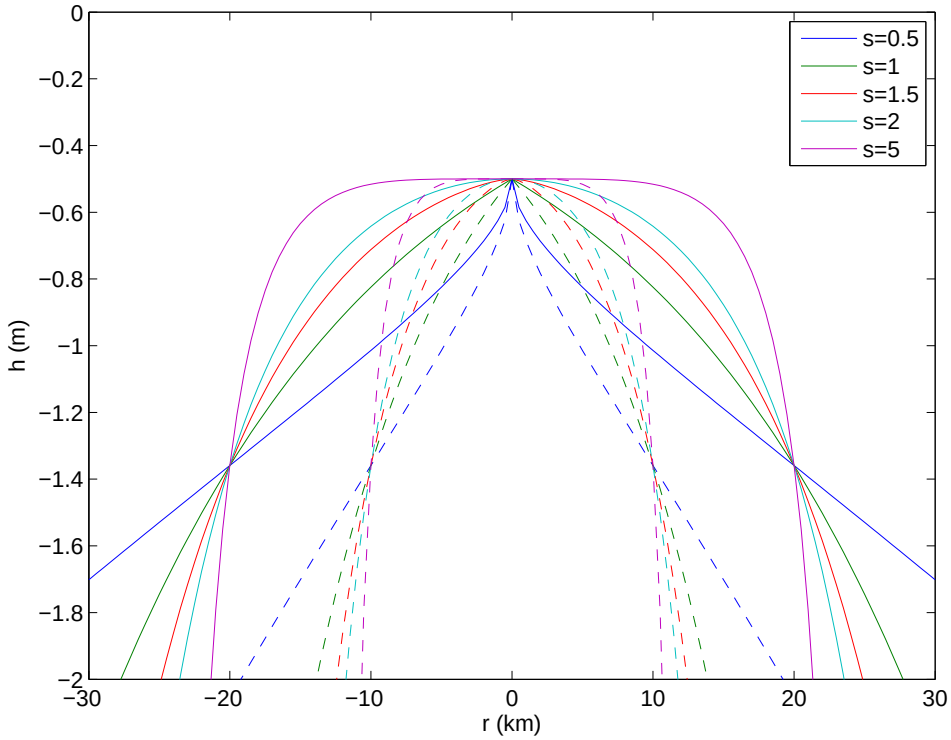

Figure 4.4: Depth profiles over seamounts of the form $h(r) = h_0 \exp(\lambda r)^s$, where $h_0 = -500$ m. Dashed lines have $\lambda^{-1} = 10$ km, solid lines $\lambda^{-1} = 20$ km.

showing that waves rotate around the seamount with angular speeds c depending inversely on s, n and p. In the southern hemisphere, waves will propagate in an anti-clockwise direction.

Thus, for a seamount whose shape is described by h_0, λ and s, solutions exist with various radial and azimuthal wavenumbers, and thus various frequencies and phase speeds. $h(r) = h_0 \exp(\lambda r)^s$ is a fairly crude approximation to the shape of the real seamount so the solutions found will be only crudely representative of the waves around the real seamount. These solutions are also barotropic, i.e., appropriate for single-layer fluids. The observed stratification is weak (N typically $\sim 8 - 9 \times 10^{-4}$ s^{-1} at the depths ensonified by the moored ADCP), but it is not zero. These solutions could, however, suggest whether a barotropic signal with a period of 4 days, as seen strongly in the eastward velocities (section 3.5 and Fig. 3.9), might reasonably be considered a consequence of the presence of barotropic waves propagating around this seamount. Prior to this analysis, we were unaware if a period of 4 days was even the right order of magnitude for barotropic waves propagating around this seamount.

The real seamount is not axisymmetric and has many irregular features. Fig. 4.5

shows the seamount and the bathymetric profiles of some example transects through the seamount. Also shown is a bathymetric profile of the form $h(r) = h_0 \exp(\lambda r)^s$, with $h_0 = 1790$ m, $s = 1$ and $\lambda^{-1} = 20$ km, which is crudely representative of the real bathymetry, and is in the form required to make use of the Sanson (2010) solutions.

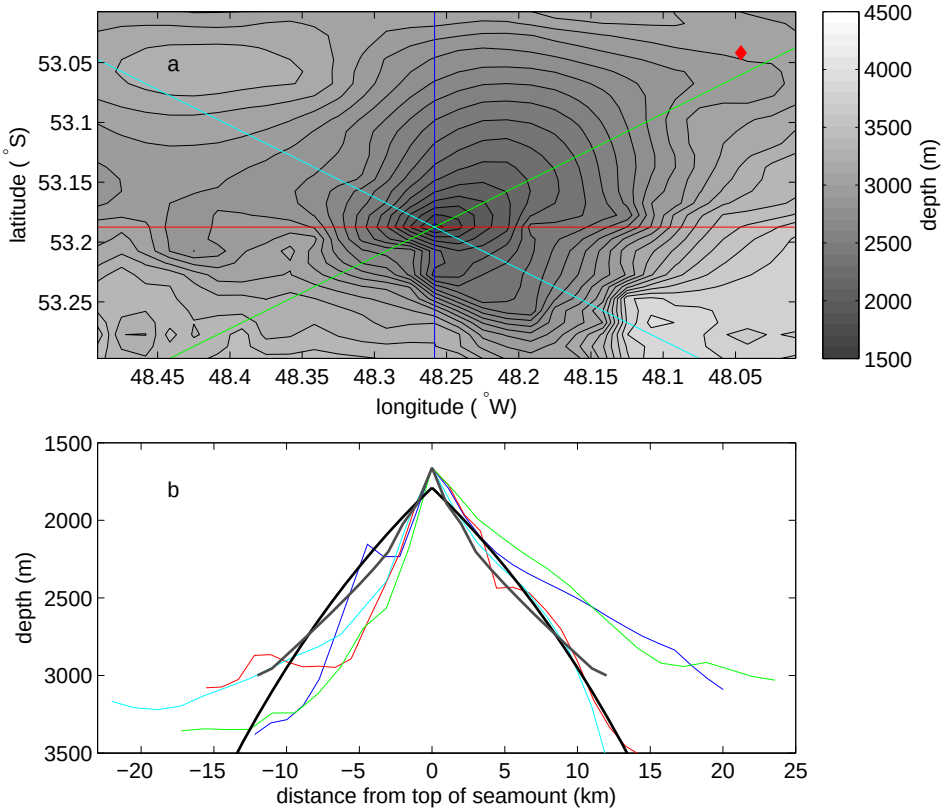

Figure 4.5: (a) Bathymetry of the seamount in Shag Rocks Passage from Smith and Sandwell (1997). Contour intervals are every 100 m. The location of mooring Shag 2b is shown as a red diamond. Coloured lines show the example transects whose bathymetric profiles are shown in panel (b) in the same colours as the transect lines in (a). The thick black line in (b) has the form $h(r) = h_0 \exp(\lambda r)^s$, with $h_0 = 1790$ m, $s = 1$ and $\lambda^{-1} = 20$ km. The thick grey line in (b) is the bathymetric profile used with the baroclinic model in section 4.3.2, included here for comparison.

4.3.1.2 Predicted Frequencies

The dispersion relation for a seamount with $s = 1$ (Fig. 4.6), was calculated using equation 8 for different values of n and p. Waves exist only at discrete points (integer values of n and p), though for clarity dashed lines connect points of equal p. Waves exist at a range of different frequencies, but only solutions with $n = 1$

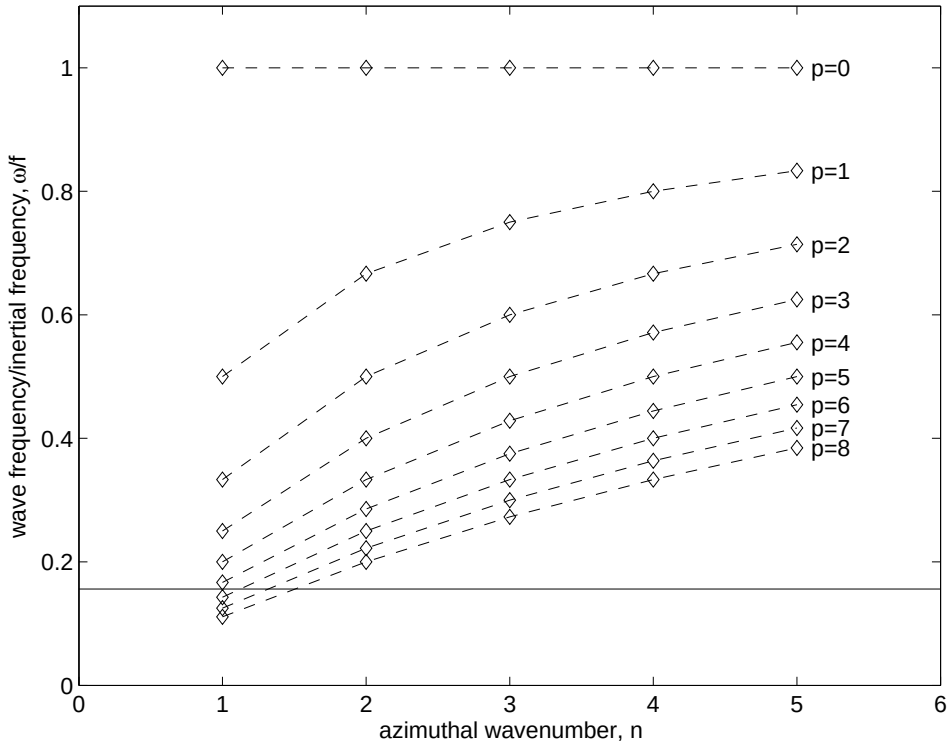

Figure 4.6: Dispersion relation for waves over a seamount calculated using $s = 1$, $f = 1.17 \times 10^{-4}$ s^{-1} (i.e., at a latitude of 53°, the latitude of the centre of the seamount). Valid frequencies are indicated with diamonds, dashed lines are used for clarity. The solid horizontal line indicates a period of 4 days (again at a latitude of 53°), i.e., $\omega/f = 0.16$.

have frequencies low enough to be of interest for explaining a signal with a period of 4 days.

The solution with azimuthal wavenumber $n = 1$ and radial wavenumber $p = 5$ has a frequency of 3.1×10^6 s^{-1} (period 3.7 days), and the solution with $n = 1$ and $p = 6$ has a frequency of 2.6×10^6 s^{-1} (period 4.4 days). These waves would propagate in an anti-clockwise direction around the seamount, with tangential phase speeds, at the distance of the mooring from the centre of the seamount, of 0.19 and 0.17 m s^{-1} respectively. Note that this is the speed of propagation of peaks/troughs of the barotropic wave, which is quite distinct from the velocity of the water. While this does not provide definitive proof that the seamount is responsible for the 4-day peak observed in the eastward velocities, it does suggest that the presence of the seamount is a plausible explanation for this barotropic signal.

4.3.2 Baroclinic Waves

We now turn to a discussion of the baroclinic signals observed in the integrated shear variance with periods of 3.8 and 2.6 days (section 3.5), which cannot be explained by a barotropic model. Brink (1989) discusses the effect of stratification on seamount-trapped waves, and thus the existence of baroclinic trapped waves around seamounts as well as barotropic. The model developed for Brink's work is made available at http://www.whoi.edu/page.do?pid=23361, and was used here to model the effect of the seamount in Shag Rocks Passage.

4.3.2.1 Model Description

Brink's model is a numerical model which calculates dispersion relations for seamount-trapped waves at subinertial frequencies in a stratified ocean. The main assumptions are a rigid-lid ocean surface, that the seamount is axisymmetric, the equations of motion are linearized, and the bottom boundary layer is infinitesimally thin. The Boussinesq approximation will be made throughout. The equations of motion are:

$$\begin{aligned} u_t - fv &= -\frac{1}{\rho_0} p_r + \frac{1}{\rho_0}\tau_z^r \,, \\ v_t + fu &= -\frac{1}{r\rho_0} p_\theta + \frac{1}{\rho_0}\tau_z^\theta \,, \\ 0 &= -p_z - g\rho' \,, \\ \frac{1}{r}(ru)_r + \frac{1}{r}(v)_\theta + w_z &= 0 \,, \\ \rho'_t + w\rho_{0z} &= 0 \,. \end{aligned} \tag{10}$$

In addition to the variables defined above (equations 6), p represents pressure, τ^r and τ^θ are turbulent vertical stresses in the radial and azimuthal directions respectively (i.e., representing drag), and density is given by

$$\rho = \rho_0(z) + \rho'(r, \theta, z, t) \,, \tag{11}$$

where $|\rho'| \ll \rho_0$.

4.3.2.2 Model Inputs and Sensitivity Tests

The necessary inputs to Brink's model are the stratification, in the form of a depth profile of N^2, and the shape of the seamount. Fig. 4.7 shows two N^2 profiles considered, along with the profile calculated from the nearest CTD station of the deployment cruise. A smoothed profile with only a few data points is necessary as a

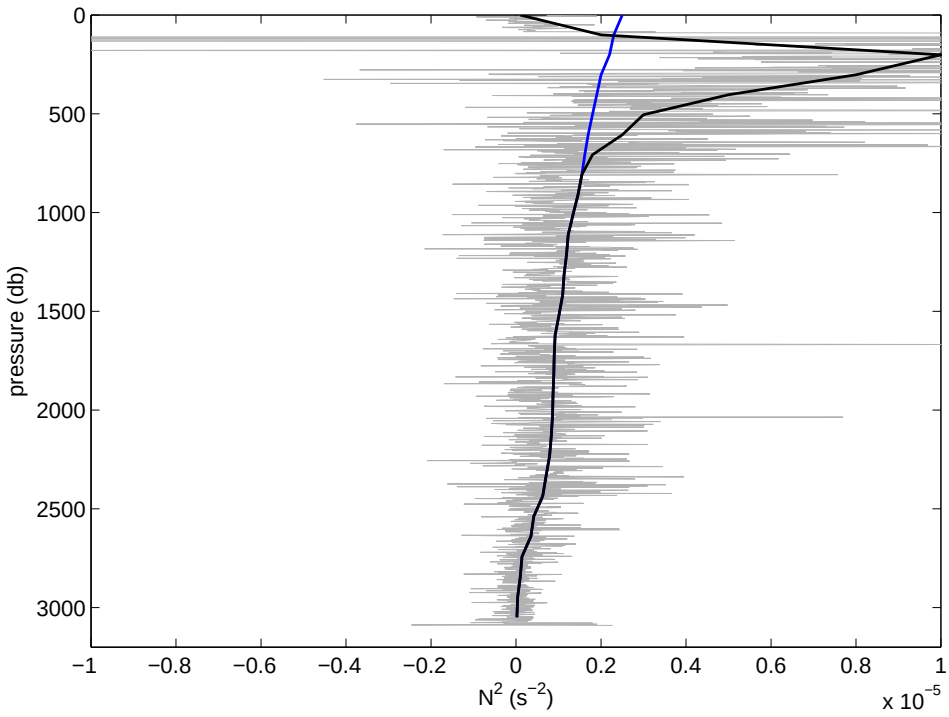

Figure 4.7: Profile of the squared buoyancy frequency at mooring Shag 2b. The grey line is the observed profile, the black and blue lines are two different smoothed profiles used as inputs to the Brink model. (The blue and black profiles are the same below 800 m.)

model input for numerical stability. By comparing the results found with these two N^2 profiles, we can determine if the model output is sensitive to the N^2 profile in the upper part of the water column. The blue profile will henceforth be referred to as "N^2 profile 1", and the black profile as "N^2 profile 2".

It was again necessary to produce an idealized topography which is a reasonable axisymmetric approximation to the real topography. However, since this numerical model does not require topography of a particular shape, a better approximation to the shape of the real seamount can be used than for the barotropic model. Two possible methods for producing an idealised axisymmetric bathymetry were considered: averaging depths at given distances from the top of the seamount, or averaging distances at given depths. The distance from the centre of the seamount was calculated for each latitude/longitude grid point. For the first method, grid points were binned every 1 km from the centre of the seamount, and the depths in each bin averaged. The depth profile acquired in this way is the blue line on Fig. 4.8. For the second method, grid points were binned every 100 m depth, and distances from the centre of the seamount in each bin averaged (green line on Fig. 4.8).

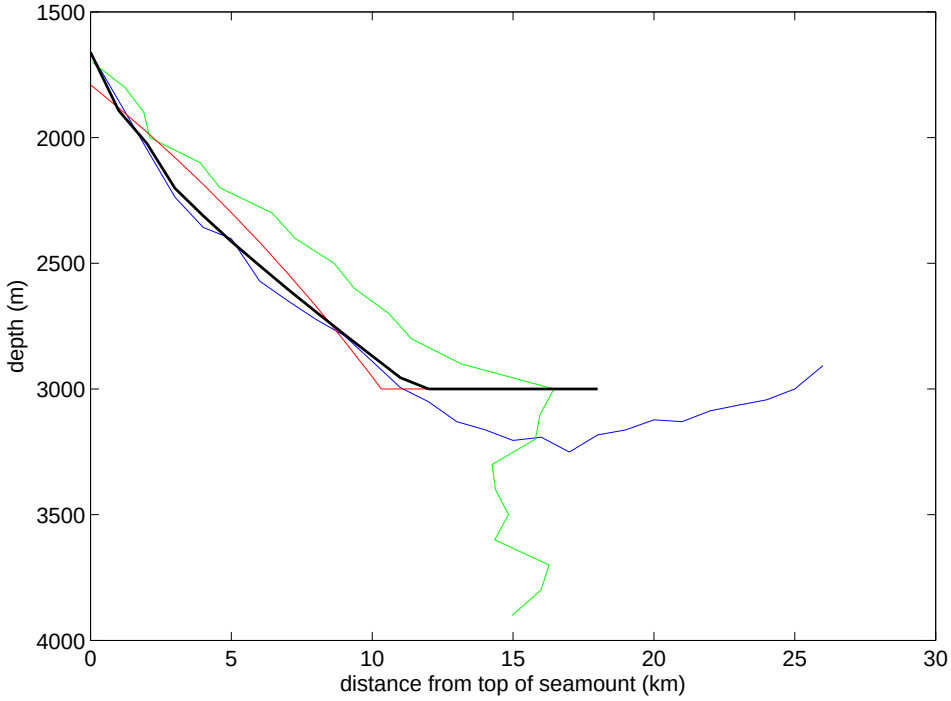

Figure 4.8: Profiles of the seamount bathymetry. The thick black line is the idealised bathymetry used as an input to the Brink model in chapter 3, and in Fig. 3.10. The green and blue lines are averages of the observed bathymetry: the blue line is found by averaging depths for given radii, and the green line by averaging radii for given depths. The red line is the seamount profile used with the Sanson model, with a bottom depth of 3000 m.

The second method, averaging distances at given depths, was found to be affected more severely by the non-axisymmetric nature of the real seamount. In Fig. 4.5a, we see that the bathymetry becomes rapidly deeper on the south-east side of the seamount, but flattens out more on the west side. At depths below around 3000 m, this pattern results in the distance averaged at given depths being approximately constant, which is not a good approximation to the shape of the seamount. Near the top of the seamount, averaging distances in depth bins means that large numbers of points from the shallow east side of the seamount are included in any given depth bin, but only a few points from the steep south-western side. Again, this does not result in a good approximation to the shape of the seamount. Therefore, the bathymetry profile found by the first method, averaging depths at given distances from the top of the seamount, was used. The black line in Fig. 4.8 is the actual idealized bathymetry input to the model used to produce the results given in chapter 3. This seamount profile will henceforth be referred to as "seamount profile 1". The red line is the seamount profile used with the barotropic model, which has the form $h(r) = h_0 \exp(\lambda r)^s$, where $h_0 = 1790$ m, $s = 1$ and $\lambda^{-1} = 20$

km. This profile, which will henceforth be referred to as "seamount profile 2", was also input to the Brink model, to determine if the results are sensitive to the shape of the seamount.

4.3.2.3 Results and Discussion

The frequency of the topographically-trapped waves was found to be sensitive to the shape of the seamount but not to the N^2 profile. Table 4.2 gives the frequencies and periods of topographically-trapped waves with azimuthal wavenumbers $n = 1$ and $n = 2$, found by Brink's model using different N^2 and seamount profiles.

Table 4.2: Frequency and period of topographically-trapped waves with azimuthal wavenumber $n = 1$ and $n = 2$, found by Brink's model using different N^2 and seamount profiles.

		$n = 1$		$n = 2$	
		N^2 profile 1	N^2 profile 2	N^2 profile 1	N^2 profile 2
seamount profile 1	ω ($\times 10^{-6}$ s^{-1})	2.969	3.000	4.460	4.461
	period (days)	3.90	3.86	2.59	2.59
seamount profile 2	ω ($\times 10^{-6}$ s^{-1})	2.000	2.000	3.996	3.995
	period (days)	5.79	5.79	2.90	2.90

These results show that it is plausible for the seamount in Shag Rocks Passage to produce topographically-trapped baroclinic waves with periods of 3.8 and 2.6 days. Such baroclinic motions could lead to variability in the internal wave shear variance, and hence in κ_z, at those periods. We have not proved definitively that this was indeed occurring in Shag Rocks Passage: to do so would require a high resolution model with bathymetry which was an accurate representation of Shag Rocks Passage (including the seamount), plus accurate information about the mean flow so as to model the interaction of the mean flow with the seamount.

Chapter 5

An assessment of density-based fine-structure methods for estimating diapycnal diffusivity in the Southern Ocean

This chapter forms the basis of a paper currently in preparation for publication in the Journal of Atmospheric and Oceanic Technology.

citation: Frants, M., S. Gille, J. MacKinnon, G. M. Damerell, K. J. Heywood, 2012, An assessment of density-based fine-structure methods for estimating diapycnal diffusivity in the Southern Ocean, J. Atmos. Oceanic Technol., in preparation.

Marina Frants, Sarah Gille and Jennifer MacKinnon, from the Scripps Institution of Oceanography, worked on the problem of the noise characteristics of the data. I was involved with the diffusivity calculations, some general discussions on the noise, and re-working the text and figures after Marina Frants wrote the first draft.

5.1 Abstract

Fine-structure estimates of diapycnal diffusivity κ are computed from CTD and XCTD data sampled in Drake Passage and in the eastern Pacific sector of the Southern Ocean and are compared against microstructure measurements from the same times and locations. The microstructure data show vertical diffusivities that are an order of magnitude smaller over the smooth abyssal plain in the southeastern

Pacific than they are in Drake Passage, where diffusivities are thought to be enhanced by the flow of the Antarctic Circumpolar Current over rough topography. Fine-structure methods based on vertical strain estimates are successful at capturing the spatial variability between the low-mixing regime in the southeastern Pacific and the high-mixing regime of Drake Passage. Thorpe scale estimates for the same data set show no significant difference between Drake Passage and eastern Pacific estimates. XCTD profiles have lower vertical resolution and higher noise levels after filtering than CTD profiles, resulting in XCTD κ estimates that are, on average, an order of magnitude higher than CTD estimates. Overall, the estimates from both CTD and XCTD are 1 to 2 orders of magnitude higher than estimates made from microstructure measurements and tracer diffusion, suggesting that the approximations required for computing fine-structure estimates can lead to over-estimation of κ.

5.2 Introduction

Diapycnal turbulent mixing is a dominant factor in controlling the stratification and energy budget of the global ocean, as well as vertical fluxes of fresh water, nutrients and dissolved tracers (e.g. Munk and Wunsch, 1998). In the upper ocean, it drives the heat and gas exchanges between the ocean and the atmosphere, influencing the ocean's role in regulating global climate. Observations have revealed a high degree of spatial variability in diapycnal diffusivity κ, with typical background diffusivities of 10^{-5} m^2 s^{-1}, and regions of intense mixing where κ can be as high as 10^{-3} m^2 s^{-1} (Gregg, 1987; Toole et al., 1994). Spatial variations of diapycnal mixing have significant implications for ocean circulation and climate modeling (e.g. Simmons et al., 2004; Palmer et al., 2007; Nikurashin and Legg, 2011), and numerical models run with patchy mixing have substantially different upwelling patterns than models with uniform mixing (e.g. Jochum, 2009). Thus characterizing the spatial patterns of vertical diffusivities in the ocean has emerged as a priority research topic (MacKinnon et al., 2010).

Vertical diffusivities have typically been inferred from tracer release experiments, which measure the integrated effect of vertical diffusivity over many months (e.g. Ledwell et al., 2000, 2011) or from microstructure profiler measurements which are able to resolve the small vertical length scales thought to be responsible for diapycnal mixing in the ocean (e.g. Toole et al., 1994; Polzin et al., 1995; St. Laurent et al., 2012). However the availability of these measurements is limited due to cost, need for trained personnel, and difficulty of deploying the instruments in rough weather conditions. As a result, a number of alternative methods of estimating κ from fine-structure measurements have been developed. These include methods based on detecting static instabilities in otherwise stably stratified density profiles (Thorpe, 1977; Dillon, 1982) and on parameterizations of internal wave shear and strain variances (Kunze, 2003). These fine-structure approaches have been applied to a wide range of observations made with velocity profiles from lowered acoustic Doppler current profilers (LADCP) (e.g. Kunze et al., 2006; Naveira Garabato et al., 2004) or with density profiles from CTDs (e.g. Sloyan, 2005; Kunze et al., 2006; Gargett and Garner, 2008; Sloyan et al., 2010), eXpendable CTDs (XCTDs) (e.g. Thompson et al., 2007; Sloyan et al., 2010) and Argo floats (Wu et al., 2011). These estimates involve a number of approximations the accuracy of which has not been fully determined, particularly in extreme environments such as the low-stratification conditions that occur throughout the Southern Ocean. However, because fine-structure methods offer the promise of inexpensive global maps of

vertical diffusivity, there is a strong impetus to apply them to the existing archive of hydrographic data. Density profiles are of particular interest because there is a long historical archive of density data, and because the growing database of Argo profiles provides approximately 3000 new density profiles every 10 days (Roemmich et al., 2009). The objective of this study is to provide an assessment of fine-structure κ derived from density profiles in comparison with microstructure measurements collected as part of the Diapycnal and Isopycnal Mixing Experiment in the Southern Ocean (DIMES).

DIMES was conceived to measure both diapycnal mixing and isopycnal stirring over the comparatively smooth topography of the southeastern Pacific (upstream of Drake Passage) and through the rough topography of Drake Passage and the Scotia Sea where internal wave activity was expected to generate enhanced vertical mixing (Gille et al., 2007, 2012). The diapycnal mixing component of the project included purposeful tracer release as well as microstructure measurements. DIMES measurements in the southeastern Pacific showed κ to be 0.75 $\times$ 10^{-5} m^2 s^{-1} on the basis of microstructure measurements and 1.3 $\times$ 10^{-5} m^2 s^{-1} on the basis of tracer diffusion (Ledwell et al., 2011). In Drake Passage, St. Laurent et al. (2012) reported an order of magnitude more mixing, with mean values of κ found to be 1.3 $\times$ 10^{-4} m^2 s^{-1}. Similarly, in a separate field program in the Indian Ocean sector of the Southern Ocean, Waterman et al. (2012a) also found a strong contrast between regions of smooth sea floor and steep terrain, with κ averaging 6.9 $\times$ 10^{-5} m^2 s^{-1} over most of the region but reaching a maximum of 3.4 $\times$ 10^{-3} m^2 s^{-1} near the Kerguelen Plateau.

In parallel to the tracer release and microstructure profiling, the DIMES project also carried out an extensive fine-structure measurement campaign that included LADCP, XCTD, and CTD sampling intended to facilitate an assessment of fine-structure methods. Results from the LADCP data will be reported separately [A. Thurnherr, personal communication, 2012], and this study focuses specifically on density profile data. Previous fine-structure estimates in the Southern Ocean have indicated enhanced mixing over rough bathymetry (e.g. Sloyan, 2005) and have indicated diffusivities in Drake Passage, with κ ranging from O(10^{-4}) m^2 s^{-1} to O(10^{-3}) m^2 s^{-1} (Naveira Garabato et al., 2004; Thompson et al., 2007), somewhat higher than inferred from the DIMES microstructure or tracer measurements. While fine-structure estimates might be predicted to overestimate the magnitude of turbulent diapycnal mixing in the ocean due to the effects of instrument noise on density profiles and spectra, at a minimum we expect that a successful diapycnal diffusivity estimate should be able to show the order of magnitude diffusivity

contrast between abyssal plain in the southeastern Pacific and Drake Passage (Ledwell et al., 2011; St. Laurent et al., 2012).

In order to compute fine-structure diapycnal diffusivity from density profiles, we consider two commonly-used methods: the Thorpe scale method and the vertical strain method. Both methods depend only on density profiles and can therefore be applied when neither microstructure data nor LADCP measurements are available. Thus, the Thorpe scale and strain methods have the potential to provide mixing estimates over a wide spatial and temporal range, provided the data are of sufficient quality and vertical resolution. We compare the CTD and XCTD estimates against each other and against the estimates produced by microstructure measurements. The goal of this analysis is first to determine both for CTD and XCTD profiles whether either method can replicate the basic contrast between high and low κ reported in the microstructure data. Our second goal is to provide guidance about the accuracy and performance of fine-structure methods in the low-stratification environment of the Southern Ocean.

5.3 Data and Methods

5.3.1 Data

Fine-structure and microstructure data used for this study were collected during January and February 2010 DIMES cruise aboard *R/V Thomas G. Thompson*. The survey area covered a region between the Polar Front and the Southern Antarctic Circumpolar Current Front in the southeastern Pacific, as well as a transect across Drake Passage near 65°W. A total of 137 usable CTD profiles, using two sets of Seabird SBE 9*plus* sensors, and 22 usable XCTD profiles were obtained at locations shown in Figure 5.1. All three types of instruments were deployed concurrently where possible, specifically to facilitate comparing fine-structure mixing estimates against microstructure measurements. Four of the CTD casts were deployed to a target depth of 5000 m, and the rest were deployed to 2000 m or to 10 m above the bottom, whichever is the shallower. However, XCTDs sample to a maximum depth of 1100 m. For this analysis, we only use the data from the top 1000 m, both to facilitate comparisons with the XCTD and also because this depth range is sampled most extensively by the Argo program and by glider campaigns. Therefore evaluation of fine-structure performance in the top 1000 m is a prerequisite for determining what we can learn from routine density profiles.

Microstructure measurements were sampled with the High Resolution Profiler

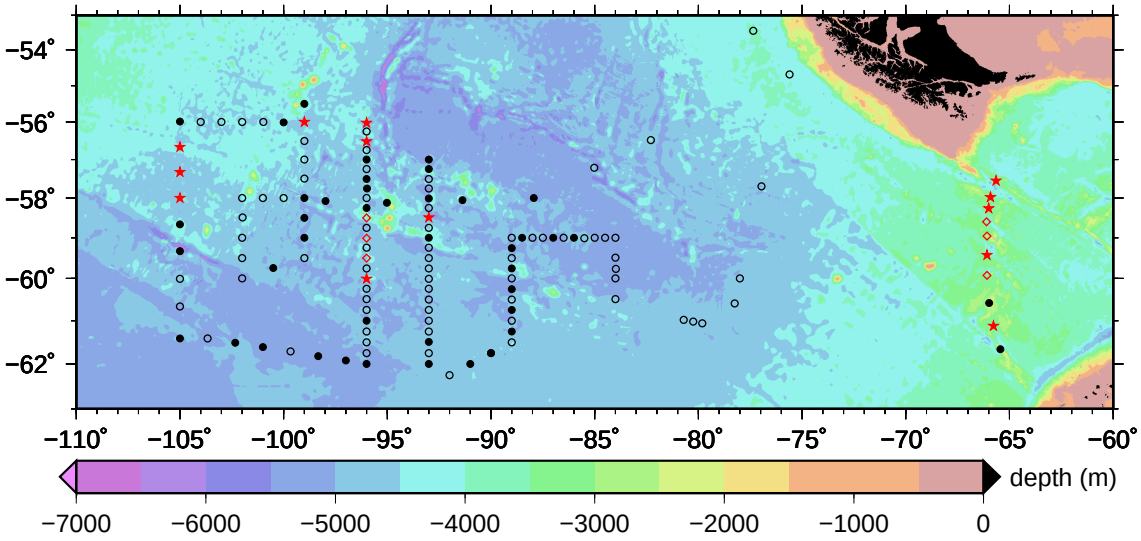

Figure 5.1: Locations of CTD stations, XCTD stations, and microstructure profiler stations sampled during the DIMES US2 cruise in austral summer 2010. Here red stars indicate stations for which concurrent microstructure, CTD, and XCTD casts are available, red open circles indicate concurrent CTD and XCTD casts, black filled dots indicate concurrent CTD and microstructure, and black open circles indicate only CTD data.

2 (HRP2) provided by Woods Hole Oceanographic Institution, and the Deep Microstructure Profiler (DMP), provided by Rockland Scientific International, Inc. A total of 40 usable profiles were obtained with HRP2, and 22 profiles with the DMP, as shown in Figure 5.1. Ledwell et al. (2011) provide detailed information about the instruments and the sampling methodology. The temperature (and thus density) profiles were averaged into 0.5 m bins for the HRP2 and into 1 m bins for the DMP.

5.3.2 Methods

5.3.2.1 Data pre-processing and noise estimation

Both of the fine-structure parameterization methods used in our analysis require a clear understanding of the noise characteristics of the data, as well as sufficient vertical resolution to resolve the turbulence. The raw data must be carefully processed in order to minimize the effects of instrument noise and measurement errors (Gargett and Garner, 2008; Gille et al., 2009; Uchida et al., 2011).

The temperature and conductivity sensors on the 9*plus* CTD sample at 24 Hz. At typical winch speeds, this results in a vertical spatial resolution of approximately 3 cm. However the resolution will vary with changes in winch speed. CTDs are also subject to ship roll, which can create pressure reversals in the measured profiles.

XCTDs record measurements at 25 Hz, equivalent to approximately 14 cm vertical resolution. They fall freely through the water column, and are not affected by ship motion. However, they are not intended to be high-precision instruments. Gille et al. (2009) found that almost all XCTDs exhibit anomalous spectral spikes at the 5 and 10 Hz sampling frequencies in both the temperature and the conductivity spectra. To remove the spectral energy at these frequencies, they developed a method for designing a low-pass filter to remove all energy at frequencies of 5 Hz or greater. Applying the same method to our data, we designed a 21-pt filter where the spectral energy tapers from 1 to 0 in the frequency range between 22% and 34% of the 12.5 Hz Nyquist frequency. This filter was used in addition to the low-pass Hamming filter with a 19-scan window as suggested by Uchida et al. (2011). The filtered and unfiltered spectra for the DIMES profiles sampled in Drake Passage are shown in Figure 5.2a,b.

Both CTDs and XCTDs are subject to salinity spiking caused by the differing time responses of the temperature and conductivity sensors (Johnson et al., 2007; Gargett and Garner, 2008). To minimize the effects of this spiking for both instruments, we utilized an iterative procedure similar to the approach used by Johnson et al. (2007) to estimate the lag between sensor pairs by minimizing the cross-spectral phase and maximizing the squared coherence between temperature and conductivity (R. Todd, personal communication). After correcting for the thermal lag, pressure reversals caused by ship roll were removed from the CTD profiles (Gargett and Garner, 2008), and salinity was computed from the filtered and lag-corrected data. Finally, all data were linearly interpolated to 0.25 m depth intervals. The resulting wavenumber spectra of salinity for the CTD and XCTD are shown in Figure 5.2c.

The raw XCTD profiles in our data set show uniform-sized discretized fluctuations of 0.01°C for temperature and 0.02 S/m for conductivity, implying corresponding measurement uncertainties of 0.005°C and 0.01 S/m. To evaluate the resulting uncertainties in the density values, we performed a 100-run Monte Carlo simulation in which the measured temperature and conductivity values were perturbed by normally distributed random noise with the same standard deviation as the measurement uncertainties. The resulting density uncertainty was approximately 0.012 kg m^{-3}.

To estimate the remaining noise in our processed CTD data, we followed the procedure described by Gargett and Garner (2008) and examined individual density profiles, defining the noise level for each profile to be the standard deviation of detrended density values within a 10 m layer where density is well-mixed. Based

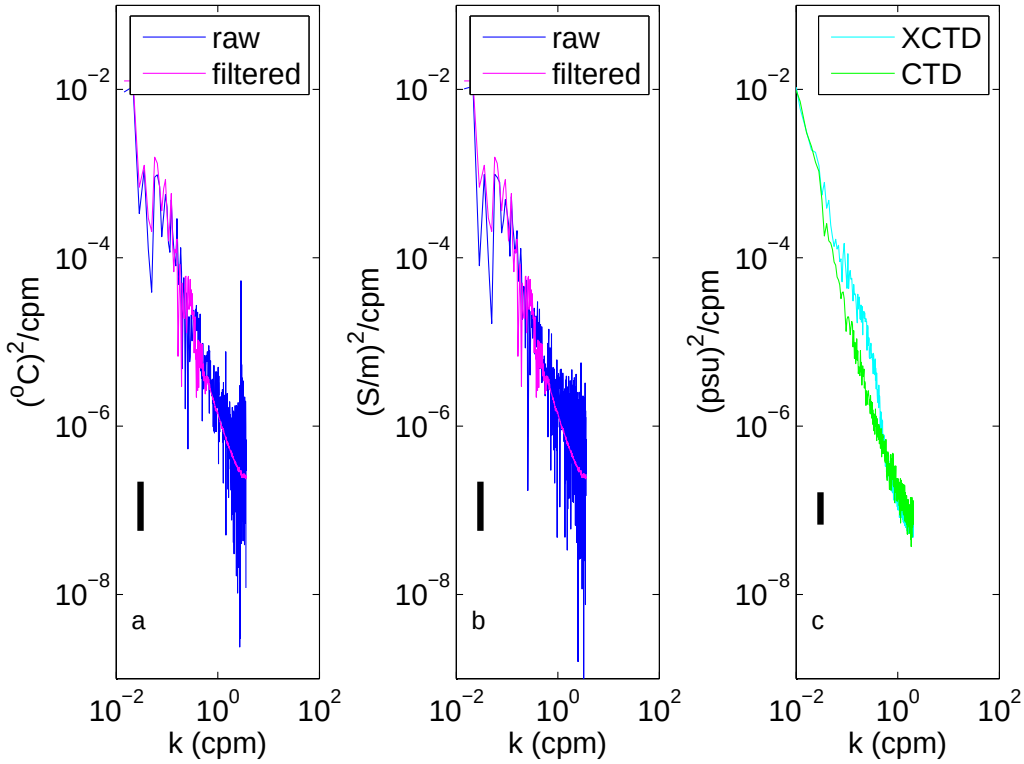

Figure 5.2: Comparison of raw and filtered spectra of (a) temperature and (b) conductivity for XCTD profiles sampled in Drake Passage during the 2010 DIMES survey; comparison of filtered, binned and time lag-corrected salinity spectra (c) for CTD and XCTD profiles sampled in Drake Passage during the 2010 DIMES survey. Error bars represent 95% confidence intervals, computed based on the χ^2 cumulative distribution of the spectra (Bendat and Piersol, 2000). For each comparison, spectra from all available Drake Passage casts were calculated from detrended 1000-pt profile segments centered on 600 m depth, then averaged together. (Vertical resolution differs for the processed data used in panel c, compared with the data used in panels a and b, and this accounts for a difference in the range of wavenumbers considered.)

on this criterion, the noise level in the CTD density profiles was approximately 4×10^{-4} kg m^{-3}.

5.3.2.2 Thorpe scale analysis and overturn validation

Thorpe scale analysis (Thorpe, 1977) provides a method for estimating small-scale mixing rates from temperature and salinity data in places where direct microstructure measurements are not available. The goal of the analysis is to determine kinetic energy dissipation rate ϵ and diapycnal eddy diffusivity κ_ρ. The

value of ϵ is related to the Ozmidov scale L_O (Ozmidov, 1965) by

$$\epsilon = L_O^2 N^3 \,, \tag{12}$$

where N is the buoyancy frequency.

The Thorpe scale L_T is obtained by reordering a vertical profile that contains density overturns in order to create a stably stratified profile. It is defined as

$$L_T \equiv \sqrt{\langle d'^2 \rangle} \,, \tag{13}$$

where Thorpe displacement d' is the displacement of every reordered point from its original position in the profile.

Comparisons between L_O and L_T suggest a linear relationship between the two scales (Dillon, 1982; Crawford, 1986). Dillon (1982) found the coefficient to be $L_O =$(0.8 $\pm$ 0.4)L_T. Substituting this relationship into (12) gives

$$\epsilon_i = 0.64 L_{Ti}^2 \langle N \rangle_i^3 \,, \tag{14}$$

where i refers to the ith overturn.

Diapycnal eddy diffusivity can be computed from ϵ as

$$\kappa_\rho = \Gamma \epsilon N^{-2} \,, \tag{15}$$

where Γ is the mixing efficiency. Here we follow common convention (e.g. Thompson et al., 2007) and assume $\Gamma = 0.2$.

At the beginning of this section, we estimated the instrument noise level in our filtered data to be approximately 0.012 kg m^{-3} for the XCTD density profiles and approximately 4×10^{-4} kg m^{-3} for the CTD profiles. At depths between 600 and 1000 m for typical low-stratification profiles in our study region, density changes of 0.012 kg m^{-3} occur over depth changes of 15-20 m, and changes of 4×10^{-4} kg m^{-3} occur over 0.5-1.5 m. To reduce the number of false overturns, we discarded all XCTD overturns of less than 20 m and all CTD overturns of less than 1.5 m, or having a density difference of less than twice the instrument noise. To evaluate the effect of our choice of minimum overturn size on the diffusivity estimates, we also performed our analysis of the CTD data using a minimum overturn of 20 m to match the XCTD analysis. The resulting κ estimates were within one standard error of the estimates computed with a 1.5 m minimum overturn size, indicating that the differences between CTD and XCTD estimates are caused primarily by variations

in instrument performance rather than in the standards for overturn validation.

Galbraith and Kelley (1996) proposed an additional water mass test designed to reduce the number of false overturns caused by the mismatch in sensor response times, particularly in regions where temperature and conductivity vary rapidly with depth. The test is based on performing least-square fits to temperature and salinity within each overturn and computing the RMS of the differences between the fitted lines and the data. The results are then normalized by the RMS difference between the sorted and the unsorted density values within the same overturn to produce the quantities ζ_t for temperature and ζ_s for salinity. The quantity $\zeta = \max(\zeta_s, \zeta_t)$ can then be used as a measure of the tightness of the T-S relationship within the overturn. Galbraith and Kelley (1996) proposed $\zeta < 0.5$ as the threshold for overturn validation. However, Martin and Rudnick (2007) and Thompson et al. (2007) have found that a less stringent criterion of $\zeta < 1$ is sufficient, and we accordingly adopt the criterion of $\zeta < 1$ for our own analysis.

As a final step in reducing noise-related false overturns in the CTD data, we follow the method of Gargett and Garner (2008) of creating an intermediate density profile in which a constant density is maintained until a density change greater than a specified threshold value occurs between two successive data points. Potential overturns in the intermediate CTD profiles were then evaluated based on Gargett and Garner's (2008) overturn ratio criteria, replacing the Galbraith and Kelley (1996) criteria used for XCTD data:

$$R_0 = min(L^+/L, L^-/L)\,, \tag{16}$$

where L is the length of an overturn, L^+ is the length of that portion of L where the Thorpe displacements are positive, and L^- is the length of the portion where the displacements are negative. Values of $R_0 < 0.2$ implied that the prospective overturn was caused by a single density spike that might have been due to instrument noise, and overturns with these values were rejected.

For both CTD and XCTD data, the results for each cast were averaged into 100 m depth bins, and error bars were calculated as one standard error based on one standard deviation of the values averaged in each bin.

5.3.2.3 Vertical strain analysis

A second method of estimating κ_ρ derives from examining the energy spectra of vertical strain in the internal wave field. In the stratified ocean, non-linear interactions among internal waves transfer energy from higher wavelengths to

increasingly unstable, smaller wavelengths, eventually leading to turbulence. Comparison of various wave-dissipation models (Wijesekera et al., 1993) has shown that κ_ρ estimates that are in good agreement with observational data can be obtained by comparing the spectrum of the internal-wave-field strain rates with a model GM spectrum proposed by Garrett and Munk (1975).

Strain variance level $\langle \xi_z^2 \rangle$ is computed by integrating the Fourier-transformed spectral representation ϕ_λ of the buoyancy frequency to determine the maximum wavenumber k_{max} such that

$$\langle \xi_z^2 \rangle = \int_{k_{min}}^{k_{max}} \phi_\lambda \mathrm{d}k = 0.2\,, \tag{17}$$

where the minimum wavenumber $k_{min} = 0.01$.

The strain variance level for the GM spectrum is computed for the same wavenumber range as

$$\langle \xi_z^2 \rangle_{GM} = \frac{\pi E_0 b j_*}{2} \int_{k_{min}}^{k_{max}} \frac{k^2}{(k+k_*)^2} \mathrm{d}k\,, \tag{18}$$

where E_0 is the dimensionless energy level, b is the scale thermocline depth, j_* is the reference mode number and $2\pi k_*$ is the reference wavenumber, defined as 0.0073(N / N_0). Following Gregg and Kunze (1991), we set these parameters to be $E_0 = 6.3\times\ 10^{-5}$, $b = 1300$ m, $j_* = 3$, and $N_0 = 0.00524\mathrm{s}^{-1}$.

Strain-derived vertical diffusivity κ_ρ^ϕ can be calculated from equations (17) and (18) as

$$\kappa_\rho^\phi = \kappa_0 \frac{\langle \xi_z^2 \rangle^2}{\langle \xi_z^2 \rangle_{GM}^2} H(R_\omega) J(f,N)\,, \tag{19}$$

with $\kappa_0 = 0.05\times\ 10^{-4}$ m^2 s^{-1}.

H and J are empirical functions that account for the effect of latitude on the internal wave field. The function H is given as

$$H(R_\omega) = \frac{3R_\omega(R_\omega+1)}{4(R_{\omega GM}^2)} \sqrt{\frac{2}{R_\omega - 1}}\,, \tag{20}$$

where $R_\omega = \langle V_z^2 \rangle / (N^2 \langle \xi_z^2 \rangle)$ is the shear/strain ratio, with V_z being the vertical derivative of horizontal velocity. For our calculations, we followed Kunze et al. (2006) and set $R_\omega = 7$ and $R_{\omega GM} = 3$. J is given as

$$J(f,N) = \frac{f cosh^{-1}(N/f)}{f_0 cosh^{-1}(N_0/f_{30})}\,, \tag{21}$$

where $f_0 = 7.29\times\ 10^{-5}\text{s}^{-1}$ is the Coriolis frequency at 30° latitude.

Thompson et al. (2007) used equations (19), (20), and (21) to calculate spectra based on both buoyancy frequency and potential density profiles across Drake Passage, and found that both quantities produced spectra of similar amplitudes, with differences of less than 15%. Both spectra also showed the same spatial pattern of κ_ρ values across the passage. For our analysis, we used buoyancy frequency spectra, computed using the method described by Kunze (2003) and followed by Thompson et al. (2007).

To compare the vertical strain diffusivities for CTD and XCTD data, we computed κ_ρ^ϕ estimates for the CTD and XCTD sections sampled over two eastern Pacific transects and one Drake Passage transect during the DIMES survey, using an averaged value of the Coriolis parameter, $f = 1.27 \times 10^{-4}\text{s}^{-1}$ (latitude 60.7°S), for each transect. For every buoyancy frequency profile in the transect, we divided the data into 100 m depth bins, discarding the top 200 m to eliminate the mixed layer and the effects of ship's draft near the surface. We normalized the data in each bin by the average buoyancy frequency for that bin, then subtracted a linear trend before computing the spectrum. We then averaged the spectra over all casts in each bin. The resulting spectra for the XCTD and CTD, as well as the GM spectrum, are shown in Figure 5.3 for the mid-depth bins for all the stations in the Drake Passage transect.

5.4 Results and discussion

The diffusivity estimates produced by both Thorpe scale and vertical strain methods depend on the noise inherent in the available density profiles. We compare values of κ obtained from two sets of DIMES stations in which CTDs and XCTDs were deployed concurrently. One set consisted of stations located in the eastern Pacific sector of the Southern Ocean, while the other was sampled along a transect in Drake Passage near 65°W, as indicated in Figure 5.1.

In optimal conditions, we would compare the microstructure shear κ estimates against separate fine-structure κ estimates derived from HRP2/DMP, CTD, and XCTD density profiles. However, the HRP2 suffered from salinity spiking issues, for which a correction has not yet been determined (St. Laurent, personal communication, 2012). We considered using temperature profiles below the subsurface temperature maximum in order to evaluate fine-structure diffusivity, following an approach tested by Thompson et al. (2007). However temperature and density spectra differ substantially (not shown) implying that even below the

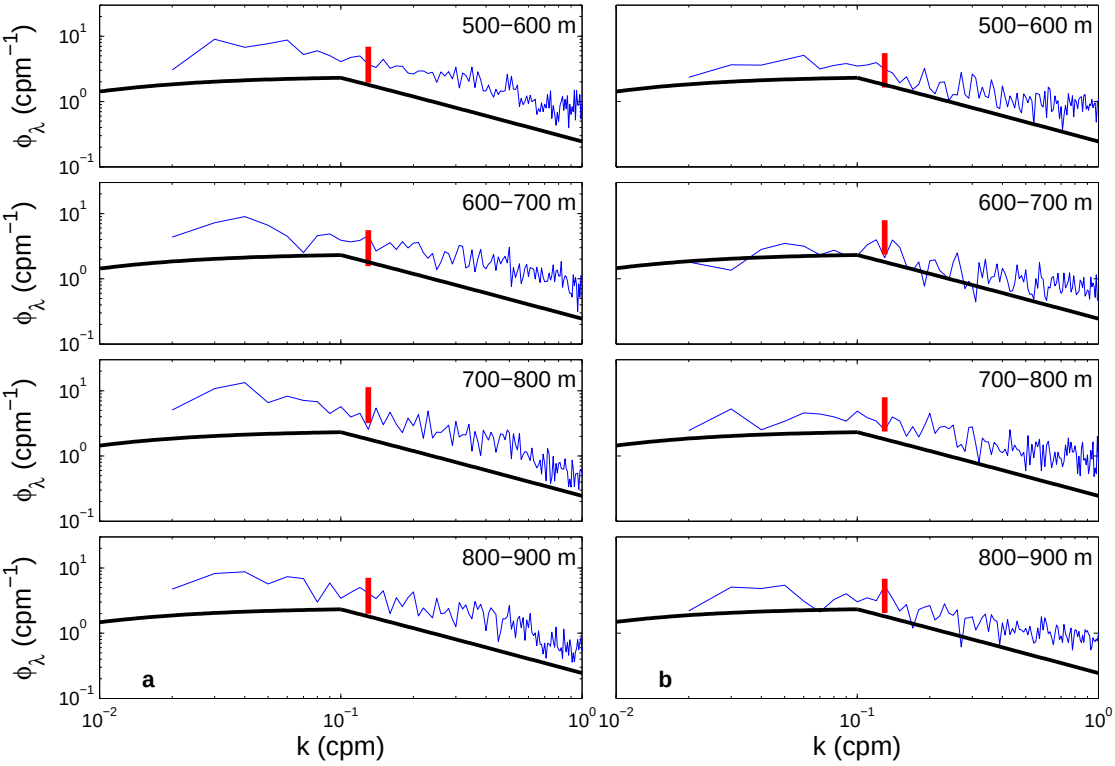

Figure 5.3: Comparison between vertical spectra of buoyancy frequency (blue) for the (a) XCTD and (b) CTD stations in Drake Passage, and the GM model spectrum (thick black line). Vertical red lines indicate the spectral uncertainty. The error bars on the spectra represent the 95% confidence interval, computed based on the χ^2 cumulative distribution of the spectra (Bendat and Piersol, 2000).

temperature maximum, salinity and temperature variations typically compensate each other, so that temperature alone is not representative of the density field. Thus the fine-structure results presented here are based on CTD and XCTD density profiles only, and these are compared with microstructure shear estimates of κ from the HRP2 and DMP centimeter-scale shear probes.

5.4.1 Thorpe scale method

Thorpe scale κ estimates are shown in Figure 5.4a-b, for XCTD (blue) and CTD (green). Microstructure estimates (magenta) are also included for comparison. For each depth bin, the mean diffusivity estimates plotted here are determined by averaging results from all stations where profiles were available from all three instruments (XCTD, CTD and Microstructure), marked with red stars on Figure 5.1. To leading order, diffusivities are log-normally distributed, and uncertainties plotted here are computed from the standard deviation of $\log(\kappa)$. Both the CTD and the XCTD estimates in Figure 5.4 show values of similar order of magnitude to

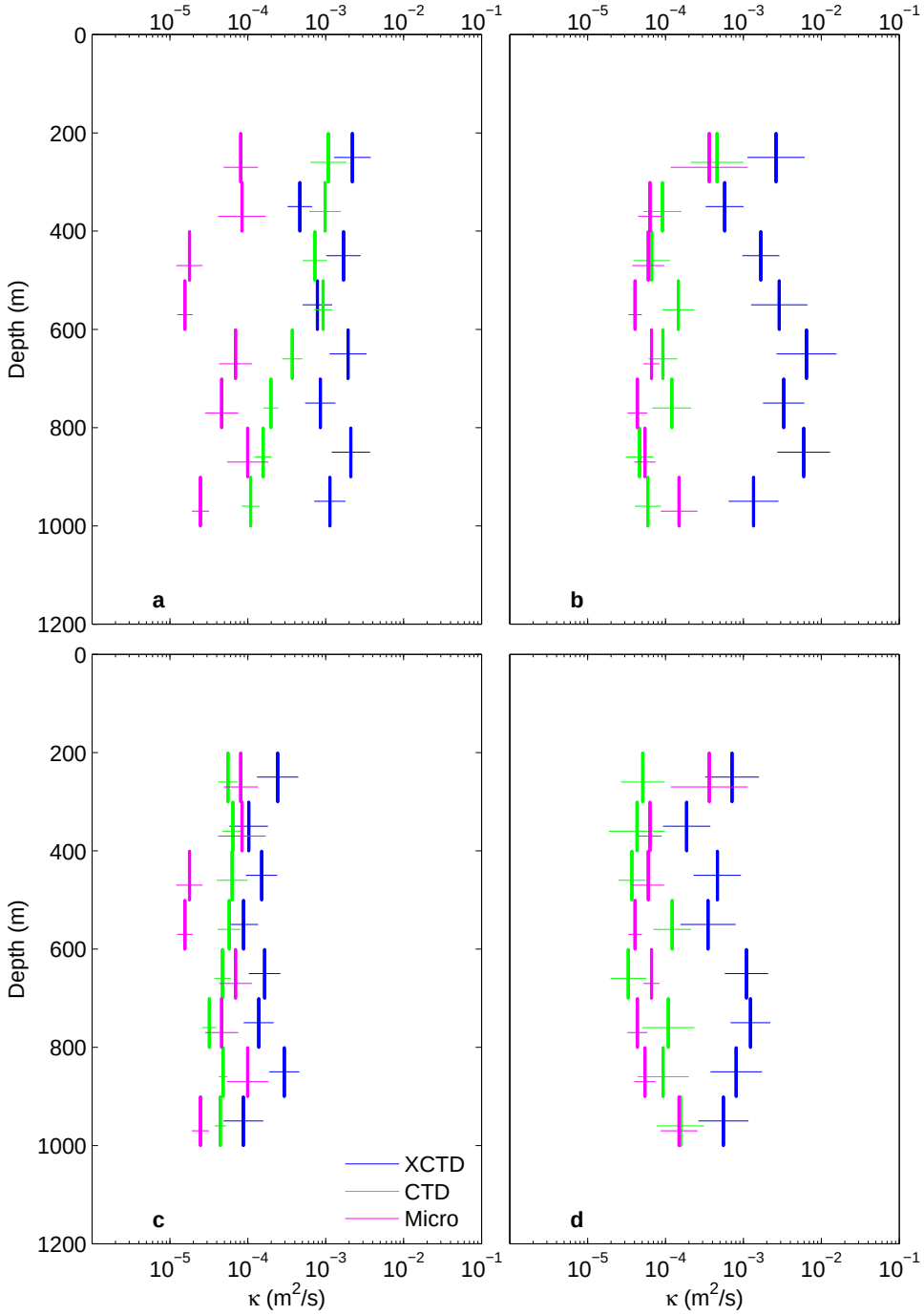

Figure 5.4: Thorpe scale (top row) and strain (bottom row) estimates of κ computed from CTD and XCTD data sampled during the DIMES survey in January and February 2010 in (a, c) southeast Pacific, (b,d) Drake Passage. Results shown here are based on stations for which all three instruments were available (red stars in Figure 5.1.) Estimates derived from measured microstructure shear are also plotted for comparison purposes.

previous fine-structure estimates (Naveira Garabato et al., 2004; Thompson et al., 2007). For example, the magnitude and vertical structure of the CTD estimates for the southeastern Pacific stations is consistent with the estimates made by Sloyan et al. (2010) in the southeastern Pacific during austral winter of 2005 and austral summer of 2006, with κ values being highest below the mixed layer and decaying with depth.

The XCTD Thorpe-scale κ estimates in Figure 5.4a-b are inconsistent with the microstructure shear estimates and previous observations from tracer diffusion (Ledwell et al., 2011) and LADCP (Naveira Garabato et al., 2004). The XCTD estimates are approximately two orders of magnitude larger than the microstructure shear estimates and do not reproduce the vertical structure seen in the microstructure estimates. The CTD Thorpe-scale κ estimates in the southeastern Pacific (Figure 5.4a), show similar inconsistencies with microstructure above 600 m, but below that depth they become more consistent with the microstructure estimates. In Drake Passage, the CTD Thorpe-scale κ estimates (Figure 5.4b) are reasonably consistent with the microstructure shear estimates, though they do not reproduce exactly the vertical structure of the microstructure estimates.

In order to capture the $O(10^{-5})$ m^2 s^{-1} diffusivities determined from microstructure data, with typical observed buoyancy frequencies N^2 of $O(10^{-5})$ in our survey region, equations (14) and (15) indicate that we should expect Thorpe scales of approximately 10 cm. Neither the CTD nor XCTD data are capable of resolving such small overturns, given the vertical resolution and noise thresholds estimated in section 5.3.2. Thus, in the southeastern Pacific and Drake Passage, overturns can only be observed from CTD or XCTD data at the upper tail of their probability distribution. If the spatial variability of large overturns were consistent with the spatial variability of all convective overturns, then Thorpe scales might be expected to yield useful information about the spatial patterns of κ. However, our results suggest that this is not the case in the ACC.

XCTD Thorpe-scales produce higher values of κ than the CTD estimates, with Drake Passage values up to two orders of magnitude larger. In addition the XCTD estimates have larger error bars. A comparison of CTD and XCTD salinity spectra (Figure 5.2c) shows different spectral slopes in the 10^{-1} to 10^{0} cpm frequency range, even after careful processing to minimize noise, as discussed in Section 5.3.2. The difference between the two spectra and the higher statistical uncertainties together suggest that the filtered XCTD data still retain significant instrument noise. Filtering at lower wavenumbers would reduce the noise, but at the cost of reducing the accuracy of the resulting estimates, because filtering would also increase the

minimum resolvable overturn size and filter out parts of the true turbulence signal along with noise.

5.4.2 Vertical strain method

Estimates of κ computed using the vertical strain analysis described in section 5.3.2.3 are shown in Figure 5.4c-d. Again, microstructure-based diffusivities (magenta) are indicated for comparison. Mean diffusivities for the strain analysis are determined in the same way as for Thorpe scales, by averaging all estimates within a depth bin, and error bars are again assigned assuming a log-normal distribution.

Compared with the Thorpe scale method, the strain method produces significantly smaller differences between the XCTD and CTD estimates, and between fine-structure instruments and microstructure. The XCTD estimates show a wider range of values and larger error bars than the CTD estimates, and XCTD estimates generally exceed CTD and microstructure estimates, particularly in Drake Passage below 600 m.

5.4.3 Diffusivity in Drake Passage versus the southeastern Pacific

At the most basic level, a successful fine-structure parameterization should capture the order of magnitude increase in vertical diffusivity between Drake Passage and the abyssal plain. In Figure 5.5, magenta lines indicate the ratio of microstructure κ in Drake Passage to microstructure κ over the abyssal plain. Uncertainties are determined by propagating the errors from the averaged κ's shown in Figure 5.4 . Half the bins show ratios greater than 1, which is generally consistent with tracer diffusivity differences inferred in the same region (Ledwell et al., 2011). The remaining bins show no significant variation between the two regions.

For Thorpe scales, panel a of Figure 5.5 compares the XCTD and CTD diffusivity ratios against the equivalent microstructure diffusivity ratios at stations where data from all instruments were available. For the XCTD Thorpe scale estimates (blue), half the bins show ratios greater than 1, though not at the same depths as the microstructure ratios. The CTD Thorpe scale estimates (green) indicate a ratio that is consistently less than one, reflecting the higher CTD estimates in the southeast Pacific as compared both with the corresponding microstructure estimates, and the CTD estimates in Drake Passage. The CTD ratios

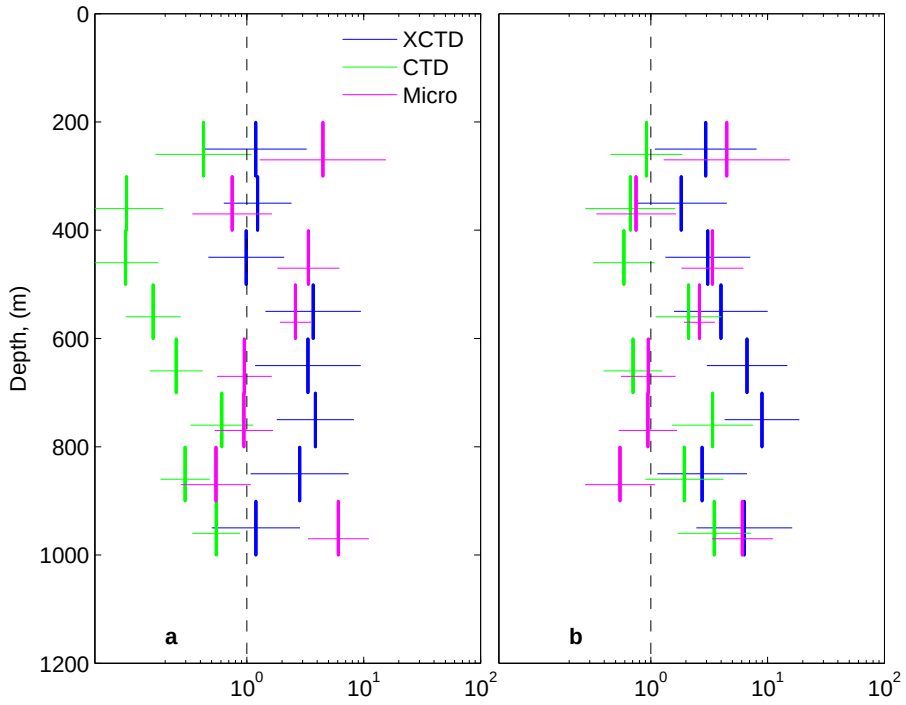

Figure 5.5: The ratios of (a) Thorpe and (b) strain estimates of κ in Drake Passage to the estimates in the southeast Pacific. Magenta lines indicate the ratio of microstructure shear estimates of κ in Drake Passage to the estimates in the southeast Pacific.

are inconsistent with the microstructure ratios and with previous observations by Ledwell et al. (2011); Naveira Garabato et al. (2004); St. Laurent et al. (2012) which indicate that diffusivities in Drake Passage are elevated compared to abyssal values. We suspect that this is because the CTD-Thorpe scale estimates over the abyssal plain are dominated by noise and thus very inaccurate, whereas the Drake Passage estimates are more accurate. However, without independent estimates (e.g., from microstructure) it is difficult to discover if one is taking measurements in a regime where the instrument used will give accurate results with the Thorpe scale method. Thus the Thorpe-scale method provides no formal means to distinguish high mixing and low mixing regimes.

Strain method ratios are shown in panel b of Figure 5.5. The XCTD ratios lie between 10^0 and 10^1, with values at some depths which are substantially larger than the microstructure shear ratios. The CTD ratios are consistently smaller than the XCTD ratios, with ratios in the 200-300 m and 400-500 m bins being smaller than the corresponding microstructure ratios by at least one standard error. Neither XCTD nor CTD reproduces the vertical structure of the microstructure shear ratios. When viewed over the entire water column, however, the strain method does appear

to be able to differentiate regions of high mixing from regions of low mixing with both XCTD and CTD data.

5.4.4 Quantifying diffusivity

A second test of a successful fine-structure parameterization is whether it provides reasonable quantitative estimates of the vertical diffusivity. Ledwell et al. (2011) found a factor of two difference between tracer-derived diffusivity and microstructure diffusivity, which might be attributable to temporal variability but could also indicate the presence of physical processes that generate mixing in ways that are not readily measured by microstructure probes. Similarly, Waterman et al.'s (2012b) ratios of microstructure and shear/strain fine-structure diffusivities computed near the Kerguelen Plateau indicate that the shear/strain estimates typically exceed microstructure by a factor of 2 to 3 in the top 1000 m of the ocean in regions of flow over rough topography. The Ledwell et al. (2011) and Waterman et al. (2012b) results suggest that density-based fine-structure diffusivities might be expected to provide order-of-magnitude agreement with microstructure diffusivities, but that we probably cannot expect them to agree by better than a factor of two or three.

Figure 5.6 shows ratios of fine-structure diffusivity to microstructure diffusivity for the two regions. For both the Thorpe scale (Figure 5.6a-b) and strain (Figure 5.6c-d) estimates, the XCTD diffusivity exceeds the microstructure diffusivity (blue). For the Thorpe scale approach, differences can be as much as two orders of magnitude, while the strain diffusivities provide a better match but can still exceed the microstructure by an order of magnitude or more at some depths. The Thorpe-scale over-estimates are consistent with indications that instrument noise in XCTD measurements leads to inflated estimates of diffusivity, with the Thorpe scale estimates being more affected than the strain estimates.

The CTD-derived fine-structure estimates provide a better quantitative match (green lines in Figure 5.6), but can still differ from microstructure κs by an order of magnitude, particularly for the Thorpe-scale method in the low diffusivity region of the southeastern Pacific (Figure 5.6a). The best fine-structure/microstructure agreement appears to occur for the Thorpe-scale based analysis of CTD data collected in Drake Passage, where microstructure measurements reflect the presence of enhanced mixing. However, the fact that Thorpe scales do not perform well in regions of lower mixing means that Thorpe scales are probably ill-suited for analyzing observations spanning regions of low stratification and low mixing. For

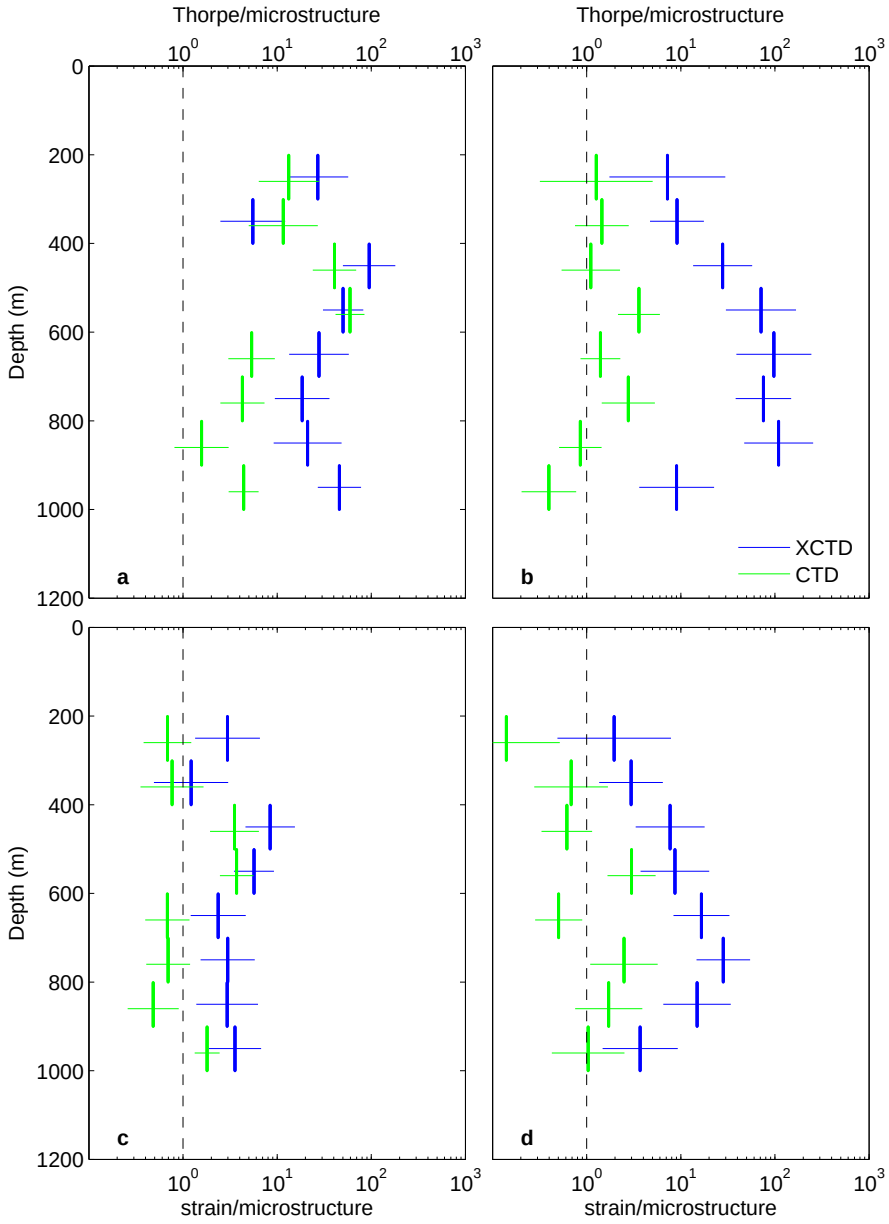

Figure 5.6: The ratios of Thorpe scale (top row) and strain (bottom row) estimates of κ to microstructure estimates for CTD and XCTD in (a, c) southeast Pacific and (b, d) Drake Passage.

the strain method, CTD-derived κ's usually agree with microstructure derived κ's within statistical uncertainty, though the statistical uncertainties can be large. The ratios of CTD strain estimates to microstructure estimates are within one order of magnitude for all depth bins except for the topmost bin in Drake Passage.

5.5 Summary

Fine-structure estimates of diapycnal diffusivities in the Southern Ocean were computed from CTD and XCTD data sampled during the DIMES survey in January and February of 2010. Both the Thorpe scale and the vertical strain method produced values of κ on the order of 10^{-4} to 10^{-3} m^2 s^{-1}. The fine-structure methods for the CTD and the XCTD tend to overestimate κ, compared with microstructure shear estimates, by at least an order of magnitude, except in Drake Passage, where the strain method for the CTD tends to underestimate κ compared with microstructure shear estimates.

A close examination of the noise characteristics of CTD and XCTD data indicates that once the data have been processed to minimize instrument noise, salinity spiking and ship effects, the minimum size of resolvable density overturns for Thorpe scales is approximately 1.5 m for CTD data and 20 m for the XCTD. Such a resolution is insufficient for the Thorpe scale method to resolve the small overturns that generate most of the mixing in the survey region. The XCTD-Thorpe scale κ estimates exceed the microstructure shear estimates by up to two orders of magnitude, while microstructure and CTD-Thorpe scale estimates match within an order of magnitude in Drake Passage.

The strain method produces more consistent κ estimates than does the Thorpe-scale method, and the CTD estimates match microstructure more closely than the XCTD. Neither the XCTD nor the CTD precisely reproduce the differences in diffusivity that have been previously measured between Drake Passage and the low-mixing region in the eastern Pacific section of the survey (Ledwell et al., 2011; St. Laurent et al., 2012), though the strain estimates provide a more consistent representation of the spatial variations, and the CTD yields more robust results with smaller statistical uncertainties than the XCTD. However, even with the CTD data, the strain method still leaves considerable uncertainty in κ, with values often overestimated in the southeastern Pacific and underestimated in Drake Passage.

Our analysis implies that CTD and XCTD measurements do not precisely replicate the microstructure estimates of small-scale mixing in the low-stratification regime characteristic of the Southern Ocean. However, both the Thorpe scale and the strain method have the potential to produce accurate estimates in regions where the stratification is high and mixing is characterized by large density overturns. Additional methods, such as a shear/strain approach based on a combination of CTD and LADCP data, may offer more possibilities for minimizing discrepancies between microstructure and fine-structure diffusivity estimates.

Chapter 6

Conclusions and Future Work

6.1 Context

The oceans are a significant part of the world climate system due to the high heat capacity of water, the contribution of the oceans to the meridional transport of heat, and the ocean-atmosphere exchanges of gases, water, heat, momentum and particulate matter (Bigg et al., 2003). In order to develop models which can accurately predict future responses to anthropogenic activity, we must first understand and quantify the ocean circulation and the driving mechanisms thereof.

In the Southern Ocean, the Antarctic Circumpolar Current (ACC) is the largest current system. The ACC is the only current to flow around the globe without encountering any continuous land barrier, facilitating the exchange of water and water mass properties (heat, salt, nutrients, etc.) between the Atlantic, Pacific and Indian Oceans. The transport of the ACC at different longitudes, and the baroclinic and barotropic variability in the transport, is an ongoing area of research (e.g. Cunningham et al., 2003; Ganachaud and Wunsch, 2000; Gladyshev et al., 2008; Heywood and King, 2002; Meijers et al., 2010; Rintoul and Sokolov, 2001). Observations of ACC transport on the northern flank of the Kerguelen Plateau were the subject of chapter 2.

The meridional overturning circulation is also an important component of the global climate system. While considerable progress has been made in measuring the rate of formation of deep water at high latitudes, the return of deep water to shallower depths remains an area of extensive research (Ganachaud and Wunsch, 2000). Some of this is accomplished by Ekman suction due to strong winds (Toggweiler and Samuels, 1995, 1998)), but much is due to turbulent mixing across isopycnals, referred to as diapycnal mixing. Model studies have shown that the

spatial variability of diapycnal diffusivity (κ_z) is a critical factor controlling the strength and structure of the circulation (see, for example, Huang, 1999; Marotzke, 1997; Marzeion and Drange, 2006; Saenko and Merryfield, 2005; Schmittner and Weaver, 2001; Zhang et al., 1999), and may even affect the response of the climate system to increased atmospheric CO_2 (Saenko, 2006). Efforts are therefore ongoing to measure κ_z as extensively as possible.

Unfortunately, measuring κ_z is complex and expensive. The most direct method, tracer release, requires a great deal of funding and ship time. Furthermore, tracer release suffers from the drawback of providing a measure of κ_z integrated over a wide area and time span: while this may improve the accuracy of measurement, very little information can be gained about the spatial and temporal variability of κ_z. The alternative is to use profiles of temperature, salinity and current velocities/shears as indicators of κ_z. Microstructure profilers are thought to provide reasonably accurate measurements but are very costly to build and operate, so efforts are underway to develop methods for calculating κ_z from data which can be obtained with greater ease and at less expense, such as data from CTDs/XCTDs and LADCPs (e.g. Naveira Garabato et al., 2004; Kunze et al., 2006; Mauritzen et al., 2002; Sloyan, 2005; Sloyan et al., 2010; Thompson et al., 2007). The use of CTD/XCTD density profiles to calculate κ_z was the subject of chapter 5.

Temporal variability in κ_z has not been widely addressed. Most existing measurements or estimates of κ_z are either snapshots at a single time, or a single integrated value over months or years. The few time series available, such as those discussed by Inall et al. (2000); Rippeth et al. (2002); Palmer et al. (2008); Moum and Nash (2009); Shroyer et al. (2010) are from shallow shelf seas or tidal channels, and cover only a few days or weeks, with the longest (Moum and Nash, 2009) spanning a period of four months. To discover if there is significant natural climate variability in κ_z, longer times series are required. Developing a method to calculate κ_z from the data collected by long-term, deep ocean moorings was the subject of chapter 3.

6.2 Progress

This thesis has presented results from three different Southern Ocean studies. Firstly, results were presented from the high resolution hydrographic survey carried out on the northern flank of the Kerguelen Plateau as part of the SOFine project. We identified a complex meandering current system with a blended STF/SAF to the north, a subsurface expression of the PF to the south, and a blended SAF/PF

to the east, which was deemed to be typical of the region. The total eastward volume transport was found to be 174 $\pm$ 22 Sv, mostly associated with the blended STF/SAF. This transport estimate is considerably larger than previous baroclinic estimates (Park et al., 1993; Sparrow et al., 1996) because of the large barotropic component of the total flow, and is also large compared with typical Drake Passage transports (Cunningham et al., 2003), but can be reconciled with other estimates of the total transport with the additional 15 Sv of the Indonesian Throughflow (Sprintall et al., 2009). The fronts may act as barriers to the exchange of water mass properties across surface waters, but may perhaps be acting as blenders deeper in the water column. Significant water mass transformation across isopycnals is not required to balance the budgets in this region, which is in agreement with the relatively moderate diapycnal diffusivities found by Waterman et al. (2012a). To our knowledge, we identify for the first time the presence of NIDW in the ACC on the northern flank of the Kerguelen Plateau.

These results could be of use in validating climate models by considering, for example, whether the variability in the models encompasses transport as high as 174 Sv in this region, and whether the models permit the presence of NIDW on the northern flank of the Kerguelen Plateau. Details of the flow around the Plateau is also of significance for biogeochemical studies, such as the effect of iron availability on phytoplankton blooms and the subsequent carbon export to the ocean interior (Blain et al., 2001, 2007).

The other results presented here were more directly concerned with measuring diapycnal diffusivity, and spanned areas of low mixing (the abyssal plain in the southeastern Pacific region of the Southern Ocean) and high mixing (Drake Passage and Shag Rocks Passage). Figure 6.1 outlines the mixing levels at these locations. These are in agreement with previous observations of enhanced mixing in regions where strong currents interact with complex topography (as discussed in chapter 1). Mixing over the Kerguelen Plateau is only moderately enhanced above background levels, but the topography here, although sloping, does not have as much small-scale topographic roughness as Drake Passage (Waterman et al., 2012a) or Shag Rocks Passage. Small-scale, in this context, refers to features O(100) m to O(10) km in size, from which linear theory predicts lee waves will radiate (Nikurashin and Ferrari, 2011). Satellite bathymetry can not resolve topographic features with scales shorter than 10-20 km; information about such features is only available from single beam or multibeam soundings.

As mentioned in section 6.1, efforts are ongoing in the oceanographic community to find ways to measure diapycnal diffusivity with greater ease and less

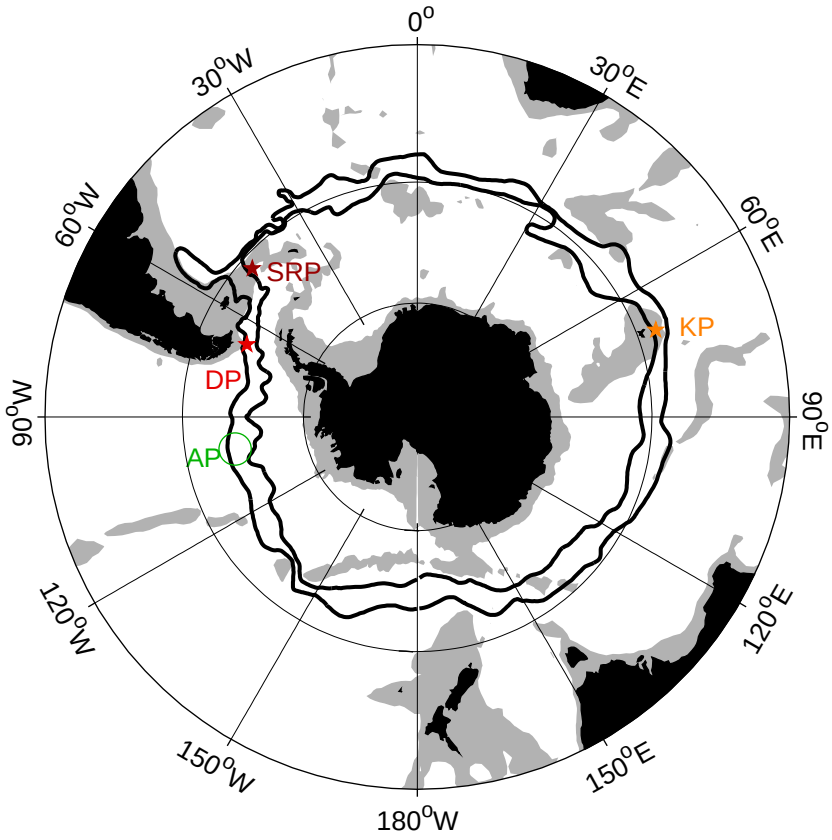

Figure 6.1: Schematic of the region south of 30°S, including the Southern Ocean, showing mixing levels at the locations discussed in this thesis. Depths shallower than 3000 m are shaded grey. Thick black contours indicate climatological mean locations of the Polar Front (south) and Subantarctic Front (north) from Orsi et al. (1995). Markers and labels indicate the locations discussed in previous chapters, with colours indicating the level of mixing: low mixing (green) at the abyssal plain (AP) in the southeastern Pacific region of the Southern Ocean (chapter 5), moderate mixing (orange) at the Kerguelen Plateau (KP, chapter 2), high mixing (red) in Drake Passage (DP, chapter 5), and higher still (dark red) in Shag Rocks Passage (SRP, chapter 3).

expense than tracer release or deploying microstructure profilers. Unfortunately, the results we present from the DIMES project (chapter 5) cast doubt on the advisability of using XCTD or CTD density profiles for this purpose, at least in areas of weak stratification (such as the Southern Ocean) and/or low mixing, and with the current calculation methods. The noise characteristics of the CTD and XCTD data result in a minimum size of resolvable density overturns (1.5 m for CTD data and 20 m for XCTDs for typical Southern Ocean low-stratification profiles) which is insufficient for the Thorpe scale method to resolve the small overturns that generate most of the mixing in the region surveyed. The method based on the variance of vertical strain was successful at capturing the order of

magnitude increase between the low-mixing regime in the southeastern Pacific and the high-mixing regime of Drake Passage, but the estimates still do not reproduce the vertical structure of estimates made using microstructure shear profiles, and can differ from microstructure shear estimates by more than an order of magnitude.

One of the interesting aspects of the Shag Rocks Passage Study (chapter 3) is the lack of a seasonal cycle or semi-annual signals such as are seen in Southern Ocean winds (Large and Van Loon, 1989). We might have expected a seasonal or semi-annual cycle for two reasons: near-inertial oscillations generated by wind forcing might propagate downwards; the Polar Front might move seasonally, and the stratification and shear variability might differ on either side of the front. Neither effect was detected in this study. There were no significant correlations with the winds over the entire Southern Ocean, suggesting that the variability in this region, at the depths ensonified, is generated by instabilities in the ocean and buoyancy forcing but is not directly wind-driven. We also did not detect any signal which could be obviously connected with the movement of the Polar Front over the mooring. This might be because the method used to extrapolate N in the depths ensonified was insufficiently sensitive, but the lack of a significant correlation between the integrated shear variance and the temperature time series suggests that the movement of the front did not have a substantial influence on the waters ensonified.

6.3 Future research

It would be interesting, in the future, to repeat this aspect of the DIMES project (the simultaneous deployment of XCTD, CTD and microstructure profilers) in areas with higher stratification and/or mixing. One possible location would be the Brazil Basin (site of a number of the early observational studies measuring diapycnal diffusivity - see chapter 1 and Polzin et al., 1997; Ledwell et al., 2000), which incorporates both a smooth abyssal plain and the rough topography of the mid-Atlantic ridge, and has generally higher stratification than in the Southern Ocean. One advantage to carrying out such a study in the Brazil Basin would be to determine if there has been any change since the previous studies, but conversely, choosing another location with a suitable range in topographic roughness could extend the global coverage of diffusivity estimates.

Density profiles from any nearby Iridium Argo floats could also be considered, as these provide high-resolution (2 m) profiles that are able to resolve fine-scale (tens to hundreds of meters) strain (Wu et al., 2011). Data from Seagliders could

also be incorporated. Beaird et al. (2012) discuss a method to infer the rate of dissipation of turbulent kinetic energy (ϵ, from which κ is easily calculated) using data from Seagliders. Their Seaglider Large-Eddy Method utilises finescale vertical velocity measurements inferred from the vertical flight model of the Seaglider, as well as density measurements. They show that this method performs well (by comparison with a microstructure survey) in the energetic turbulence of the Faroe Bank Channel. Comparisons between this method and purely density profile based methods would also be interesting. Seagliders and Iridium Argo floats both provide profiles at much less expense than microstructure profilers, and the data coverage provided by these types of instruments is increasing rapidly.

As mentioned in section 3.6, the mooring in Shag Rocks Passage used for this study was not designed to measure κ_z, and in particular lacked temperature and salinity instrumentation in the water depths ensonified by the ADCP. Figure 6.2 outlines a possible improved design for a mooring intended for κ_z measurements. The basic design is similar to the mooring in Shag Rocks Passage, with the addition of a string of instruments giving reasonably accurate temperature and salinity readings (such as Seabird Electronics MicroCATs, as indicated here), in the depths ensonified. The spacing of these instruments is such that they fall at the centre of 100 m bins upwards from the ADCP, so that, if the quality of the ADCP velocity measurements is sufficient, the diffusivity estimates can be made every 100 m rather than averaged over the entire depth ensonified. If the mooring were to be deployed in an area where particularly complex stratification is expected, additional MicroCATs might be necessary, and similarly, in regions with particularly simple stratification fewer MicroCATs might be sufficient. 100 m spacing seems a reasonable baseline. RCMs are included above and below the depths ensonified, to provide verification that the velocities recorded by the ADCP (and, in particular, unexpected features/variability) are not instrument artefacts. The near-bottom RCM and MicroCAT are included so the bottom boundary layer can be compared with waters above. Pressure loggers are included so that mooring motion can be analysed. The portion of the mooring marked as 'Repeat Section' could be repeated upwards in the water column to give a more complete vertical picture. Increased mixing in the upper part of the water column has been ascribed to the influence of the wind in other studies (e.g. Jing and Wu, 2010; Wu et al., 2011; Waterman et al., 2012a), but a long time series of diffusivity estimates showing correlation with local winds would provide additional verification.

If such moorings were to be deployed in Shag Rocks Passage, it would be interesting to place three of them such that they encircled the seamount. If we

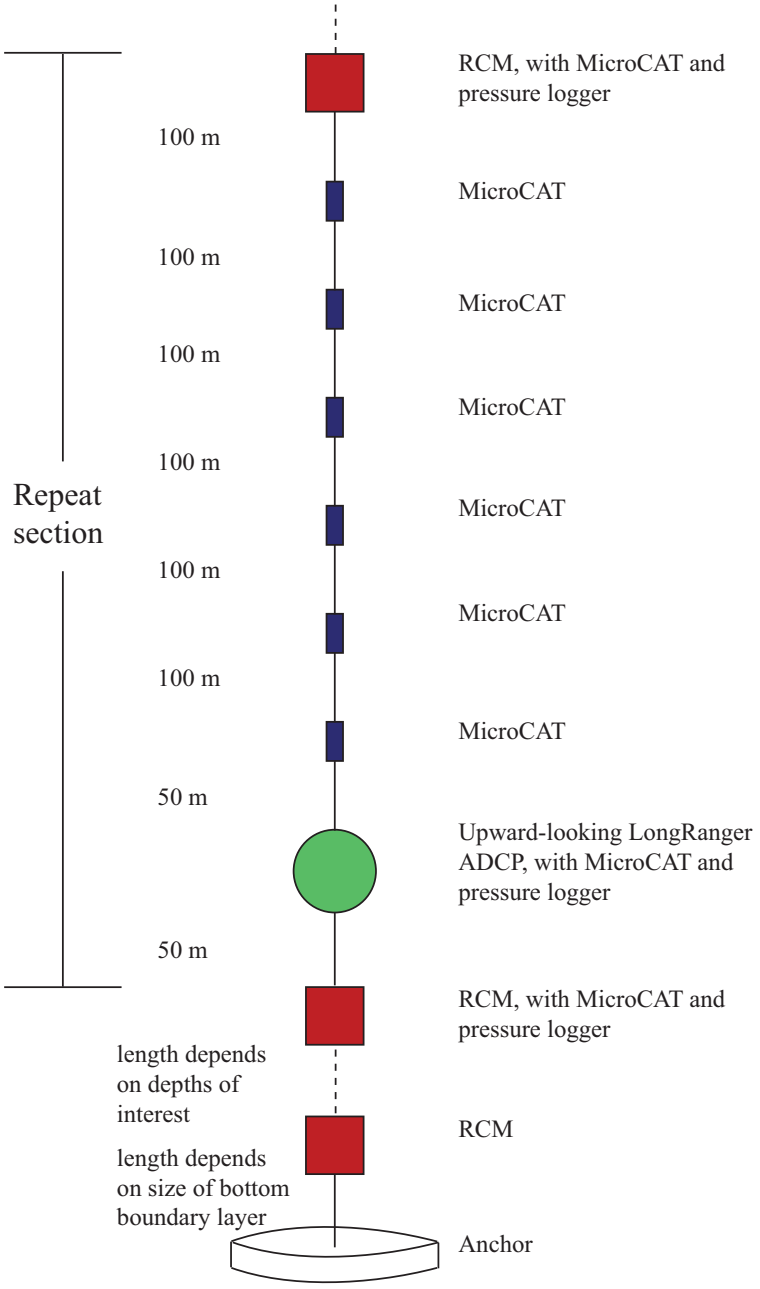

Figure 6.2: Schematic of a mooring designed for κ measurements. This is based on the moorings in Shag Rocks Passage, but includes MicroCATs in the water depths ensonified by the ADCP, so that a more accurate profile of buoyancy frequency is available.

are correct in our supposition of topographically trapped waves propagating around the seamount, variability due to these waves should be apparent in all the moorings. However, it would be of more general interest to place such moorings in locations covering a wide range in stratification and mixing regimes, current strengths and variability, eddy activity, and atmospheric conditions. With repeating chains of ADCPs, RCMs and MicroCATs, one could hypothetically achieve time series of diffusivity estimates showing the influence of stratification, currents, winds and eddies, and the time-and-depth variations in those effects, as well as increasing the dataset of diffusivity estimates around the global ocean. Time series of a year or more in length would give a first look at the natural climate variability in diapycnal diffusivity in the chosen locations.

Deploying moorings for the specific purpose of measuring diffusivity at a wide range of locations would amount to a very ambitious (and expensive!) program. More realistically, moorings could be modified on an opportunistic basis to allow for diffusivity estimates. If a mooring for another project already included a LongRanger ADCP, it would be relatively inexpensive to add RCMs above and below (if not already part of the mooring design), and a chain of MicroCATs in the water depths ensonified to provide the necessary temperature and salinity measurements.

It would also be sensible to test diffusivity estimates calculated from the data produced by such moorings against estimates from a microstructure profiler deployed in the same location. If possible, one would take concurrent CTD/LADCP and microstructure profiles in the vicinity of such a test mooring in a couple of different locations with smooth/rough topography, and at times with some different wind strengths. This should highlight regimes where the reduced vertical resolution (compared with normal CTD/LADCP profiles) is significantly degrading the diffusivity estimates. These tests could be combined with the hypothetical deployment, discussed above, of concurrent and co-located XCTDs, CTD/LADCP, microstructure profilers, Iridium Argo floats and Seagliders. Thus the microstructure profiles could be used efficiently to test a wide variety of finescale instruments and methods of calculating diapycnal diffusivity, which could also be inter-compared. These might provide an opportunity for some improvement in the finescale parameterization methods, which were originally developed by comparison with microstructure instruments (e.g. Gregg and Kunze, 1991; Polzin et al., 1995, 2002), but are still being modified and improved (e.g. Thurnherr, 2012).

6.4 Final Conclusions

Results from three Southern Ocean studies have been presented in this thesis. Firstly, the high resolution hydrographic survey carried out on the northern flank of the Kerguelen Plateau identified a complex meandering current system carrying a total eastward volume transport of 174 $\pm$ 22 Sv, mostly associated with the blended STF/SAF. Significant water mass transformation across isopycnals is not required to balance the budgets in this region, which is in agreement with the relatively moderate diapycnal diffusivities found by Waterman et al. (2012a). The results from the DIMES project cast doubt on the advisability of using CTD/XCTD density profiles to estimate diapycnal diffusivity in areas of weak stratification such as the Southern Ocean, because the noise characteristics of the data result in inaccurate diffusivity estimates. Finally, the work in Shag Rocks Passage has led to the development of a method for estimating diffusivity from moored ADCP velocity shear profiles. We derive an 18-month time series of diffusivity estimates with a median of 3.3×10^{-4} m^2 s^{-1} and a range of 0.5×10^{-4} m^2 s^{-1} to 57×10^{-4} m^2 s^{-1}. There is no significant signal at annual or semiannual periods, but there is evidence of signals at periods of approximately fourteen days (likely due to the spring-neaps tidal cycle), and at periods of 3.8 and 2.6 days most likely due to topographically-trapped waves propagating around the local seamount. We also outline a mooring design intended for the acquisition of diffusivity time series in the future, to allow for an assessment of natural climate variability in diapycnal diffusivity.

Bibliography

Alford, M. H., 2001: Internal swell generation: The spatial distribution of energy flux from the wind to mixed layer near-inertial motions. *J. Phys. Oceanogr.*, **31 (8)**, 2359–2368.

Alford, M. H., 2003a: Improved global maps and 54-year history of wind-work on ocean inertial motions. *Geophys. Res. Lett.*, **30 (8)**, 1424.

Alford, M. H., 2003b: Redistribution of energy available for ocean mixing by long-range propagation of internal waves. *Nature*, **423 (6936)**, 159–162.

Arhan, M., A. C. Naveira Garabato, K. J. Heywood, and D. P. Stevens, 2002: The Antarctic Circumpolar Current between the Falkland Islands and South Georgia. *J. Phys. Oceanogr.*, **32 (6)**, 1914–1931.

Baines, P. G., 1973: Generation of internal tides by flat-bump topography. *Deep-Sea Res.*, **20 (2)**, 179–205.

Baines, P. G., 1982: On internal tide generation models. *Deep-Sea Res.*, **29 (3)**, 307–338.

Beaird, N., I. Fer, P. Rhines, and C. Eriksen, 2012: Dissipation of turbulent kinetic energy inferred from seagliders: an application to the Eastern Nordic Seas Overflows. *J. Phys. Oceanogr.*, in press.

Bell, T. H., 1975: Topographically generated internal waves in open ocean. *J. Geophys. Res.*, **80 (3)**, 320–327.

Bendat, J. S. and A. G. Piersol, 2000: *Random data: analysis and measurement procedures*. 3d ed., John Wiley and Sons Ltd, 594 pp.

Bigg, G. R., T. D. Jickells, P. S. Liss, and T. J. Osborn, 2003: The role of the oceans in climate. *International Journal of Climatology*, **23 (10)**, 1127–1159.

Blain, S., et al., 2001: A biogeochemical study of the island mass effect in the context of the iron hypothesis: Kerguelen Islands, Southern Ocean. *Deep-Sea Res.*, **48 (1)**, 163–187, doi:10.1016/S0967-0637(00)00047-9.

Blain, S., et al., 2007: Effect of natural iron fertilization on carbon sequestration in the Southern Ocean. *Nature*, **446 (7139)**, 1070–U1, doi:10.1038/nature05700.

Bower, A. S., H. T. Rossby, and J. L. Lillibridge, 1985: The Gulf Stream - barrier or blender? *J. Phys. Oceanogr.*, **15 (1)**, 24–32.

Bray, N. A. and N. P. Fofonoff, 1981: Available potential-energy for mode eddies. *J. Phys. Oceanogr.*, **11 (1)**, 30–47.

Brink, K. H., 1989: The effect of stratification on seamount-trapped waves. *Deep-Sea Res.*, **36 (6)**, 825–844.

Broecker, W. S., 1997: Thermohaline circulation, the Achilles heel of our climate system: Will man-made CO2 upset the current balance? *Science*, **278 (5343)**, 1582–1588.

Bryden, H. L., 1979: Poleward heat-flux and conversion of available potential-energy in Drake Passage. *J. Mar. Res.*, **37 (1)**, 1–22.

Bryden, H. L. and R. A. Heath, 1985: Energetic eddies at the northern edge of the Antarctic Circumpolar Current in the Southwest Pacific. *Progress In Oceanography*, **14 (1-4)**, 65–87.

Charrassin, J. B., Y. H. Park, Y. Le Maho, and C. A. Bost, 2004: Fine resolution 3D temperature fields off Kerguelen from instrumented penguins. *Deep-Sea Res.*, **51 (12)**, 2091–2103.

Crawford, W. R., 1986: A comparison of length scales and decay times of turbulence in stably stratified flows. *J. Phys. Oceanogr.*, **16 (11)**, 1847–1854.

Cunningham, S. A., S. G. Alderson, B. A. King, and M. A. Brandon, 2003: Transport and variability of the Antarctic Circumpolar Current in Drake Passage. *J. Geophys. Res.*, **108 (C5)**, 8084.

D'Asaro, E. A., 1984: Wind forced internal waves in the North Pacific and Sargasso Sea. *J. Phys. Oceanogr.*, **14 (4)**, 781–794.

Deacon, G. E. R., 1937: The hydrology of the Southern Ocean. *Discovery Reports*, **15**, 1–124.

Dillon, T. M., 1982: Vertical overturns: a comparison of Thorpe and Ozmidov length scales. *J. Geophys. Res.*, **87**, 9601–9613, doi:10.1029/JC087iC12p09601.

ECMWF, cited 2009: European Centre for Medium-Range Weather Forecasts. ECMWF ERA-Interim re-analysis data. British Atmospheric Data Centre. Available online at http://badc.nerc.ac.uk/data/ecmwf-era-interim/.

Egbert, G. D., 1997: Tidal data inversion: interpolation and inference. *Progress In Oceanography*, **40 (1-4)**, 53–80.

Egbert, G. D. and S. Y. Erofeeva, 2002: Efficient inverse modeling of barotropic ocean tides. *J. Atmos. Oceanic Technol.*, **19 (2)**, 183–204.

Galbraith, P. S. and D. E. Kelley, 1996: Identifying overturns in CTD profiles. *J. Atmos. Oceanic Technol.*, **13 (3)**, 688–702.

Ganachaud, A. and C. Wunsch, 2000: Improved estimates of global ocean circulation, heat transport and mixing from hydrographic data. *Nature*, **408 (6811)**, 453–457.

Ganachaud, A., C. Wunsch, J. Marotzke, and J. Toole, 2000: Meridional overturning and large-scale circulation of the Indian Ocean. *J. Geophys. Res.*, **105 (C11)**, 26 117–26 134.

Gargett, A. and T. Garner, 2008: Determining Thorpe scales from ship-lowered CTD density profiles. *J. Atmos. Oceanic Technol.*, **25 (9)**, 1657–1670, doi:10.1175/2008JTECHO541.1.

Garrett, C., 2003: Mixing with latitude. *Nature*, **422 (6931)**, 477–478.

Garrett, C. and E. Kunze, 2007: Internal tide generation in the deep ocean. *Annu. Rev. Fluid Mech.*, **39**, 57–87.

Garrett, C. and W. Munk, 1975: Space-time scales of internal waves: a progress report. *J. Geophys. Res.*, **80 (3)**, 291–297.

Garrett, C. and L. St Laurent, 2002: Aspects of deep ocean mixing. *Journal of Oceanography*, **58 (1)**, 11–24.

Gille, S. T., 1997: The Southern Ocean momentum balance: evidence for topographic effects from numerical model output and altimeter data. *J. Phys. Oceanogr.*, **27 (10)**, 2219–2232.

Gille, S. T., A. Lombrozo, J. Sprintall, G. Stephenson, and R. Scarlet, 2009: Anomalous spiking in spectra of XCTD temperature profiles. *J. Atmos. Oceanic Technol.*, **26 (6)**, 1157–1164.

Gille, S. T., K. Speer, J. R. Ledwell, and A. C. Naveira Garabato, 2007: Mixing and stirring in the Southern Ocean. *EOS*, **88**, 382–383.

Gille, S. T., et al., 2012: The Diapycnal and Isopycnal Mixing Experiment: a first assessment. *CLIVAR Exchanges*, **17**, 46–48.

Gladyshev, S., M. Arhan, A. Sokov, and S. Speich, 2008: A hydrographic section from South Africa to the southern limit of the Antarctic Circumpolar Current at the Greenwich Meridian. *Deep-Sea Res.*, **55 (10)**, 1284–1303.

Gonella, J., 1972: Rotary-component method for analyzing meteorological and oceanographic vector time series. *Deep-Sea Res.*, **19 (12)**, 833–846.

Gordon, A. L., J. R. E. Lutjeharms, and M. L. Grundlingh, 1987: Stratification and circulation at the Agulhas Retroflection. *Deep-Sea Res.*, **34 (4)**, 565–599.

Gordon, A. L., E. Molinelli, and T. Baker, 1978: Large-scale relative dynamic topography of the Southern Ocean. *J. Geophys. Res.*, **83 (NC6)**, 3023–3032, doi: 10.1029/JC083iC06p03023.

Gordon, A. L., M. Visbeck, and B. Huber, 2001: Export of Weddell Sea Deep and Bottom Water. *J. Geophys. Res.*, **106 (C5)**, 9005–9017.

Gregg, M. C., 1987: Diapycnal mixing in the thermocline: a review. *J. Geophys. Res.*, **92 (C5)**, 5249–5286, doi:10.1029/JC092iC05p05249.

Gregg, M. C. and E. Kunze, 1991: Shear and strain in Santa Monica Basin. *J. Geophys. Res.*, **96 (C9)**, 16 709–16 719.

Gregg, M. C., T. B. Sanford, and D. P. Winkel, 2003: Reduced mixing from the breaking of internal waves in equatorial waters. *Nature*, **422 (6931)**, 513–515.

Gregg, M. C., H. E. Seim, and D. B. Percival, 1993: Statistics of shear and turbulent dissipation profiles in random internal wave-fields. *J. Phys. Oceanogr.*, **23 (8)**, 1777–1799.

Griesel, A., M. R. Mazloff, and S. T. Gille, 2012: Mean dynamic topography in the Southern Ocean: evaluating Antarctic Circumpolar Current transport. *Journal of Geophysical Research*, **117**, C01 020.

Hanawa, K. and L. D. Talley, 2001: Mode Waters, chap. 5.4. *Ocean Circulation and Climate: Observing and Modelling the Global Ocean*, G. Siedler, J. Church, and J. Gould, Eds., Academic Press, London, UK, International Geophysics Series, Vol. 77, 715 pp.

Hasumi, H. and N. Suginohara, 1999: Effects of locally enhanced vertical diffusivity over rough bathymetry on the world ocean circulation. *J. Geophys. Res.*, **104 (C10)**, 23 367–23 374.

Henyey, F. S., J. Wright, and S. M. Flatte, 1986: Energy and action flow through the internal wave field - an eikonal approach. *J. Geophys. Res.*, **91 (C7)**, 8487–8495.

Heywood, K. J., J. L. Collins, C. W. Hughes, and I. Vassie, 2007: On the detectability of internal tides in Drake Passage. *Deep-Sea Res.*, **54 (11)**, 1972–1984.

Heywood, K. J. and B. A. King, 2002: Water masses and baroclinic transports in the South Atlantic and Southern oceans. *J. Mar. Res.*, **60 (5)**, 639–676.

Heywood, K. J., A. C. Naveira Garabato, and D. P. Stevens, 2002: High mixing rates in the abyssal Southern Ocean. *Nature*, **415 (6875)**, 1011–1014.

Heywood, K. J., M. D. Sparrow, J. Brown, and R. R. Dickson, 1999: Frontal structure and Antarctic Bottom Water flow through the Princess Elizabeth Trough, Antarctica. *Deep-Sea Res.*, **46 (7)**, 1181–1200.

Holliday, N. P. and J. F. Read, 1998: Surface oceanic fronts between Africa and Antarctica. *Deep-Sea Res.*, **45 (2-3)**, 217–238.

Huang, R. X., 1999: Mixing and energetics of the oceanic thermohaline circulation. *J. Phys. Oceanogr.*, **29 (4)**, 727–746.

Inall, M. E., T. P. Rippeth, and T. J. Sherwin, 2000: Impact of nonlinear waves on the dissipation of internal tidal energy at a shelf break. *J. Geophys. Res.*, **105 (C4)**, 8687–8705.

IOC, SCOR, and IAPSO, 2010: *The international thermodynamic equation of seawater - 2010: Calculations and use of thermodynamic properties.* Intergovernmental Oceanographic Commission, Manuals and Guides No. 56, UNESCO (English).

Jackett, D. R. and T. J. McDougall, 1997: A neutral density variable for the world's oceans. *J. Phys. Oceanogr.*, **27 (2)**, 237–263.

Jacobs, S. S., 1991: On the nature and significance of the Antarctic Slope Front. *Mar. Chem.*, **35 (1-4)**, 9–24.

Jing, Z. and L. Wu, 2010: Seasonal variation of turbulent diapycnal mixing in the northwestern Pacific stirred by wind stress. *Geophys. Res. Lett.*, **37**, L23 604, doi: 10.1029/2010GL045418.

Jochum, M., 2009: Impact of latitudinal variations in vertical diffusivity on climate simulations. *J. Geophys. Res.*, **114**, C01 010, doi:10.1029/2008JC005030.

Johnson, G. C., J. M. Toole, and N. G. Larson, 2007: Sensor corrections for Sea-Bird SBE-41CP and SBE-41 CTDs. *J. Atmos. Oceanic Technol.*, **24 (6)**, 1117–1130, doi:10.1175/JTECH2016.1.

Kuhlbrodt, T., A. Griesel, M. Montoya, A. Levermann, M. Hofmann, and S. Rahmstorf, 2007: On the driving processes of the Atlantic meridional overturning circulation. *Rev. Geophys.*, **45 (1)**, RG2001.

Kunze, E., 1985: Near-inertial wave-propagation in geostrophic shear. *J. Phys. Oceanogr.*, **15 (5)**, 544–565.

Kunze, E., 2003: Yes, we have no abyssal mixing. *Near-Boundary Processes and Their Parameterizations: Proc. 'Aha Huliko'a Hawaiian Winter Workshop*, University of Hawaii at Manoa, 85–93.

Kunze, E., E. Firing, J. M. Hummon, T. K. Chereskin, and A. M. Thurnherr, 2006: Global abyssal mixing inferred from lowered ADCP shear and CTD strain profiles. *J. Phys. Oceanogr.*, **36 (8)**, 1553–1576.

Kunze, E. and T. B. Sanford, 1984: Observations of near-inertial waves in a front. *J. Phys. Oceanogr.*, **14 (3)**, 566–581.

Kunze, E., A. J. Williams, and M. G. Briscoe, 1990: Observations of shear and vertical stability from a neutrally buoyant float. *J. Geophys. Res.*, **95 (C10)**, 18 127–18 142.

Large, W. G. and H. Van Loon, 1989: Large-scale, low-frequency variability of the 1979 FGGE surface buoy drifts and winds over the southern hemisphere. *J. Phys. Oceanogr.*, **19 (2)**, 216–232.

Le Provost, C. and F. Lyard, 1997: Energetics of the M-2 barotropic ocean tides: an estimate of bottom friction dissipation from a hydrodynamic model. *Progress In Oceanography*, **40 (1-4)**, 37–52.

LeBlond, P. and L. Mysak, 1978: *Waves in the Ocean*. Elsevier.

Ledwell, J. R., E. T. Montgomery, K. L. Polzin, L. C. St Laurent, R. W. Schmitt, and J. M. Toole, 2000: Evidence for enhanced mixing over rough topography in the abyssal ocean. *Nature*, **403 (6766)**, 179–182.

Ledwell, J. R., L. C. St Laurent, J. B. Girton, and J. M. Toole, 2011: Diapycnal mixing in the Antarctic Circumpolar Current. *J. Phys. Oceanogr.*, **41 (1)**, 241–246.

Ledwell, J. R., A. J. Watson, and C. S. Law, 1998: Mixing of a tracer in the pycnocline. *J. Geophys. Res.*, **103 (C10)**, 21 499–21 529.

Lueck, R. G. and T. D. Mudge, 1997: Topographically induced mixing around a shallow seamount. *Science*, **276 (5320)**, 1831–1833.

MacKinnon, J. A., et al., 2010: Using global arrays to investigate internal-waves and mixing. *Proceedings of the "OceanObs'09: Sustained Ocean Observations and Information for Society" Conference*, J. Hall, D. E. Harrison, and D. Stammer, Eds., Venice, Italy, Vol. 2.

Marotzke, J., 1997: Boundary mixing and the dynamics of three-dimensional thermohaline circulations. *J. Phys. Oceanogr.*, **27 (8)**, 1713–1728.

Martin, J. P. and D. L. Rudnick, 2007: Inferences and observations of turbulent dissipation and mixing in the upper ocean at the Hawaiian Ridge. *J. Phys. Oceanogr.*, **37 (3)**, 476–494, doi:10.1175/JPO2992.1.

Marzeion, B. and H. Drange, 2006: Diapycnal mixing in a conceptual model of the Atlantic Meridional Overturning Circulation. *Deep-Sea Res.*, **53 (1-2)**, 226–238.

Mauritzen, C., K. L. Polzin, M. S. McCartney, R. C. Millard, and D. E. West-Mack, 2002: Evidence in hydrography and density fine structure for enhanced vertical mixing over the Mid-Atlantic Ridge in the western Atlantic. *J. Geophys. Res.*, **107 (C10)**, C103 147.

McComas, C. H. and P. Muller, 1981: The dynamic balance of internal waves. *J. Phys. Oceanogr.*, **11 (7)**, 970–986.

McDonagh, E. L., H. L. Bryden, B. A. King, and R. J. Sanders, 2008: The circulation of the Indian Ocean at 32 degrees S. *Progress In Oceanography*, **79 (1)**, 20–36.

McManus, J. F., R. Francois, J. M. Gherardi, L. D. Keigwin, and S. Brown-Leger, 2004: Collapse and rapid resumption of Atlantic meridional circulation linked to deglacial climate changes. *Nature*, **428 (6985)**, 834–837.

Meijers, A. J. S., A. Klocker, N. L. Bindoff, G. D. Williams, and S. J. Marsland, 2010: The circulation and water masses of the Antarctic shelf and continental slope between 30 and 80 degrees E. *Deep-Sea Res.*, **57 (9-10)**, 723–737.

Merryfield, B., 2005: Ocean mixing in 10 steps. *Science*, **308 (5722)**, 641–642.

Mohammad, R. and J. Nilsson, 2004: The role of diapycnal mixing for the equilibrium response of thermohaline circulation. *Ocean Dynamics*, **54 (1)**, 54–65.

Moore, J. K., M. R. Abbott, and J. G. Richman, 1997: Variability in the location of the Antarctic Polar Front (90 degrees-20 degrees W) from satellite sea surface temperature data. *J. Geophys. Res.*, **102 (C13)**, 27 825–27 833.

Moore, J. K., M. R. Abbott, and J. G. Richman, 1999: Location and dynamics of the Antarctic Polar Front from satellite sea surface temperature data. *J. Geophys. Res.*, **104 (C2)**, 3059–3073.

Moum, J. N. and J. D. Nash, 2009: Mixing measurements on an equatorial ocean mooring. *J. Atmos. Oceanic Technol.*, **26 (2)**, 317–336.

Munk, W. and C. Wunsch, 1998: Abyssal recipes II: energetics of tidal and wind mixing. *Deep-Sea Res.*, **45 (12)**, 1977–2010.

Munk, W. H. and E. Palmn, 1951: Note on the dynamics of the Antarctic Circumpolar Current. *Tellus*, **3**, 53–55.

Naveira Garabato, A. C., 2009: RRS James Cook Cruise 29, 01 Nov-22 Dec 2008. SOFine Cruise Report: Southern Ocean Finestructure. National Oceanography Centre Southampton Cruise Report No. 35, 216 pp.

Naveira Garabato, A. C., E. L. McDonagh, D. P. Stevens, K. J. Heywood, and R. J. Sanders, 2002: On the export of Antarctic Bottom Water from the Weddell Sea. *Deep-Sea Res.*, **49 (21)**, 4715–4742.

Naveira Garabato, A. C., K. L. Polzin, B. A. King, K. J. Heywood, and M. Visbeck, 2004: Widespread intense turbulent mixing in the Southern Ocean. *Science*, **303 (5655)**, 210–213.

Naveira Garabato, A. C., D. P. Stevens, and K. J. Heywood, 2003: Water mass conversion, fluxes, and mixing in the Scotia Sea diagnosed by an inverse model. *J. Phys. Oceanogr.*, **33 (12)**, 2565–2587.

Naveira Garabato, A. C., D. P. Stevens, A. J. Watson, and W. Roether, 2007: Short-circuiting of the overturning circulation in the Antarctic Circumpolar Current. *Nature*, **447 (7141)**, 194–197.

Nikurashin, M. and R. Ferrari, 2010a: Radiation and dissipation of internal waves generated by geostrophic motions impinging on small-scale topography: application to the Southern Ocean. *J. Phys. Oceanogr.*, **40 (9)**, 2025–2042.

Nikurashin, M. and R. Ferrari, 2010b: Radiation and dissipation of internal waves generated by geostrophic motions impinging on small-scale topography: Theory. *J. Phys. Oceanogr.*, **40 (5)**, 1055–1074.

Nikurashin, M. and R. Ferrari, 2011: Global energy conversion rate from geostrophic flows into internal lee waves in the deep ocean. *Geophys. Res. Lett.*, **38**, L08 610, doi:10.1029/2011GL046576.

Nikurashin, M. and S. Legg, 2011: A mechanism for local dissipation of internal tides generated at rough topography. *J. Phys. Oceanogr.*, **41 (2)**, 378–395, doi: 10.1175/2010JPO4522.1.

Nilsson, J., G. Brostrom, and G. Walin, 2003: The thermohaline circulation and vertical mixing: Does weaker density stratification give stronger overturning? *J. Phys. Oceanogr.*, **33 (12)**, 2781–2795.

Olbers, D., 1998: Comments on "On the obscurantist physics of 'form drag' in theorizing about the Circumpolar Current". *J. Phys. Oceanogr.*, **28 (8)**, 1647–1654.

Olbers, D., V. Gouretski, G. Seiss, and J. Schroter, 1992: *Hydrographic Atlas of the Southern Ocean*. Alfred Wegener Inst. for Polar and Mar. Res., Bremerhaven, Germany.

Orsi, A. H., G. C. Johnson, and J. L. Bullister, 1999: Circulation, mixing, and production of Antarctic Bottom Water. *Progress In Oceanography*, **43 (1)**, 55–109.

Orsi, A. H., T. Whitworth, and W. D. Nowlin, 1995: On the meridional extent and fronts of the Antarctic Circumpolar Current. *Deep-Sea Res.*, **42 (5)**, 641–673.

Osborn, T. R., 1980: Estimates of the local-rate of vertical diffusion from dissipation measurements. *J. Phys. Oceanogr.*, **10 (1)**, 83–89.

Ozmidov, R. V., 1965: On the turbulent exchange in a stably stratified ocean. *Izv. Acad. Sci. USSR, Atmos. Oceanic Phys.*, **1**, 861–871.

Palmer, M. D., A. C. Naveira Garabato, J. D. Stark, J. J. M. Hirschi, and J. Marotzke, 2007: The influence of diapycnal mixing on quasi-steady overturning states in the Indian Ocean. *J. Phys. Oceanogr.*, **37**, 2290–2304.

Palmer, M. R., T. P. Rippeth, and J. H. Simpson, 2008: An investigation of internal mixing in a seasonally stratified shelf sea. *J. Geophys. Res.*, **113 (C12)**, C12 005.

Park, Y. H., E. Charriaud, P. Craneguy, and A. Kartavtseff, 2001: Fronts, transport, and Weddell Gyre at 30 degrees E between Africa and Antarctica. *J. Geophys. Res.*, **106 (C2)**, 2857–2879.

Park, Y. H., L. Gamberoni, and E. Charriaud, 1993: Frontal structure, water masses, and circulation in the Crozet Basin. *J. Geophys. Res.*, **98 (C7)**, 12 361–12 385.

Park, Y. H., N. Gasco, and G. Duhamel, 2008a: Slope currents around the Kerguelen Islands from demersal longline fishing records. *Geophys. Res. Lett.*, **35 (9)**, L09 604.

Park, Y. H., F. Roquet, I. Durand, and J. L. Fuda, 2008b: Large-scale circulation over and around the Northern Kerguelen Plateau. *Deep-Sea Res.*, **55 (5-7)**, 566–581.

Park, Y. H., F. Vivier, F. Roquet, and E. Kestenare, 2009: Direct observations of the ACC transport across the Kerguelen Plateau. *Geophys. Res. Lett.*, **36**, L18 603.

Percival, D. and A. Walden, 1993: *Spectral Analysis for Physical Applications: Multitaper and Conventional Univariate Techniques*. Cambridge University Press.

Phillips, H. E. and S. R. Rintoul, 2000: Eddy variability and energetics from direct current measurements in the Antarctic Circumpolar Current south of Australia. *J. Phys. Oceanogr.*, **30 (12)**, 3050–3076.

Pollard, R. T., 1970: On generation by winds of inertial waves in ocean. *Deep-Sea Res.*, **17 (4)**, 795–&.

Pollard, R. T. and R. C. Millard, 1970: Comparison between observed and simulated wind-generated inertial oscillations. *Deep-Sea Res.*, **17 (4)**, 813–821.

Polzin, K., E. Kunze, J. Hummon, and E. Firing, 2002: The finescale response of lowered ADCP velocity profiles. *J. Atmos. Oceanic Technol.*, **19 (2)**, 205–224.

Polzin, K. L. and Y. V. Lvov, in press: Towards regional characterizations of the oceanic internal wavefield. *Rev. Geophys.*

Polzin, K. L., K. G. Speer, J. M. Toole, and R. W. Schmitt, 1996: Intense mixing of Antarctic Bottom Water in the equatorial Atlantic Ocean. *Nature*, **380 (6569)**, 54–57.

Polzin, K. L., J. M. Toole, J. R. Ledwell, and R. W. Schmitt, 1997: Spatial variability of turbulent mixing in the abyssal ocean. *Science*, **276 (5309)**, 93–96.

Polzin, K. L., J. M. Toole, and R. W. Schmitt, 1995: Finescale parameterizations of turbulent dissipation. *J. Phys. Oceanogr.*, **25 (3)**, 306–328.

Pond, S. and G. L. Pickard, 1983: *Introductory Dynamical Oceanography*. 2d ed., Pergamon Press, 329 pp.

Rahmstorf, S., 2002: Ocean circulation and climate during the past 120,000 years. *Nature*, **419 (6903)**, 207–214.

Rhines, P. B., 1969: Slow oscillations in an ocean of varying depth. Part 2. Islands and seamounts. *J. Fluid Mech.*, **37**, 191–205.

Rintoul, S. R. and S. Sokolov, 2001: Baroclinic transport variability of the Antarctic Circumpolar Current south of Australia (WOCE repeat section SR3). *J. Geophys. Res.*, **106 (C2)**, 2815–2832.

Rippeth, T. P., E. Williams, and J. H. Simpson, 2002: Reynolds stress and turbulent energy production in a tidal channel. *J. Phys. Oceanogr.*, **32 (4)**, 1242–1251.

Roemmich, D., et al., 2009: The Argo program: observing the global ocean with profiling floats. *Oceanography*, **22 (2)**, 34–43, doi:10.5670/oceanog.2009.36.

Roquet, F., Y. H. Park, C. Guinet, F. Bailleul, and J. B. Charrassin, 2009: Observations of the Fawn Trough Current over the Kerguelen Plateau from instrumented elephant seals. *J. Mar. Syst.*, **78 (3)**, 377–393.

Saenko, O. A., 2006: The effect of localized mixing on the ocean circulation and time-dependent climate change. *J. Phys. Oceanogr.*, **36 (1)**, 140–160.

Saenko, O. A. and W. J. Merryfield, 2005: On the effect of topographically enhanced mixing on the global ocean circulation. *J. Phys. Oceanogr.*, **35 (5)**, 826–834.

Sallee, J. B., K. Speer, R. Morrow, and R. Lumpkin, 2008: An estimate of Lagrangian eddy statistics and diffusion in the mixed layer of the Southern Ocean. *J. Mar. Res.*, **66**, 441–463.

Sanson, L. Z., 2010: Solutions of barotropic trapped waves around seamounts. *J. Fluid Mech.*, **661**, 32–44.

Schmittner, A. and A. J. Weaver, 2001: Dependence of multiple climate states on ocean mixing parameters. *Geophys. Res. Lett.*, **28 (6)**, 1027–1030.

Sciremammano, F., 1980: The nature of the poleward heat-flux due to low-frequency current fluctuations in Drake Passage. *J. Phys. Oceanogr.*, **10 (6)**, 843–852.

Sherman, J. T. and R. Pinkel, 1991: Estimates of the vertical wave-number frequency-spectra of vertical shear and strain. *J. Phys. Oceanogr.*, **21 (2)**, 292–303.

Shroyer, E. L., J. N. Moum, and J. D. Nash, 2010: Vertical heat flux and lateral mass transport in nonlinear internal waves. *Geophys. Res. Lett.*, **37**, L08 601.

Sievers, H. A. and W. D. Nowlin, 1984: The stratification and water masses at Drake Passage. *J. Geophys. Res.*, **89 (NC6)**, 489–514.

Simmons, H. L., S. R. Jayne, L. C. St Laurent, and A. J. Weaver, 2004: Tidally driven mixing in a numerical model of the ocean general circulation. *Ocean Modelling*, **6 (3-4)**, 245–263, doi:10.1016/S1463-5003(03)00011-8.

Sloyan, B. M., 2005: Spatial variability of mixing in the Southern Ocean. *Geophys. Res. Lett.*, **32 (18)**, L18 603.

Sloyan, B. M., L. D. Talley, T. K. Chereskin, R. Fine, and J. Holte, 2010: Antarctic Intermediate Water and Subantarctic Mode Water formation in the Southeast Pacific: the role of turbulent mixing. *J. Phys. Oceanogr.*, **40 (7)**, 1558–1574.

Smith, I. J., D. P. Stevens, K. J. Heywood, and M. P. Meredith, 2010: The flow of the Antarctic Circumpolar Current over the North Scotia Ridge. *Deep-Sea Res.*, **57**, 14–28.

Smith, W. H. F. and D. T. Sandwell, 1997: Global sea floor topography from satellite altimetry and ship depth soundings. *Science*, **277 (5334)**, 1956–1962.

Sokolov, S. and S. R. Rintoul, 2007: Multiple jets of the Antarctic Circumpolar Current south of Australia. *J. Phys. Oceanogr.*, **37 (5)**, 1394–1412.

Sokolov, S. and S. R. Rintoul, 2009: Circumpolar structure and distribution of the Antarctic Circumpolar Current fronts: 1. Mean circumpolar paths. *J. Geophys. Res.*, **114**, C11 018.

Sparrow, M. D., K. J. Heywood, J. Brown, and D. P. Stevens, 1996: Current structure of the south Indian Ocean. *J. Geophys. Res.*, **101 (C3)**, 6377–6391.

Speer, K., S. R. Rintoul, and B. Sloyan, 2000: The diabatic Deacon cell. *J. Phys. Oceanogr.*, **30 (12)**, 3212–3222.

Sprintall, J., S. E. Wijffels, R. Molcard, and I. Jaya, 2009: Direct estimates of the Indonesian Throughflow entering the Indian Ocean: 2004-2006. *J. Geophys. Res.*, **114**, C07 001.

St Laurent, L. and C. Garrett, 2002: The role of internal tides in mixing the deep ocean. *J. Phys. Oceanogr.*, **32 (10)**, 2882–2899.

St. Laurent, L. C., A. C. N. Garabato, J. R. Ledwell, A. M. Thurnherr, and J. M. Toole, 2012: Turbulence and diapycnal mixing in Drake Passage. *J. Phys. Oceanogr.*, submitted.

Stevens, D. P. and V. O. Ivchenko, 1997: The zonal momentum balance in an eddy-resolving general-circulation model of the Southern Ocean. *Quart. J. Roy. Meteor. Soc.*, **123 (540)**, 929–951, doi:10.1002/qj.49712354008.

Sverdrup, H. U., M. W. Johnson, and R. H. Fleming, 1942: *The Oceans: their Physics, Chemistry and General Biology*. Prentice-Hall, Englewood Cliffs, NJ, 1087 pp.

Talley, L. D., G. L. Pickard, W. J. Emery, and J. H. Smith, 2011: *Descriptive Physical Oceanography: an Introduction*. 6th ed., Elsevier Ltd, 555 pp.

Tamura, T., K. I. Ohshima, and S. Nihashi, 2008: Mapping of sea ice production for Antarctic coastal polynyas. *Geophys. Res. Lett.*, **35 (7)**, L07 606, doi:10.1029/2007GL032903.

Thompson, A. F., 2008: The atmospheric ocean: eddies and jets in the Antarctic Circumpolar Current. *Philos. Trans. Roy. Soc. London*, **366 (1885)**, 4529–4541, doi:10.1098/rsta.2008.0196.

Thompson, A. F., 2010: Jet formation and evolution in baroclinic turbulence with simple topography. *J. Phys. Oceanogr.*, **40 (2)**, 257–278, doi:10.1175/2009JPO4218.1.

Thompson, A. F., S. T. Gille, J. A. MacKinnon, and J. Sprintall, 2007: Spatial and temporal patterns of small-scale mixing in Drake Passage. *J. Phys. Oceanogr.*, **37 (3)**, 572–592.

Thompson, A. F., P. H. Haynes, C. Wilson, and K. J. Richards, 2010: Rapid Southern Ocean front transitions in an eddy-resolving ocean GCM. *Geophys. Res. Lett.*, **37**, L23 602, doi:10.1029/2010GL045386.

Thompson, A. F. and K. J. Heywood, 2008: Frontal structure and transport in the northwestern Weddell Sea. *Deep-Sea Res.*, **55 (10)**, 1229–1251.

Thompson, A. F. and K. J. Richards, 2011: Low frequency variability of Southern Ocean jets. *J. Geophys. Res.*, **116**, C09 022, doi:10.1029/2010JC006749.

Thomson, D. J., 1982: Spectrum estimation and harmonic-analysis. *J. Proc. IEEE*, **70 (9)**, 1055–1096.

Thorpe, S. A., 1977: Turbulence and mixing in a Scottish loch. *Philos. Trans. Roy. Soc. London*, **286 (1334)**, 125–181, doi:10.1098/rsta.1977.0112.

Thorpe, S. A., 1992: The generation of internal waves by flow over the rough topography of a continental slope. *Proc. Roy. Soc. London*, **439 (1905)**, 115–130.

Thorpe, S. A., 2005: *The Turbulent Ocean*. Cambridge University Press.

Thurnherr, A. M., 2012: The finescale response of lowered ADCP velocity measurements processed with different methods. *J. Atmos. Oceanic Technol.*, **29 (4)**, 597–600.

Toggweiler, J. R. and B. Samuels, 1995: Effect of Drake Passage on the global thermohaline circulation. *Deep-Sea Res. I*, **42 (4)**, 477–500.

Toggweiler, J. R. and B. Samuels, 1998: On the ocean's large-scale circulation near the limit of no vertical mixing. *J. Phys. Oceanogr.*, **28 (9)**, 1832–1852.

Toole, J. M., K. L. Polzin, and R. W. Schmitt, 1994: Estimates of diapycnal mixing in the abyssal ocean. *Science*, **264 (5162)**, 1120–1123.

Trani, M., P. Falco, and E. Zambianchi, 2011: Near-surface eddy dynamics in the Southern Ocean. *Polar Research*, **30**, 11 203.

Uchida, H., K. Shimada, and T. Kawano, 2011: A method for data processing to obtain high-quality XCTD data. *J. Atmos. Oceanic Technol.*, **28 (6)**, 816–826, doi:10.1175/2011JTECHO795.1.

van Aken, H. M., H. Ridderinkhof, and W. P. M. de Ruijter, 2004: North Atlantic Deep Water in the south-western Indian Ocean. *Deep-Sea Res.*, **51 (6)**, 755–776.

van Wijk, E. M., S. R. Rintoul, B. M. Ronai, and G. D. Williams, 2010: Regional circulation around Heard and McDonald Islands and through the Fawn Trough, central Kerguelen Plateau. *Deep-Sea Res.*, **57 (5)**, 653–669.

Walkden, G. J., K. J. Heywood, and D. P. Stevens, 2008: Eddy heat fluxes from direct current measurements of the Antarctic Polar Front in Shag Rocks Passage. *Geophys. Res. Lett.*, **35 (6)**, L06 602.

Wang, W. and R. X. Huang, 2004a: Wind energy input to the Ekman layer. *J. Phys. Oceanogr.*, **34 (5)**, 1267–1275.

Wang, W. and R. X. Huang, 2004b: Wind energy input to the surface waves. *J. Phys. Oceanogr.*, **34 (5)**, 1276–1280.

Warren, B. A., 1981: Transindian hydrographic section at lat 18-degrees-S - property distributions and circulation in the South Indian Ocean. *Deep-Sea Res.*, **28 (8)**, 759–788.

Waterman, S., A. C. Naveira Garabato, and K. L. Polzin, 2012a: Internal waves and turbulence in the Antarctic Circumpolar Current. *J. Phys. Oceanogr.*, in press.

Waterman, S., K. L. Polzin, A. C. Naveira-Garabato, and K. L. Sheen, 2012b: Suppression of internal wave breaking by lee wave-mean flow interactions in the Antarctic Circumpolar Current? *J. Phys. Oceanogr.*, submitted.

Webb, D. J. and N. Suginohara, 2001: Oceanography - vertical mixing in the ocean. *Nature*, **409 (6816)**, 37–37.

Wijesekera, H., L. Padman, T. Dillon, M. Levine, C. Paulson, and R. Pinkel, 1993: The application of internal-wave dissipation models to a region of strong mixing. *J. Phys. Oceanogr.*, **23 (2)**, 269–286.

Wu, L., Z. Jing, S. Riser, and M. Visbeck, 2011: Seasonal and spatial variations of Southern Ocean diapycnal mixing from Argo profiling floats. *Nature Geoscience*, **4 (6)**, 363–366.

Wunsch, C., 1998: The work done by the wind on the oceanic general circulation. *J. Phys. Oceanogr.*, **28 (11)**, 2332–2340.

Wunsch, C. and R. Ferrari, 2004: Vertical mixing, energy and the general circulation of the oceans. *Annu. Rev. Fluid Mech.*, **36**, 281–314.

You, Y. Z., 2000: Implications of the deep circulation and ventilation of the Indian Ocean on the renewal mechanism of North Atlantic Deep Water. *J. Geophys. Res.*, **105 (C10)**, 23 895–23 926.

Zhang, J. B., R. W. Schmidt, and R. X. Huang, 1999: The relative influence of diapycnal mixing and hydrologic forcing on the stability of the thermohaline circulation. *J. Phys. Oceanogr.*, **29 (6)**, 1096–1108.